Investigation Into The Effect Of Substrate On $Pb(Zr_{0.52}Ti_{0.48})O_3$ Films For MEMS Application

by

Dan Liu

A dissertation submitted to the Graduate Faculty of
Auburn University
in partial fulfillment of the
requirements for the Degree of
Doctor of Philosophy

Auburn, Alabama
May 09, 2011

Key words: Piezoelectric, MEMS, substrate effects, Nanoindentation

Copyright 2011 by Dan Liu

Approved by

Dong-Joo Kim, Chair, Associate Professor of Materials Engineering
ZhongYang Cheng, Associate Professor of Materials Engineering
Barton C. Prorok, Associate Professor of Materials Engineering
Robert L. Jackson, Associate Professor of Mechanical Engineering

Abstract

During the past several decades, PZT ($Pb(Zr,Ti)O_3$) thin films were given extensive attention for their potential as sensors and actuators in microelectromechanical systems (MEMS) due to their excellent piezoelectric properties. However, for thin films deposited on much thicker substrate, the piezoelectric response is influenced by the substrate clamping, which deviates PZT properties compared with bulk materials. Therefore, to optimize the performance of PZT thin film for a MEMS device, a comprehensive understanding of the clamping effect of substrate on PZT thin films is extremely pertinent.

This study investigated the effects of substrate on $Pb(Zr_{0.52}Ti_{0.48})O_3$films. To begin with the effects of structural layer on the mechanical and electrical properties of PZT film were investigated by varying film thickness and changing types of substrate. The PZT films were deposited by a sol-gel method on platinized silicon substrates, where silicon nitride and silicon oxide were used as a structural layer. The mechanical properties of PZT films were characterized by nanoindentation. Electrical properties as a function of film thickness and layer material were investigated. Residual stresses in PZT films were also characterized by Raman spectroscopy. The measured mechanical properties of PZT films on two types of substrate indicate that the structural layer has a significant influence on the obtained Young's moduli of PZT films. The PZT on SiNx-based substrates presented higher values than PZT on SiO_2-based substrate throughout the whole indentation depth. The substrate effect on film hardness, however, was

negligible since a hardness value of around 8.8GPa was measured for both PZT on SiNx- and SiO_2-based substrates. Significant influences of film thickness and substrate type on electrical properties were not observed for the investigated thickness range of the PZT films.

To study the true orientation effect on the mechanical properties of oriented PZT films, a new model of thin film indentation was developed and used to deconvolute the effects of film orientation and structural layer on the Young's modulus. The results indicated a clear substrate effect and the new model was able to extract the true film modulus from the measured flat region values. The moduli for (001) and (111)-oriented PZT film are about 159 GPa and 149 GPa, respectively.

The electrical and piezoelectric properties of fabricated PZT cantilevers with varying Si thickness were also measured and analyzed. As expected, a smaller thickness of Si substrate resulted in high polarization, dielectric and piezoelectric constants, probably due to the change of the residual stress condition. A model was developed to predict the residual stress in PZT cantilevers. It was found that varying Si thickness resulted in different residual stress conditions in the released PZT cantilever, thus leading to different electrical and piezoelectric properties of the devices.

Acknowledgements

I would like to express my respect and thanks to my advisor, Dr. Dong-Joo Kim. His direction, patience, and encouragement were invaluable throughout the entirety of my research and made this dissertation possible. From him, I learned to always believe in myself, work hard to overcome the obstacles, stand up to frustrations, and much more. He has generously provided me with everything I could have ever expected. It has truly been an honor to work in Dr. Kim's Lab and participate in the enjoyment of the scientific journey as a graduate student.

I am very grateful for the active support of Dr. Barton C. Prorok, Dr. ZhongYang Cheng, Dr. Arnold Vainrub and Dr.Robert Jackson for being on my dissertation committee. Professor Prorok literally restructured my knowledge of nanoindentation. His care for my development was evidenced through his valuable encouragement, questions and comments. Professor ZhongYang Cheng is a phenomenal teacher and scientist. His lectures and talks are remarkably enjoyable, to the point and easy to follow. I also want to thank him for always giving me suggestions and helping when my mother-in-law encountered a health issue.

I appreciate my colleagues and friends, Dr. Jung-hyun Park, Dr. DongnaShen, Dr. Sang H. Yoon, Dr. Howard C. Wikle, Dr. Bo Zhou, Dr. Xiaobing Shan, Hosang Ahn, Seon-Bae Kim, L.C. Mathison, Roy Howard, Charles Ellis, Steven Moore, Kewei Zhang, Peixuan Wu, Lin Zhang, Yating Chai, Wen Shen, Zijie Cai, and others, of whom there

are too many to mention, for their support and friendship. I would especially like to thank Dr. Jung-Hyun Park for teaching me MEMS fabrication.

Last but certainly not least, it is my family, who has always been there for me with unconditional love and support, that I dedicate this dissertation to. I am indebted to my wife, Yinghui Rong and my son, Andrew Liu, for their support, substantial patience and genuine love. Yinghui is a wonderful wife and my best friend, understanding and accommodating me throughout this journey. To my parents, I simply could not owe more. They brought me into the world and made me who I am. Also, many thanks to my elder sisters for loving and supporting me.

Table of Contents

Abstract ii

Acknowledgements iv

List of Figures ix

List of Tables xiii

Chapter 1 Introduction 1

1.1 Motivation 1

1.2 Two main aspects in the substrate effects of PZT films 2

1.2.1 Mechanical properties of PZT films 2

1.2.2 Electric properties of pMEMS structure with varying Si thickness 5

1.3 Research objective and dissertation structure 6

1.3.1 Research objective 6

1.3.2 Dissertation structure 7

Chapter 2 Literature Review 9

2.1 Piezoelectricity and piezoelectric materials 9

2.1.1 Piezoelectricity 9

2.1.2 Piezoelectric materials 12

2.2 Mechanical properties of thin film 15

2.2.1 Techniques for measuring mechanical properties of thin film 16

2.2.2 The development of analytical solutions for determining the mechanical properties of thin films 22

2.2.3 Mechanical properties of PZT films 28

2.3 PZT MEMS devices and fabrication background ... 35

Chapter 3 Investigation of the Effect of Substrates on the Measured Mechanical and Electrical Properties of PZT Films ... 41

3.1 Structure layer materials for MEMS devices - SiO_2 and SiNx ... 41

3.2 PZT film fabrication ... 42

3.3 Measurement of mechanical property of PZT films ... 45

3.3.1 Principle of measurement using nanoindentation ... 45

3.3.2 Experimental setup of nanoindentation ... 47

3.4 Measurements of electrical properties and residual stress of PZT films ... 48

3.5 Results and discussion ... 49

3.5.1 Mechanical properties of PZT films on different substrates ... 49

3.5.2 Electrical properties of PZT films on different substrates ... 59

3.6 Chapter summary ... 65

Chapter 4 Investigation of the Orientation Effect on the Mechanical Properties of PZT Films on Different Substrate ... 66

4.1 Introduction ... 66

4.2 Fabrication of oriented PZT films on different substrates ... 67

4.3 Results and discussion ... 69

4.4 Chapter summary ... 79

Chapter 5 Investigation of the Influence of Varying Si Substrate Thickness on the Electrical and Piezoelectric Properties of the PZT Cantilevers ... 80

5.1 Device design and fabrication ... 80

5.1.1 Device design ... 80

5.1.2 Device fabrication ... 86

5.2 Experimental setup and measurement of electric properties of PZT cantilevers on substrate with different Si thickness ... 92

5.3 Analytical model for predicting the distribution of residual stress in PZT cantilever 95

5.4 Results and discussion 102

5.4.1 Si substrate thickness measurement 102

5.4.2 Calculated residual stress by the developed model 104

5.4.3 Electrical properties and piezo-response of PZT cantilevers with different Si substrate thickness 109

5.5 Chapter summary 116

Chapter 6 Conclusion and Future Work 118

6.1 Conclusions 118

6.2 Future works 120

Bibliography 121

Appendix A 134

Appendix B 135

Appendix C 137

List of Figures

Figure 1-1 Laminated PZT/Si deflecting structures used in piezoelectric MEMS: bridge, cantilever and suspended membrane.[1] 3

Figure 1-2 A schematic illustration of MEMS components and their interconnection 5

Figure 2-1 Phase diagram for the $PbZrO_3$-$PbTiO_3$ system 13

Figure 2-2 Perovskite crystal structure of paraelectric PZT above its Curie temperature 14

Figure 2-3 Perovskite crystal structure of rhombohedral (F_R) and tetragonal (F_T) PZT .. 15

Figure 2-4 A sketch of nanoindentation system 19

Figure 2-5 Nanoindentation system for the measurement of mechanical properties of PZT films 20

Figure 2-6 (a) A typical load–displacement curve and (b) the deformation pattern of a sample during and after loading 21

Figure 2-7 A schematic diagram showing different strain fields in the film and substrate 27

Figure 2-8 (a) Young’s modulus and (b) the hardness as a function of penetration depth for PZT films annealed at 600,700 and 800^0C 30

Figure 2-9 Reduced modulus (Er) and hardness (H) versus indentation depth for 33

Figure 2-10 (a) Indentation modulus and (b) hardness of PZT films as a function of indentation depth 34

Figure 2-11 Typical process flow for the microfabrication of PZT/Si cantilever (cross section and top view) 38

Figure 2-12 The effect of residual stress on ferroelectric PZT cantilever MEMS structure 40

Figure 3-1 Schematic diagram for the preparation of PZT films 44

Figure 3-2 (a)Load-Displacement and (b) Young’s Modulus-Displacement curves of 1130nm PZT films 46

Figure 3-3 Nano indenter assembly parts 47

Figure 3-4 A TF analyzer 2000 for measuring piezoelectric properties of thin films 48

Figure 3-5 An impedance analyzer for measuring dielectric properties........................... 49

Figure 3-6 Young's Modulus as a function of the thickness of PZT films on SiO_2/Si and SiNx/Si substrates 50

Figure 3-7 XRD patterns of PZT films with different substrates and thickness............... 51

Figure 3-8 SEM images for PZT films on SiO_2/Si (left) and SiNx/Si (right) substrates with different thickness: (a)& (d)580nm; (b)& (e)830nm; and (c)& (f)1130nm (all have 60–280nm grain size) 52

Figure 3-9 Young's modulus as a function of displacement with 2200nm depth limit for PZT on SiO_2/Si and SiNx/Si substrates.. 54

Figure 3-10 Load-displacement curve of PZT film on SiNx-based substrate with 200nm depth limit indicating fracture point 55

Figure 3-11 SEM showing delamination and cracking around indentation 55

Figure 3-12 Hardness as a function of indentation depth with 2200nm depth limit for PZT on SiO_2/Si and SiNx/Si substrates 57

Figure 3-13 The dielectric constants of PZT films with different substrate as a function of DC bias (a) 580nm (6t) (b) 830nm (9t) (c) 1130nm (12t)...................................... 60

Figure 3-14 The electrical properties as a function of the thickness of PZT films on SiO_2/Si and SiNx/Si substrates 61

Figure 3-15 Raman spectra of PZT films on (a) SiO_2/Si and (b) SiNx/Si substrate......... 64

Figure 4-1 Flow chart for preparation of 0.5M PZT precursor with AcAc 67

Figure 4-2 Flow chart for preparation of 0.5M PZT precursor without AcAc 68

Figure 4-3 (a) XRD patterns of PZT films with SiO_2-based substrates. (b) XRD patterns of PZT films with SiNx-based substrates.. 70

Figure 4-4 Plots of experimental and calculated data for (a) SiO_2/Si (b) SiNx/Si 71

Figure 4-5 (a) Experimental and (b) calculated data of PZT films with (001) orientation on SiO_2/Si and SiNx/Si substrates 75

Figure 4-6 (a) Experimental and (b) calculated data of PZT films with (111) orientation on SiO_2/Si and SiNx/Si substrates 76

Figure 4-7 (a) Experimental and (b) calculated data of PZT films with mixed orientation on SiO_2/Si and SiNx/Si substrates 77

Figure 5-1 Schematic of the designed cantilevers 81

Figure 5-2 Schematic of the designed cantilevers on the wafer with 82

Figure 5-3 Schematic of the multi-layer configuration for the PZT cantilever 83

Figure 5-4 Mask for top electrode patterning 84

Figure 5-5 Mask for 1st cantilever patterning 84

Figure 5-6 Mask for 2st cantilever patterning 85

Figure 5-7 Mask for back-side etching 85

Figure 5-8 Schematic of the front-side etching for the PZT cantilevers 91

Figure 5-9 Setup for measurement of piezoelectric coefficients of the cantilevers 93

Figure 5-10 Schematic of displacement sensing mechanism of FS 94

Figure 5-11 Typical calibration curve of FS 95

Figure 5-12 Schematic of the stress condition (a) an arbitrary profile of the distributed stress in the constrained PZT thin film (b) the "bending stress" distribution in the released PZT cantilever 97

Figure 5-13 The errors involved in using Stoney's equation to calculate the residual stress in PZT film structure with varying Si thickness 101

Figure 5-14 Picture of fabricated cantilever array (a) front view (b) back view 103

Figure 5-15 The cross-sectional SEM image of a PZT thin film structure 104

Figure 5-16 The plots of (a) the residual stress and (b) bending curvature as a function of Si substrate thickness 105

Figure 5-17 The schematic of the deformed cantilever 107

Figure 5-18 SEM images of (a) the cross-section of Si substrate (b) free end of the curved cantilever (6mm) 108

Figure 5-19 SEM images of (a) the cross-section of Si substrate (b) free end of the curved cantilever (8mm) 109

Figure 5-20 Ferroelectric hysteresis loops measured at maximum applied voltage of 25v for all cantilevers 110

Figure 5-21 The remanent polarization as a function of the applied voltage for all cantilevers ... 111

Figure 5-22 The remanent polarization as a function of the Si thickness ... 111

Figure 5-23 Field dependence of the dielectric constant of all cantilevers ... 113

Figure 5-24 The dielectric constant as a function of the Si thickness ... 113

Figure 5-25 Tip displacement of the cantilevers as a function of the applied voltage ... 115

Figure 5-26 The piezoelectric coefficient d_{31} as a function of Si thickness ... 115

List of Tables

Table 2.1 Properties of some piezoelectric materials 12

Table 2.2 Current research status about the measurement of mechanical properties of PZT films 31

Table 2.3 Summary of typical materials used in pMEMS devices fabrication [1] 37

Table 3.1 Material properties of SiO_2 and SiN_x 42

Table 3.2 Description of PZT film structure 58

Table 3.3 The electric properties of PZT films with different thickness on two types of substrate 59

Table 3.4 The extracted residual stresses in the PZT films based on $A_1(TO_3)$ mode after background substraction and lorentz fitting 64

Table 4.1 Summary of the fabrication parameters and measured Young's Modulus 69

Table 5.1 Comparison of process conditions of two photoresists for cantilever patterning 88

Table 5.2 Comparison of calculated curvatures from the experimental results and developed model for two cantilevers 106

Table 5.3 Summary of measured properties of PZT cantilevers 116

Chapter 1 Introduction

1.1 Motivation

In recent years, there has been a growing interest in the field of microelectro-mechanical systems (MEMS) due to a strong requirement of miniaturization for higher performance devices with improved thermal management, reduced energy and materials consumption as well as cost advantages [1-3]. Since silicon has good mechanical properties, a relatively large band gap (1.12eV), and good processability, it is the most widely used semiconducting material in the MEMS field. Therefore, early MEMS devices were based on silicon to construct a wide range of devices; however, the need for flexibility in device design and performance improvement has motivated the development of new concepts, techniques, and new materials.

One of the avenues is to integrate functional materials into MEMS devices, which allows them to cover an entire range of physical phenomena. Among those functional materials, piezoelectric materials are of primary interest because they can directly provide an electro-mechanical conversion and are useful for many kinds of motion sensors, actuators, ultrasound and acoustic devices due to large motions with low hysteresis and high energy densities [4, 5]. An important family of piezoelectric materials are ferroelectric materials such as $Pb(Zr_{1-x}Ti_x)O_3$(PZT), $PbMg_{1/3}Nb_{2/3}O_3$-$PbTiO_3$ (PMN-PT), $BiScO_3$-$PbTiO_3$ and so on due to their large piezoelectric coefficients and

electromechanical coupling coefficients [6]. Such properties are of considerable importance in reducing the drive voltage or increasing the speed/sensitivity of a device. In comparison with commonly used piezoelectric materials such as ZnO and quartz, ferroelectric materials, PZT is known to have more than one order of magnitude larger piezoelectric coefficients. Furthermore, its properties can be easily tailored by controlling the composition between Zr and Ti [5, 7]. Therefore, PZT films are widely investigated in piezoelectric-based microelectromechanical systems [6, 8].

PZT films in a MEMS device are mechanically clamped by a massive substrate as shown in Figure 1-1, which deviates piezoelectric response of the films compared to bulk materials. The influence of film thickness, composition, and orientation on the piezoelectric properties of PZT films has been intensively investigated in literature, but the substrate effects on the electromechanical properties of PZT films still remain poorly understood due to complicated geometric constraints and the anisotropic nature of piezoelectric materials. Therefore, it is essential to investigate the effects of substrate clamping on piezoelectric properties of PZT films to construct highly functional piezoelectric MEMS devices and understand the scaling effects of piezoelectric materials.

1.2 Two main aspects in the substrate effects of PZT films

1.2.1 Mechanical properties of PZT films

It is well known with the PZT film structure that piezoelectric properties are dependent on the material’s mechanical properties [9, 10], due to the plane stress state.

Moreover, delamination, cracking or brittle fracture, and fatigue degradation of PZT composite structures are directly related to mechanical behaviors [11-13], which should be understood for proper design of the structure to prevent failures under large strain conditions. Therefore, the scaling effects of PZT films' mechanical properties must be determined for the optimization of piezoelectric MEMS devices.

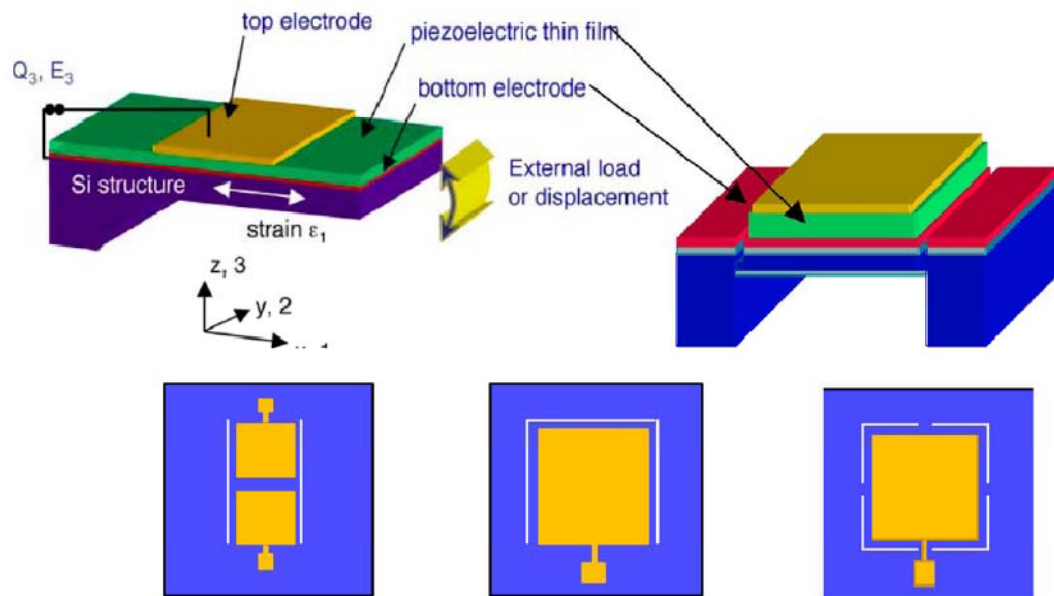

Figure 1-1 Laminated PZT/Si deflecting structures used in piezoelectric MEMS: bridge, cantilever and suspended membrane.[1]

1.2.1.1 Geometric constraint due to substrate

Among the methods used to characterize the mechanical properties of films such as impulse acoustic method, micro-beam cantilever deflection technique, atomic force microscopy etc. [14, 15], the nanoindentation technique can exhibit high sensitivity without requiring the removal of the film from its substrate; however, experimental

results of the film usually include information on both film and substrate. Thus, it is not trivial to extract the true mechanical properties of PZT films. The substrate effect must be understood to distinguish the individual contributions of film and substrate to measured mechanical properties.

1.2.1.2 Orientation of piezoelectric films

PZT films can form in a textured or oriented crystalline direction by combined mechanisms of preferred nucleation and growth kinetics. Nucleation of a crystal on a substrate is usually the dominant factor or rate determining step since the energy barrier for such nucleation is much higher than the activation energy for growth[16]. Since heterogeneous nucleation on a substrate typically occurs during PZT film fabrication, the film can be textured when there is lattice matching between the substrate and a specific PZT plane. For example, (111) oriented PZT films are commonly obtained on (111) oriented platinized silicon substrates with Ti adhesion layers [12, 17, 18]. If lattice mismatch between PZT and substrate occurs, it was considered that a (100) texturing may dominate. Due to charge considerations, the (100) face has the lowest surface energy and will act as the fast growth direction [19, 20]. Thus, if PZT continues to nucleate heterogeneously on a substrate, (100) crystallites will be dominant due to their fast growth kinetics [20].

Properties of a PZT film are anisotropic due to crystalline orientation. Therefore, the control of crystalline orientation tailored by processing conditions, microstructures, composition and their electromechanical response in PZT films have been studied

intensively. However, the crystalline orientation dependence of PZT films on nanomechanical properties has rarely been investigated [12, 17, 18]. Since highly oriented crystalline films are required for piezoelectric MEMS devices to obtain designed electromechanical properties, it is necessary to investigate the orientation effects on the mechanical properties of PZT films.

1.2.2 Electric properties of pMEMS structure with varying Si thickness

MEMS typically cover the following components: mechanical microstructures, microsensors, microactuators, and microelectronics [21], as shown in Figure 1-2.

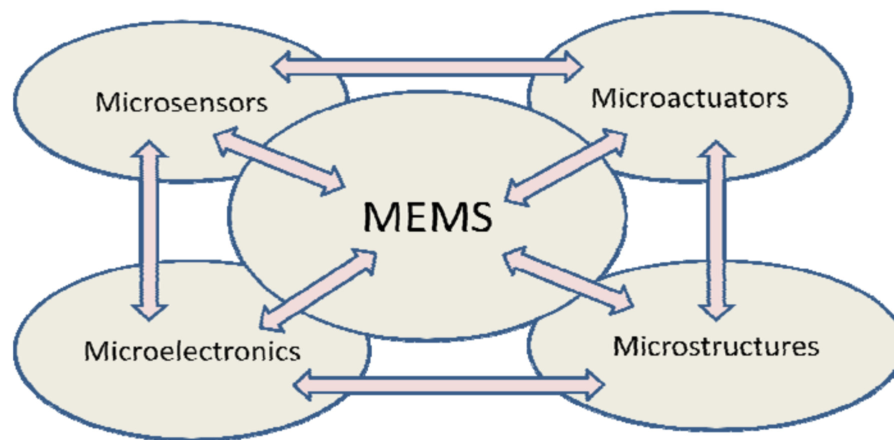

Figure 1-2 A schematic illustration of MEMS components and their interconnection

MEMS have broad applications such as motion sensors, pressure and force sensors, small actuators as well as a number of acoustic and ultrasonic devices, among others [22]. In the past 20 years, MEMS technology has achieved significant progress through the introduction of a variety of functional materials including piezoelectric material. This material has attracted the most attention because it provides a range of advantages such as fine resolution, large force generation, fast response time, zero

magnetic fields, low power consumption, vacuum and clean room compatibility and the ability to operate at cryogenic temperatures [23]. Unfortunately, during the fabrication of PZT films, residual stress may be induced upon cooling due to structural and thermal mismatch between the film and the substrate. Such residual stress could lead to cracking or delamination of the structure, thus degrading the performance of the devices [24]. Although different methods such as controlling composition, texture, thickness and poling condition have been tried to compensate for residual stress, the substrate effect on the residual stress distribution is rarely reported. With backside etching of the substrate, i.e. variation of Si thickness, the device may experience relaxation due to the released constraint from the substrate [25]. Since the change in mechanical constraint from a Si substrate can influence the electromechanical properties of PMEMS devices, it is necessary to investigate Si thickness dependence on the properties of piezoelectric devices.

1.3 Research objective and dissertation structure

1.3.1 Research objective

The objective of this work is to perform a systematic investigation on the substrate clamping effects of ferroelectric films and freestanding ferroelectric MEMS structures (PZT cantilever in this work) by addressing both experimental and analytical methods. To accomplish this goal, research will be conducted in the following aspects:

1) The influence of substrate type on the mechanical and electric properties of PZT films is investigated. PZT films with different thicknesses and orientations will be deposited onto two kinds of platinized Si substrates. The mechanical properties of the films will be measured by nanoindentation and the experimental results will be analyzed based on a modified discontinuous elastic interface transfer model. The corresponding electric properties of the PZT films will also be characterized.

2) The influence of Si substrate thickness on the electromechanical properties of PZT cantilevers is studied. PZT cantilevers will be designed and fabricated. The thickness of Si substrates will be controlled by varying the backside etching time through Dry reactive ion etching (DRIE). An analytical solution will be given to predict the change of the properties of PZT cantilevers.

1.3.2 Dissertation structure

This dissertation consists of six parts. Chapter 1 introduces the motivation and the research objective. Dissertation structures are given in this chapter as well.

Chapter 2 gives the theoretical background, including backgrounds on piezoelectricity and piezoelectric materials. The development of analytical solutions for determining the mechanical properties of films are reviewed and current research about investigating the mechanical properties of PZT films are introduced as well. Finally, PZT MEMS devices and fabrication backgrounds are summarized.

Chapter 3 presents the process for fabricating PZT films on different substrates and the measurement of mechanical and electrical properties of the obtained PZT films. In this chapter, the substrate effect is discussed in detail.

Chapter 4 studies the orientation effect on the mechanical properties of PZT films on SiO_2 and SiNx -based substrate. A modified discontinuous elastic interface transfer model was employed to extract the true orientation effect.

Chapter 5 investigates the influence of varying Si substrate thickness on the electrical and piezoelectric properties of the PZT cantilevers. A numerical model was developed to predict the residual stress distribution in the PZT cantilever.

Chapter 6 describes the overall conclusions and suggested work for the future study.

Chapter 2 Literature Review

2.1 Piezoelectricity and piezoelectric materials

Piezoelectric materials are at the heart of the piezoelectric MEMS devices (sensors or actuators). An understanding of the development of crystal structure, microstructure, and properties of these materials is necessary for the structural design and process integration of piezoelectric MEMS devices. In this section, piezoelectric materials are reviewed, beginning with a short description of piezoelectricity in general, followed by the introduction of common piezoelectric material and their properties structure and lastly, Lead Zirconate Titanate (PZT).

2.1.1 Piezoelectricity

Piezoelectricity is a material property that linearly relates applied stresses to induced dielectric displacements (direct piezoelectric effect) or applied electric fields to induced strains (converse piezoelectric effect). The direct piezoelectric effect has been widely applied to various sensors design, such as accelerometer, pressure sensor etc. While different actuators, for instance, piezoelectric motors, utilize the converse piezoelectric effect to convert electrical energy into a mechanical displacement or stress.

The constitutive equations that describe above two effects in regard to electric and elastic properties are [4, 9]

$$x_{jk} = d_{ijk} E_i \quad \text{or} \quad \sigma_{jk} = -e_{ijk} E_i \qquad \text{(converse effect)} \qquad (2\text{-}1)$$

$$D_i = d_{ijk} \sigma_{jk} \quad \text{or} \quad D_i = e_{ijk} x_{jk} \qquad \text{(direct effect)} \qquad (2\text{-}2)$$

where σ, x, E, D , are the stress, strain, electric field and electric displacement, respectively. d and e are the piezoelectric coefficients.

Since film materials are usually used in a composite structure, which is different from bulk materials, the total elastic properties are often dominated by the other part of the structure such as layer components (silicon oxide, silicon nitride etc). Therefore, the solution of the equations of state will be necessary to explain piezoelectric response resulting from substrate clamping. Equation (2-3) and (2-4) are defined as the piezoelectric constitutive equations which relate the electric and elastic variables of a piezoelectric materials [9, 26].

$$x_{ij} = s^E_{ijkl} \sigma_{kl} + d_{ijk} E_k \qquad (2\text{-}3)$$

$$D_i = d_{ikl} \sigma_{kl} + \varepsilon^{\sigma}_{ij} E_j \qquad (2\text{-}4)$$

$i, j, k, l = 1, 2, 3$, where $s^E_{ijkl}, d_{ikl}, \varepsilon^{\sigma}_{ij}$ represent, respectively, the compliances (at constant electric field), the piezoelectric coefficients and the dielectric constant (at constant stress). The number of unique coefficients in Equations (2-3) and (2-4) depends on the symmetry class of the materials. For a polycrystalline film, the symmetry can be expressed as ∞mm (equivalent to a six fold symmetry axis). The relevant equations in this case are:

$$x_1 = s^E_{11} \sigma_1 + s^E_{12} \sigma_2 + s^E_{13} \sigma_3 + d_{31} E_3 \qquad (2\text{-}5)$$

$$x_2 = s^E_{11} \sigma_2 + s^E_{12} \sigma_1 + s^E_{13} \sigma_3 + d_{31} E_3 \qquad (2\text{-}6)$$

$$x_3 = s_{13}^E(\sigma_1 + \sigma_2) + s_{33}^E\sigma_{33} + d_{33}E_3 \tag{2-7}$$

$$D_3 = \varepsilon_3^T E_3 + d_{31}(\sigma_1 + \sigma_2) + d_{33}\sigma_3 \tag{2-8}$$

For the measurement of the piezoelectric properties of films, one has to keep in mind that the film is always clamped to a substrate. Therefore, the piezoelectric coefficients obtained from the measurement are effective coefficients. For the inverse effect, with no applied stress (σ_3=0), the ratio of the elongation in length (Δl) to the applied voltage V can be written as

$$\Delta l / V = \left(x_3 / E_3\right) = d_{33} + s_{13}^E(\sigma_1 + \sigma_2) / E_3 \tag{2-9}$$

As the film is clamped to a much thicker substrate, the displacements in axes 1 and 2 are not allowed and therefore $x_1 = x_2 = 0$. We also assume that the substrate is the dominant element and that it is isotropic, then $\sigma_1 = \sigma_2$ due to symmetry reasons. By combining Equation (2-5) to (2-9), we can obtain:

$$x_1 = (s_{11}^E + s_{12}^E)\sigma_1 + d_{31}E_3 = 0$$

$$-d_{31}E_3 = (s_{11}^E + s_{12}^E)\sigma \rightarrow \sigma / E_3 = -d_{31} / \left(s_{11}^E + s_{12}^E\right) \tag{2-10}$$

$$d_{33,f} = \Delta l / V = d_{33} - 2d_{31}s_{13}^E / (s_{11}^E + s_{12}^E) \tag{2-11}$$

Equation (2-11) gives the effective d_{33} value. From Equation (2-10), the effective e_{31} value can be obtained:

$$e_{31,f} = \sigma / E_3 = -d_{31} / (s_{11}^E + s_{12}^E) \tag{2-12}$$

Both effective coefficients can be measured directly and are very important for predicting piezoelectric response of devices.

2.1.2 Piezoelectric materials

In the past years, numerous researches were conducted to develop piezoelectric material since Jacques and Pierre Curie brothers discovered the piezoelectric effect. Till now, different types of piezoelectric materials have been available such as single-crystal or highly oriented polycrystalline ceramics (e.g. zinc oxide and quartz), organic crystals (e.g. ammonium dihydrogen phosphate or ADP), poled polycrystalline ceramics (e.g. lead zirconate titanate, PZT), and polymers (e.g. polyvinylidiene fluoride or PVDF), as shown in Table 2.1.

Table 2.1 Properties of some piezoelectric materials

Material	d_{31}(pC/N)	d_{33}(pC/N)
ZnO(thin film)	-5.1 [27]	10.5~11.5 [28]
Quartz(Single crystal)	-	2.3 [29]
PVDF(Oriented film)	28 [30]	20 [31]
ADP(Single crystal)	d_{36}=48 [30]	-
AlN(thin film)	-2 [32]	4 [32]
PZT(polycrystalline)	-190~-320 [33]	390~650 [33]
PZT(thin film)	-30~-110 [34]	190~250 [28]

From this table, we can see that PZT has higher piezoelectric constants for MEMS devices where the application requires larger displacement under certain applied electric field or vice versa. Therefore, with the increasing desire of miniaturization of electronic devices, PZT material attracts most intensive attention by providing design versatility

and performance advantages over both single phase ceramic and polymer piezoelectric materials in both sensing and actuating applications [35].

PZT materials have the perovskite structure (ABO_3) in cubic, tetragonal, rhombohedral, and orthorhombic forms, depending on the temperature and composition, as shown in the Figure 2-1 [30].

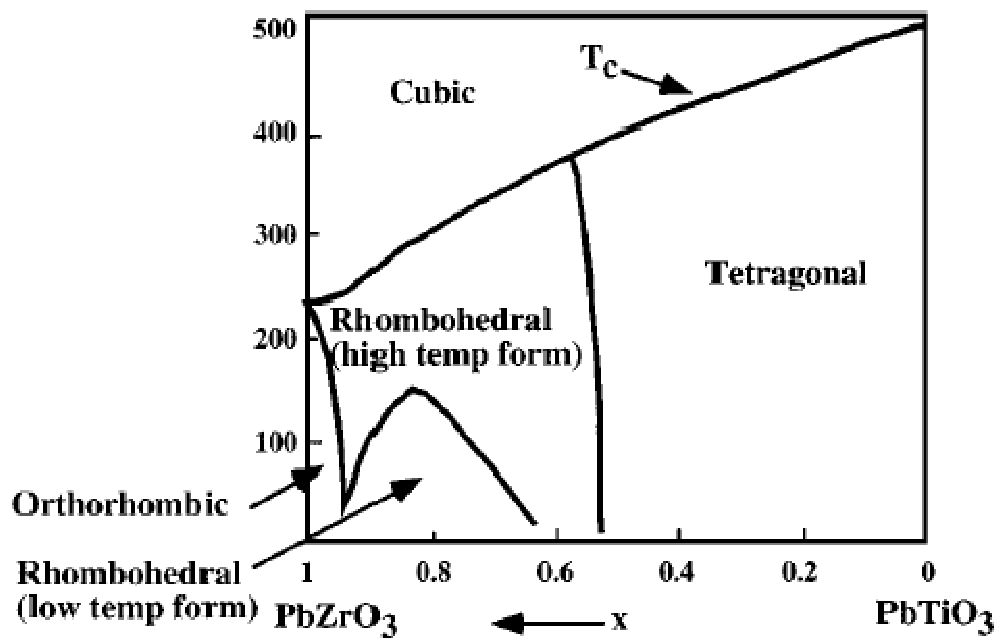

Figure 2-1 Phase diagram for the $PbZrO_3$-$PbTiO_3$ system

PZT at room temperature is a solid solution of lead titanate $PbTiO_3$ and lead zirconate $PbZrO_3$. This solid solution gives the communally named PZT (Lead Zirconate Titanate). Its crystal structure above the Curie temperature has a cubic unit cell (Figure 2-2).

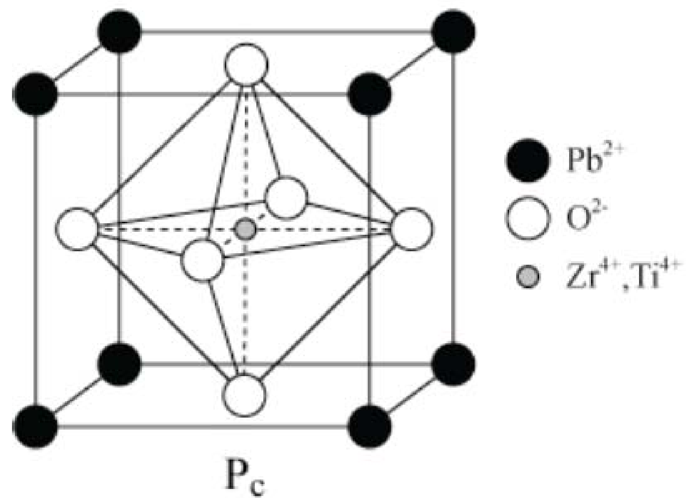

Figure 2-2 Perovskite crystal structure of paraelectric PZT above its Curie temperature

The structure can be considered as a face-centered cubic derivative structure in which the larger Pb cation and oxygen anion together form a face-centered cubic lattice. The smaller Ti and Zr cations occupy the octahedral sites in the face-centered cubic array and have only oxygen anions as their nearest neighbors. When the crystal is cooled down through its Curie temperature, it undergoes a phase transition from the cubic paraelectric (Pc) state to ferroelectric state. A spontaneous polarization occurs because the oxygen and titanium ion are shifted relatively to the lead ions. The distortion of the lattice is rhombohedral (F_R) for zirconium-rich compositions and tetragonal (F_T) for the titanium-rich compositions (Figure 2-3).

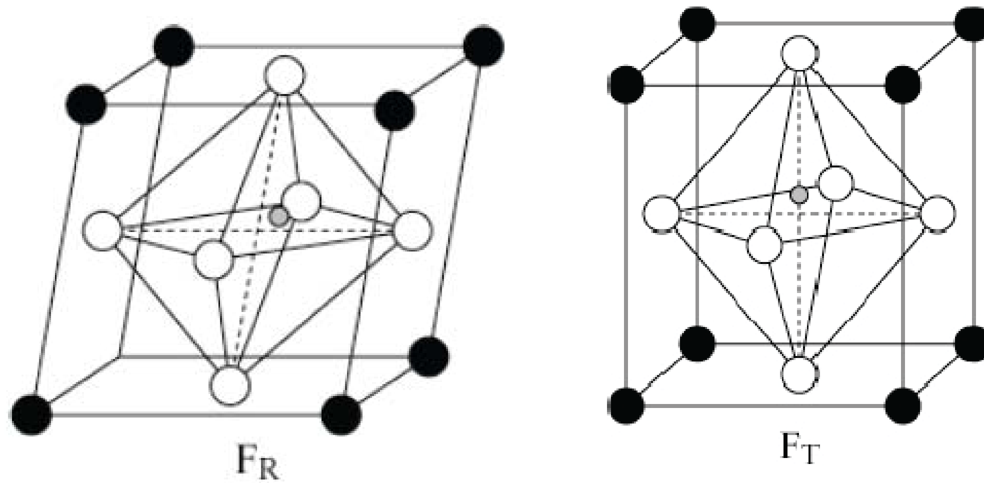

Figure 2-3 Perovskite crystal structure of rhombohedral (F_R) and tetragonal (F_T) PZT

In the case of the tetragonal distortion, six equivalent directions for the polarization can occur, whereas eight are possible in the rhombohedral case. At the morphotropic phase boundary (MPB), both phases coexist since they have an equal probability to form. This leads to fourteen different possibilities for the direction of the spontaneous polarization and thus to a peak of the piezoelectric and dielectric properties. At room temperature, the MPB is situated at ~53% Zr.

2.2 Mechanical properties of thin film

Mechanical properties are the response of a material to an externally applied load, such as elasticity, compressivity, tensile strength, deformability, hardness, wear resistivity, brittleness, cleavability, etc. The mechanical properties depend on the chemical bonding and the crystal structure. Anisotropic mechanical properties appear in crystals with non-cubic structures because of the directionality of the atomic bonding and their arrangement in a crystal. For bulk materials, testing methods to determine

mechanical properties are well established, such as tensile testing for strength, elasticity, and ductility; impact test for impact resistance and toughness; Rockwell, Brinell, or Vickers test for hardness [36, 37]. However, the mechanical properties of films may be quite different from those of their bulk materials because of unique microstructure, large surface-to-volume ratio, reduced dimensions, and the constraints caused by the substrate [38, 39]. Therefore, the techniques for measuring the mechanical properties of thin films are also different from those for bulk materials.

2.2.1 Techniques for measuring mechanical properties of thin film

As mentioned in the first chapter, mechanical characterization is essential for the design and analysis of MEMS devices. As techniques to measure the mechanical response of thin films, there are micro-tensile test [40-43], impulse acoustic method [44], Brillouin light scattering [45], X-ray diffraction [46], substrate curvature technique [47-49], and nanoindentation [11-15, 17, 18, 50-54].

In the micro-tensile test, tensile force is usually applied by piezoelectric motor and the generated strain or displacement will be detected by laser-based interferometry. The process has the following requirement:

1) A specimen film that attached on the Si substrate or die.
2) Resistance of the specimen material to the Si etchant.
3) Excellent adhesion between specimen material and substrate .

The micro-tensile can be a straightforward method to measure both Young's modulus and yield stress from thin films by using same general procedure employed for bulk samples

at a much smaller scale [40, 43]. However, there are difficulty in clamping method and avoiding bending in a sample, which limits its broader usage.

As far as the impulse acoustic method, Hurley et al. [44] developed laser-ultrasonic methods to evaluate the elastic properties of thin films. They used broadband surface acoustic waves (SAWs) generated by a line-focused, pulsed laser. Then the SAWs were detected by a Michelson interferometer. Based on displacement waveforms obtained from a range of source-detector separations, a dispersion relation for the phase velocity vs. frequency was calculated. With a developed inversion algorithm, the dispersion relation was employed to get the quantitative elastic-property information of the thin films.

Djemia et al. [45] utilized Brillouin light scattering (BLS) to investigate the elastic properties of polycrystalline and smooth fine-grained diamond films deposited on a titanium alloy by a two-step microwave plasma-assisted chemical vapor deposition. In the BLS experiment, a beam of monochromatic light is used as a probe to reveal acoustic phonons in a medium. The power spectrum of this excitation is mapped from frequency analysis of the light scattered within a solid angle by means of a multipass Fabry-Perot interferometer. The acoustic modes confined within the film were then decided and the elastic constants therefore obtained.

Shute and Cohen [46] used an X-ray diffraction method to determine the mechanical properties of Al–2% Cu films on oxidized Si wafer substrate. They measured the change of thermal residual stress, caused by the difference in thermal expansion coefficients between the film and substrate with changing temperature. The yield strengths of passivated samples were obtained at different film thickness. However, for

some materials, the reduced temperatures may not be low enough to yield the samples. Thus, this method will not be applicable for universal thin film system.

Bader et al. [47] used a substrate curvature technique to study the mechanical properties of hot and cold sputtered Si or Cu-doped Al films on silicon wafer during thermal cycling. The stress-temperature curves were constructed accordingly. However, at elevated temperatures, annealing and recrystallization may occur in these thin films, and consequently influences the yield strength of the films.

Compared with the above methods, nanoindentation technique can have the following advantages:

1) High resolution [55]. (Depth Resolution <0.01 nm, Load Resolution 50 nN)

2) No need to remove the film from its substrate [15].

3) No extensive modeling to account for the anisotropy [17].

4) No special pre-treatment for the sample or experimental condition for running the test.

Besides, the test results provide plenty of information on the elastic modulus, hardness, strain-hardening, cracking, phase transformations, creep, fracture toughness, and energy absorption. Since the deformation during the indentation process is very small, the technique is applicable to explore the mechanical properties of thin surface films and surface modified layers. Commonly measured properties using Nanoindnetation are elastic modulus and hardness. Both can be measured as a function of depth of penetration into the specimen surface, thus providing a depth profile of these properties.

A schematic [56] and an image of a nanoindentation system were given in Figure 2-4 and 2-5. Figure 2-4 shows three basic components of the system: an indenter transmitting the force with a specific geometry, an actuator to apply the force, a sensor recording the indenter displacement. Figure 2-5 is the actual nanoindentation setup.

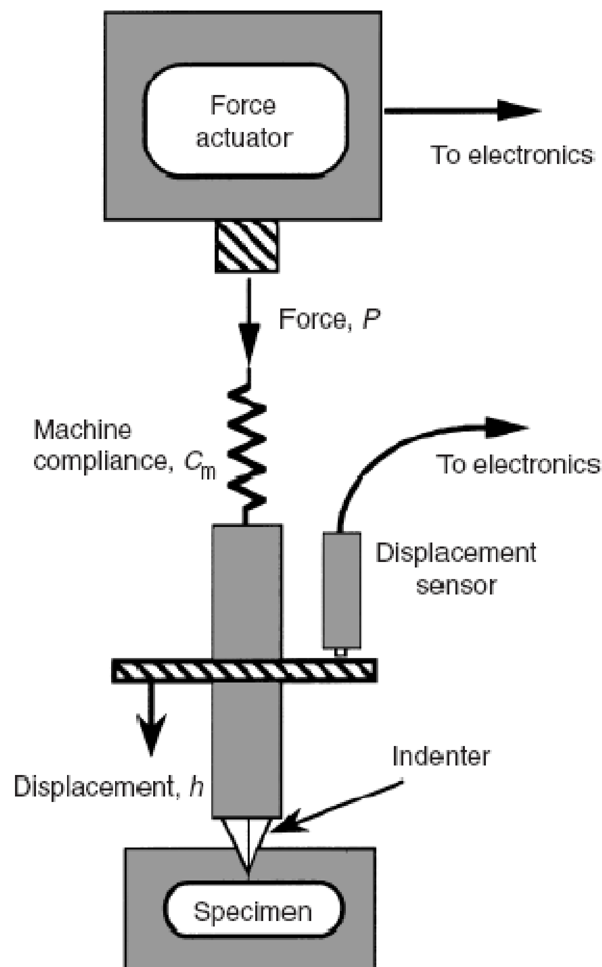

Figure 2-4 A sketch of nanoindentation system

Nanoindentation tests were performed using a nano-indenter with combination of a continuous stiffness method (CSM) and static method. First of all, the sample which will be fixed on the stage need to load in the chamber. Next step is to predefine and

control loading path through the software, which determine the penetration of a diamond tip in the sample material under test. During the indentation sequence, the applied load P is continuously measured at the corresponding displacement h. Based on above processes, load-displacement data P=f(h) is obtained from a complete loading-unloading cycle yielding the elastic modulus, E, and the material's hardness, H. A typical load-displacement curve and the deformation pattern of an elastic-plastic sample during and after indentation are shown in Figure 2-6 [57]. h_{max} represents the displacement at the peak load, P_{max}. h_c is the contact depth and is defined as the depth of the indenter in contact with the sample under load. h_f is the final displacement after complete unloading. S is the initial unloading contact stiffness.

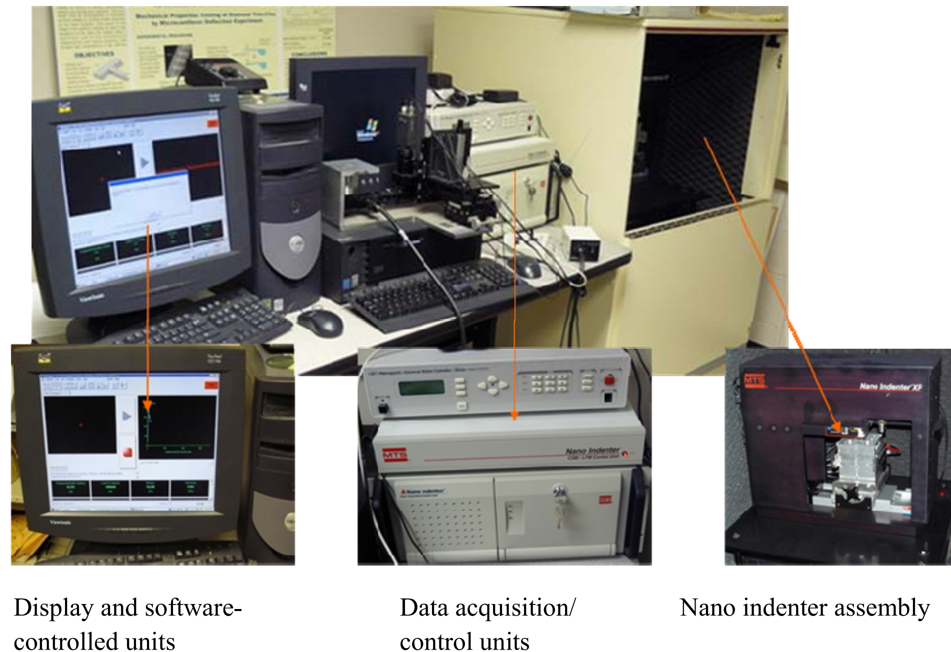

Figure 2-5 Nanoindentation system for the measurement of mechanical properties of PZT films

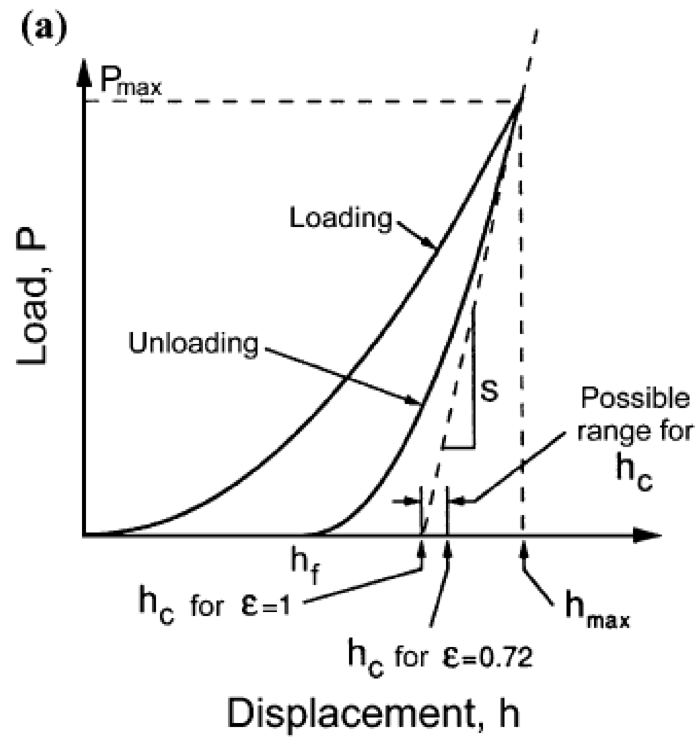

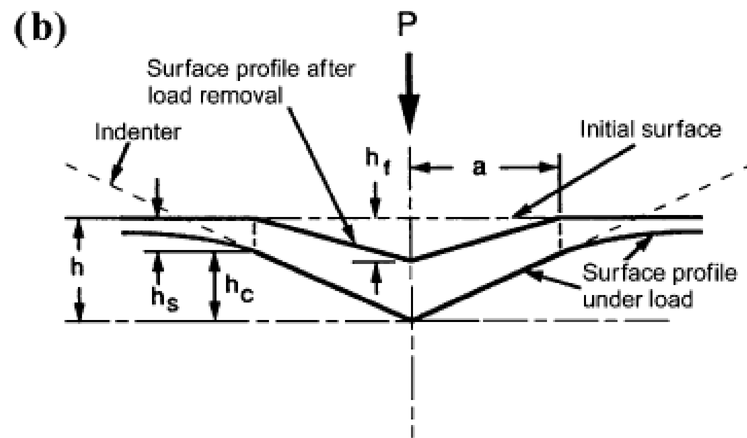

Figure 2-6 (a) A typical load–displacement curve and (b) the deformation pattern of a sample during and after loading

The hardness is defined as the indentation load divided by the projected contact area A of the indentation. From the load-displacement curve as shown in Figure 2-6, the hardness can be calculated by:

$$H = \frac{P_{max}}{A} \tag{2-13}$$

The Sneddon's elastic solution for the indentation of an elastic half space by any punch [58] related the contact stiffness S and the projected contact area A between indenter and half space to the elastic properties:

$$S = 2\beta\sqrt{\frac{A}{\pi}}E_r \tag{2-14}$$

where β is a constant determined by the geometry of the indenter (β = 1.034 for a Berkovich indenter). E_r is the reduced elastic modulus which accounted for the elastic behavior involved in both the sample and the indenter. It has the following form:

$$E_r = \frac{1-\nu^2}{E} + \frac{1-\nu_i^2}{E_i} \tag{2-15}$$

where E and ν are the elastic modulus and Poisson's ratio for the sample, respectively, and E_i and ν_i are the elastic modulus and Poisson's ratio of the indenter. For diamond, the elastic constants E_i and ν_i are equal to 1,141 GPa and 0.07[50, 59].

2.2.2 The development of analytical solutions for determining the mechanical properties of thin films

In 1992, Oliver and Pharr [60] proposed an analysis method to determine the hardness and elastic modulus from load-displacement curves of indentation for bulk

materials. In the method, the nonlinear unloading curve is described by a power law (Equation 2-15) with empirically determined parameters:

$$P = B\left(h - h_f\right)^m \tag{2-15}$$

where B and m are empirically determined parameters.

The contact stiffness S is calculated by differentiating the power law function.

$$S = \left(\frac{dP}{dh}\right)_{h=h_{\max}} = Bm(h_{\max} - h_f)^{m-1} \tag{2-16}$$

The projected contact area is a function of the contact depth for an indenter with a known geometry. The area function for a perfect Berkovich indenter can be expressed as:

$$A_c = 24.56h_c^2 \tag{2-17}$$

Since the indenters are not perfectly sharp in practical use, the area function needs to be calibrated as the following expression:

$$A_c = 24.56h_c^2 + C_1h_c^1 + C_2h_c^{1/2} + C_3h_c^{1/4} + \cdots + C_8h_c^{1/128} \tag{2-18}$$

where C_1 through C_8 are constants. The first term accounts for a perfect Berkovich indenter, the others describe deviation from the Berkovich geometry due to blunting of the tip.

The contact depth can be estimated as:

$$h_c = h - \varepsilon\frac{P}{S} \tag{2-19}$$

where ε is a constant decided by the indenter geometry ($\varepsilon = 0.75$ for a Berkovich indenter).

The Oliver-Pharr method was initially developed for exploring mechanical properties of bulk materials, not for films on substrates. Therefore it does not include any

information about a possible substrate. However, the Oliver-Pharr method is frequently used by researchers to investigate the approximate mechanical properties of thin films without considering the possible effect of substrate on the measurement. The accuracy of the measurement results by directly using this method depends on the film and substrate properties as well as the ratio of the indentation depth to the total film thickness. Generally, the introduced inaccuracy caused by the substrate effect increases with increasing indentation depth and elastic mismatch between film and substrate [61-63]. An often-used guideline to minimize the effect of the substrate on the measurement is that the substrate effect is negligible if the indentation depth is less than 10% of the film thickness [64]. In most cases, this rule of thumb is applicable. However, when the film is very thin or the elastic mismatch between film and substrate is large, applying this rule may result in inaccurate results. Evidently other methods must be developed for dealing with the substrate effects.

Numerous investigators have used different approaches to study the substrate effect for extracting 'true' film properties from nanoindentation of film/substrate composites. King [65] modeled the elastic indentation of a layered half space with numerical method. Indenters with three different geometries (sphere, square and triangle) were employed in the calculation. The solution related the effective indentation modulus of the composite structure to the indentation depth and the indenter size normalized by the film thickness. A function α of the indentation depth to film thickness ratio was also constructed, reflecting the substrate effect. Unfortunately, his model didn't give a clear solution for exploring the thin film modulus value.

Gao et al. [66] employed an approximate first-order perturbation method to calculate the thin film young's modulus. The reduced modulus of the film/substrate composite system was determined in closed form as the weighted average of the indentation moduli of the film and the substrate, as shown below:

$$E = E_s + (E_f - E_s) \cdot \Phi \tag{2-20}$$

where Φ is the weighting factor depending on the ratio of film thickness and contact area radius.

$$\Phi = \frac{2}{\pi}\arctan\left(x\right) + \frac{1}{2\pi(1-\nu)}\left[\left(1-2\nu\right)x\ln\left(\frac{1+x^2}{x^2}\right) - \frac{x}{1+x^2}\right] \tag{2-21}$$

Gao's model, however, becomes increasingly inaccurate as the elastic mismatch between the film and the substrate increases [67]. With a slight modification of the expression, the accuracy of Gao's model for the reduced modulus could be improved [68].

Saha and Nix modified King's results in order to analyze elasto-plastic indentations performed with a Berkovich punch [63]. In the analysis, they replaced the film thickness in King's model with a new parameter: the film thickness minus the instantaneous indentation depth. This is equivalent to changing the Berkovich tip to an "effective" flat punch during the elastic recovery in unloading process from an elasto-plastic indentation. The modified model fits well as the indent depth is less than 50% of the film thickness; however, it overestimates the substrate effect at relatively deep indentation depths [63, 69].

Chen and Vlassak [67] used finite element method to study the elasto-plastic indentation of a film on a substrate. They defined a substrate effect factor and provided a relationship between the contact stiffness and contact area. This relationship was later

employed by Han et al. [69] to determine the hardness of a thin film on the substrate. Han's method can estimate the instantaneous projected contact area from the contact stiffness. However, it cannot be used to measure the indentation modulus of the thin film a *priori*. Application of this method needs to know the elastic properties of the film and substrate in advance.

Besides above mentioned works, there are also many investigators who utilized experimental [61, 70-73] and theoretical methods [74-77] to study the substrate effect in nanoindentation. However, most of them just gave the measured modulus of thin film/substrate composite and the developed models partially fitted with the nanoindentation data-either at small indentation depth or at large depth. Moreover, without being verified by a wide range of film/substrate composites with different modulus, the models must be used with caution.

Recently, Zhou and Prorok [78] developed a discontinuous elastic interface transfer model based on Doerner and Nix model. Their simulation results showed that the elastic strains occurred in thin film and substrate were not continuous (Figure 2-7). Based on the results, two weighting factors were introduced in the model and accounted for the different developed strain fields in thin film and substrate, separately, during the indentation process.

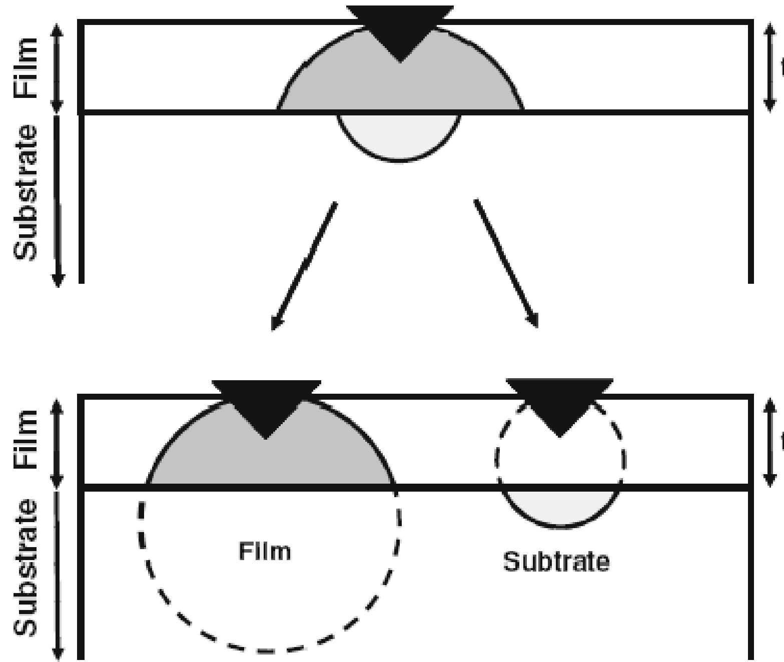

Figure 2-7 A schematic diagram showing different strain fields in the film and substrate

The modified model was shown as below:

$$\frac{1}{E^{'}} = \frac{1}{E_{f}^{'}}(1-\Phi_{s}) + \frac{1}{E_{s}^{'}}\Phi_{f} \qquad (2\text{-}22)$$

where $E^{'}$ is the measured modulus, $E_{f}^{'}$ is the film modulus=$E_{f}/(1-\upsilon_{f}^{2})$, $E_{s}^{'}$ is the substrate modulus= $E_{s}/(1-\upsilon_{s}^{2})$, and $\Phi_{f} = e^{-\alpha_{f}(t/h)}$ and $\Phi_{s} = e^{-\alpha_{s}(t/h)}$ are the weighting factors to account for the effects of the film on the substrate and substrate on the film, respectively. t is the film thickness, h is the indentation depth and α_{f} and α_{s} are the constants for the film and substrate respectively, corresponding to their bulk Poisson's ratios. By performing nanoindentation experiments on thirteen different amorphous thin films on a silicon substrate, the model was found to fit well with the experimental data. However, since the model was constructed based on one substrate, they decided to extend the investigation to more combinations of 5 films on 5 substrates to see if the model is

still applicable [79]. Experimental results indicated that the substrate significantly influenced the mechanical behavior even at penetration depths less than 2 % of the film thickness ,therefore, the measured flat region value at small indentation depth seems strongly depend on the substrate other than the thin film. To extract the true film modulus from the measured flat region value, a power function (Equation 2-23) was proposed and the discontinuous model was modified accordingly (Equation 2-24).

$$\frac{\Delta E_f^{'}}{E_f^{'}} = \left(\frac{E_s^{'}}{E_f^{'}}\right)^{0.1} - 1 \tag{2-23}$$

$$\frac{1}{E^{'}} = \frac{1}{E_f^{'}}(1-\Phi_s)\bullet\left(\frac{E_f^{'}}{E_s^{'}}\right)^{0.1} + \frac{1}{E_s^{'}}\Phi_f \tag{2-24}$$

Comparing with Equation (2-22), the additional term $\left(\frac{E_f^{'}}{E_s^{'}}\right)^{0.1}$ accounts for the early influence of the substrate. Thus, the true Young's modulus of the films can be extracted from the measured flat region value by using Equation (2-24).

2.2.3 Mechanical properties of PZT films

The deposition processing, orientation control, microstructures, composition and electromechanical properties of PZT films have been studied extensively [80-90]. However, very few studies have been conducted to investigate the mechanical properties of PZT films. Examples of reports are summarized in Table 2.2.

Bahr et al. [11] studied mechanical properties and fracture characteristics of PZT films by nanoindentation. A 600nm (111) PZT film was deposited on a 1 cm^2 platinized

Si substrate by a sol-gel method. The Oliver and Pharr method was employed to measure the modulus of the thin films. The obtained values are ranging from 130 to 160GPa. According to the calculated elastic strain, however, they found that the indentation process likely exceeded the elastic strain over which the PZT behaves in a linear elastic manner. Therefore, the low-load indentation is required to measure the modulus in a non-linear elastic manner.

In Fang et al. [51]'s study, a 500nm (110) PZT film was deposited on a platinized Si substrate by RF magnetron sputtering. Three different annealing temperatures were used in the fabrication of PZT film through RTA (rapid thermal annealing). The annealing temperature dependence of mechanical properties was investigated by nanoindentation.

The results are shown in Figure 2-8. The Young's moduli of those thin films ranged from 109.17 to 260.04GPa and differed with various annealing temperatures and indentation depth. The authors ignored the possible substrate effect at the beginning of the nanoindentation process. Therefore, the reported data may not be able to represent the true values of PZT films.

Wang et al. [18] studied the crystal orientation dependence of PZT films on nanomechanical properties. By varying processing conditions, PZT film with strong (001), (111). or random orientations were prepared on platinized silicon substrates. The one-tenth rule of thumb was employed to measure the Young's moduli of the PZT films and the obtained average values of PZT films with (001) and (111) orientations are 165 and 145 GPa, respectively. The moduli of the PZT film with random orientation ranged from 125 to 190 GPa. Based on the results, the authors concluded that the distinct

Young's moduli of the PZT films were caused by the different orientation. However, as mentioned in previous section, the one-tenth rule must be used with caution, especially when the film thickness is very thin. Without a comprehensive analysis of the raw data, the obtained mechanical properties and crystalline orientation relationships may not be accurate.

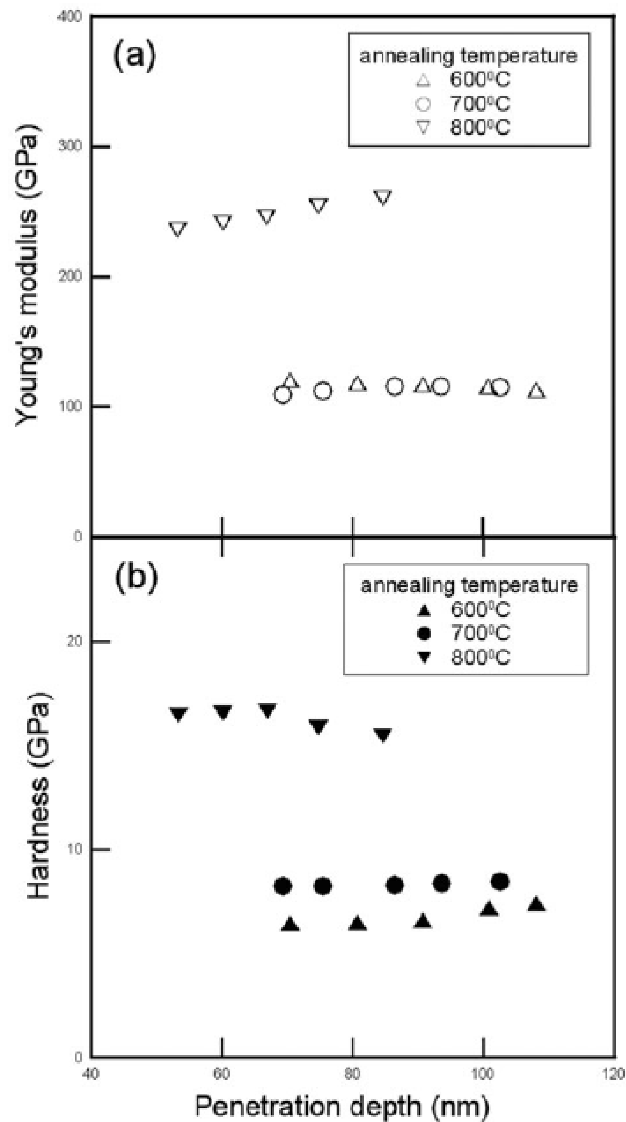

Figure 2-8 (a) Young's modulus and (b) the hardness as a function of penetration depth for PZT films annealed at 600,700 and 800^{0}C

Table 2.2 Current research status about the measurement of mechanical properties of PZT films

Thin film structures	**Experimental conditions**	**Conclusions**	**References**
Si(100)/SiO_2/Ti/Pt/PZT (Pt-111)	1 micron PZT films with (001),(111) and random orientation; the same thickness and similar microstructure	PZT films with different orientation show different Young's Modulus. E_{001}=165GPa, E_{111}=145GPa, E_{random}=125~190GPa (average value)	[18]
Si/SiO_2/TiO_x/Pt/PZT Si/SiO_2/$LaNiO_3$/PZT ($LaNiO_3$-001)	PZT films with (001),(110) and (111) orientation were obtained by varying deposition parameter such as bottom electrode, film thickness , and precursor	PZT films with different orientation show different Young's Modulus. E_{001}=180±5GPa, E_{111}=156±8GPa, E_{110}=125±10GPa	[14, 17, 50]
Si(100)/SiO_2/Ti/Pt/PZT (Pt-111)	500nm PZT films were fabricated at different annealing temperature: 600,700 and 800^{0}C	The Young's Modulus increased from109.17 to 260.04GPa as the rapid annealing temperature increased from 600 to 800^{0}C	[51]
Si(100)/SiO_2/Ti/Pt/PZT	600nm,1 micron PZT films	Obtained Young's Modulus is approximately 123GPa. The Young's Modulus may be influenced by underlying substrate.	[11, 15]
Si(100)/SiO_2/Ti/Pt/PZT	200nm PZT film	E_{100}=146.5GPa, E_{111}=161.2GPa, E_{random}=155.3GPa	[12]

Delobelle et al. [14, 17, 50] measured the mechanical properties of PZT films with different orientations on various electrodes. PZT film with different orientations

were fabricated by utilizing different electrode materials (Pt and LNO) and chelating agents (2-MOE and acetate acid). Nanoindentation experiments were performed at different indentation depths: 10%, 5% and 2.5% of the PZT film thickness. The data employing 2.5% of the film thickness as an indentation depth were used to calculate the mechanical properties of those PZT films. At small indentation depth, the authors found there was no occurrence of micro-cracks during the nanoindentation process and they considered that the results are free of substrate effect, representing the true moduli of the PZT films. Therefore, the experimental results present that the mechanical properties of the PZT films greatly depend on the crystalline orientation and the relationship can be represented by the following inequality:

$$E_{<110>} < E_{<111>} < E_{<001>} \tag{2-25}$$

Xu et al. [15] investigated the possible substrate effect on the measured mechanical properties of PZT film. 1 μm PZT film was deposited on platinized silicon substrates. The mechanical properties were measured by nanoindentation. For all indentation tests, the maximum penetration depth and tip force were limited within 250 nm and 10 mN, respectively. The results are shown in Figure 2-9. The reduced modulus and hardness of a PZT film show little variation when the indentation depth is lower than 60 nm. Furthermore, Xu et al employed Yu and Chen et al's model [67, 77] to calculate the induced error due to substrate effect, which was estimated to be less than 5% when the indentation depth is smaller than 60nm. Therefore, the measured values at small depth were considered to be true modulus of the PZT film. However, as Prorok and Bo's work indicated in previous section, even at small indentation depth (<2%), the results may be significantly influenced by the substrate, and the measured values are actually the

modulus of the composite. Therefore, Xu et al's work just examined the accuracy of the composite modulus and failed to extract the thin film modulus from the obtained data.

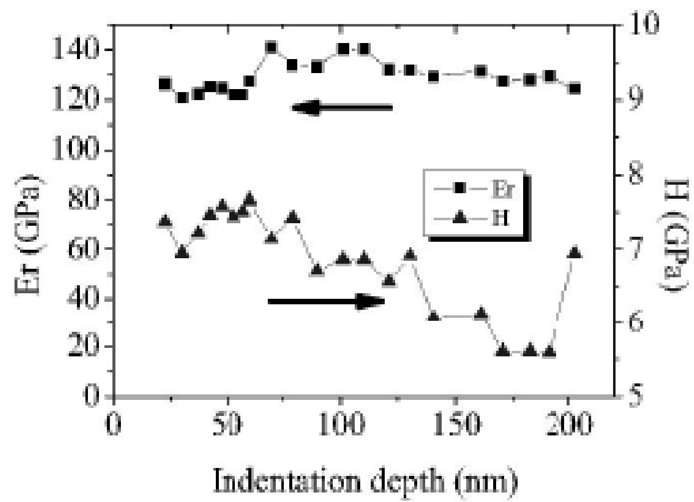

Figure 2-9 Reduced modulus (Er) and hardness (H) versus indentation depth for PZT films

Wu et al. [12] fabricated 200nm PZT films with different orientations under different annealing temperatures. The mechanical properties of those films were measured by nanoindentation and shown in Figure 2-10.

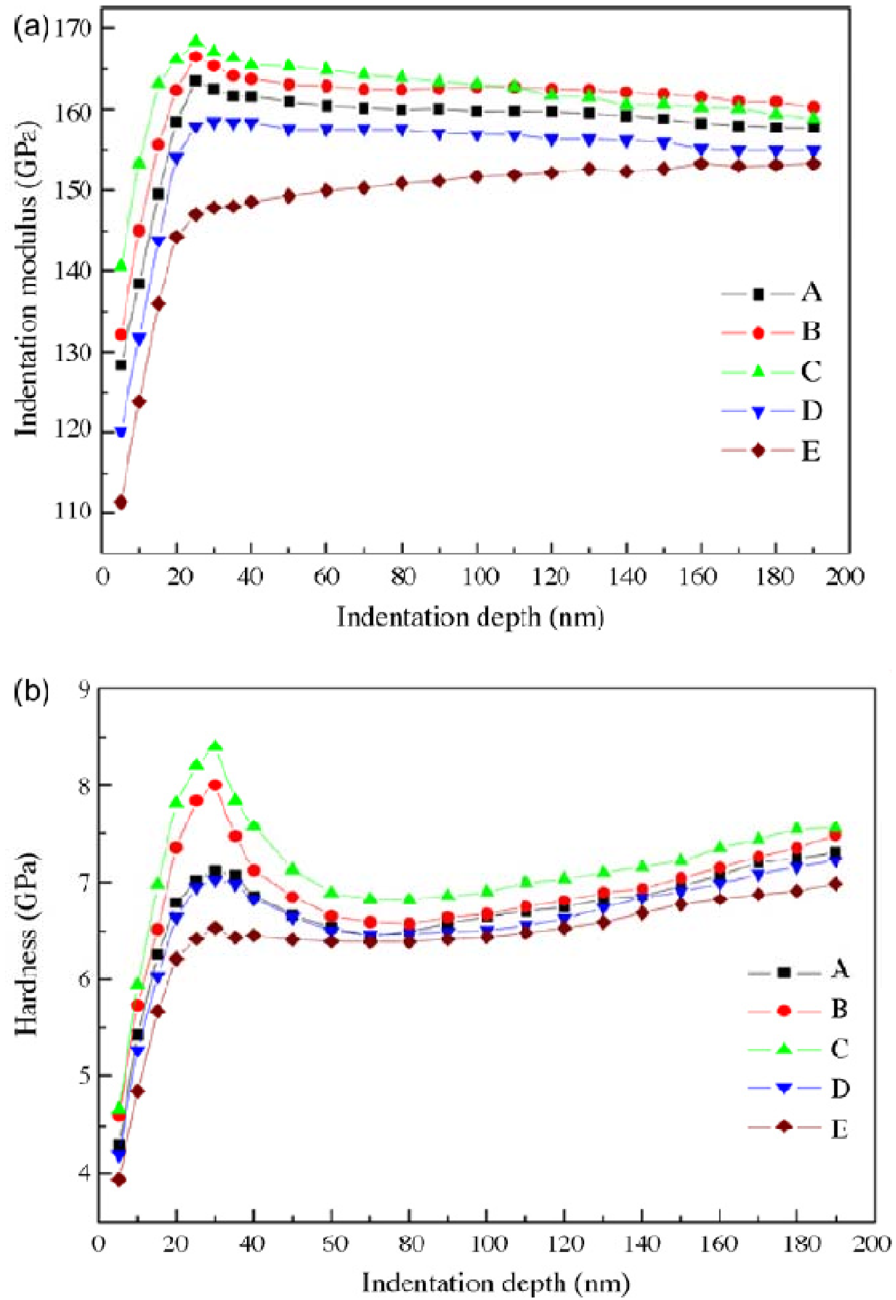

Figure 2-10 (a) Indentation modulus and (b) hardness of PZT films as a function of indentation depth

To avoid the considerable effect from a substrate, the values of indentation modulus and hardness of PZT films were determined when the averages of the data obtained from 5 to 15% of the total depth of PZT films.

Obviously, Wu et al. did not consider possible substrate effects at small indentation depth either. Therefore, the measured mechanical properties of PZT films can be inaccurate and the obtained orientation dependence of mechanical properties may not be reliable.

Through the literature survey, although a lot of efforts have been made to explore the mechanical properties of PZT films by many researchers, the substrate effects still remain unclear. Analytical methods have to be developed to extract the modulus of the PZT film from the raw nanoindentation data. Many models were introduced in previous section to study the substrate effects in two-layer structure. Since PZT film composite includes several layers, direct application of those models to PZT structures may not be reasonable. Therefore, research work should be focused to investigate the substrate effect via both experimental and analytical method based on current models.

2.3 PZT MEMS devices and fabrication background

Piezoelectric MicroElectroMechanical Systems (pMEMS) consists of at least two elements: a bulk silicon frame and a piezoelectric deflection element with electrodes [1]. During the last 30 years, micromachining of silicon has been developed and successfully used to manufacture a range of mechanical microstructures such as beams, diaphragms, grooves, orifices, sealed cavities, pyramids and needles. However, the need for specific functionality drives the development of integrating functional materials such as piezoelectric thin films into MEMS. The piezoelectric element can provide a direct transformation between a driving signal or read-out signal and a sensor or an actuator

parameter. The input and output parameters for actuator and sensor applications of piezoelectric laminated plates are schematically described in Figure 1-1.In an actuator, application of a voltage leads to a piezoelectric in-plane stress causing a deflection of the structure, whereas the piezoelectric thin film is strained in the out-of-plane direction. In the sensor mode, in-plane strains create the piezoelectric charges that record the deformation of the flexible structure.

The representative structures in MEMS are categorized into three configurations: diaphragm, bridge, and cantilever, as shown in Figure 1-1. The common processes for fabricating those devices include photolithography, pattern transfer with dry and wet etching techniques, and common thin films deposition (SiO_2, Si_3N_4, poly-Si, Al, Cr, Ni, and Au) [91]. Figure 2-11 [1] shows the typical process flow for the microfabrication of planar PZT/Si suspended membrane structures. It usually starts with an oxidized silicon wafer with one side polished. The SiO_2 is grown on the wafer by thermal oxidation, which is the electrical and diffusion buffer layer of PZT film structure. The adhesion layer (e.g. Ti/TiO_2), bottom and top electrode (e.g. Pt) are deposited by PVD sputtering. The Piezoelectric thin film is deposited by sol-gel CSD or by sputtering. Top electrode is patterned either by lift-off or by plasma dry etching. For accessing the bottom electrode, vias are opened through the PZT film by wet or dry etching. The front-side shape of the structure is patterned by using a lithography technique through Pt/PZT/Pt/Ti/SiO_2 stack and through Si defining the depth of groove. In general, the Si thickness is controlled by back-side deep reactive ion etch (DRIE). Table 2.3 summarizes typical materials used in pMEMS devices and fabrication details.

Table 2.3 Summary of typical materials used in pMEMS devices fabrication [1]

Materials	Growth methods	Thickness	Typical stress (MPa)	Patterning methods
Silicon wafer/SOI	Czochralski.bonding and polishing	390μm; 1~50 μm of device Si on buried SiO_2		DRIE; wet etching
Thermal SiO_2	Wet oxidation	Max. 2000nm	-300 ± 5	ICP plasma etching; wet etching (BHF)
Si_3N_4	LPCVD	Max. 200nm	0~ +700	ICP plasma etching
Pt bottom electrode	PVD sputtering	100~300nm	+550	ICP plasma etching
PZT 53/47 {100}	sputtering or sol-gel	500~40000nm	+100 (unpoled) +1800 (poled)	ECR/RF plasma etching wet etching (HCL/HF)
Au/Cr top electrode	PVD evaporation	100nm/10nm	+280	lift-off

To fabricate pMEMS device with high quality, a number of important issues should be addressed:

1) The deposition of uniform, high quality PZT to provide excellent electromechanical properties of devices.

2) The mechanical stress through the structure need to be compensated to avoid any residual bending.

3) The thickness of supporting Si substrate should be uniform and the border conditions should be defined precisely.

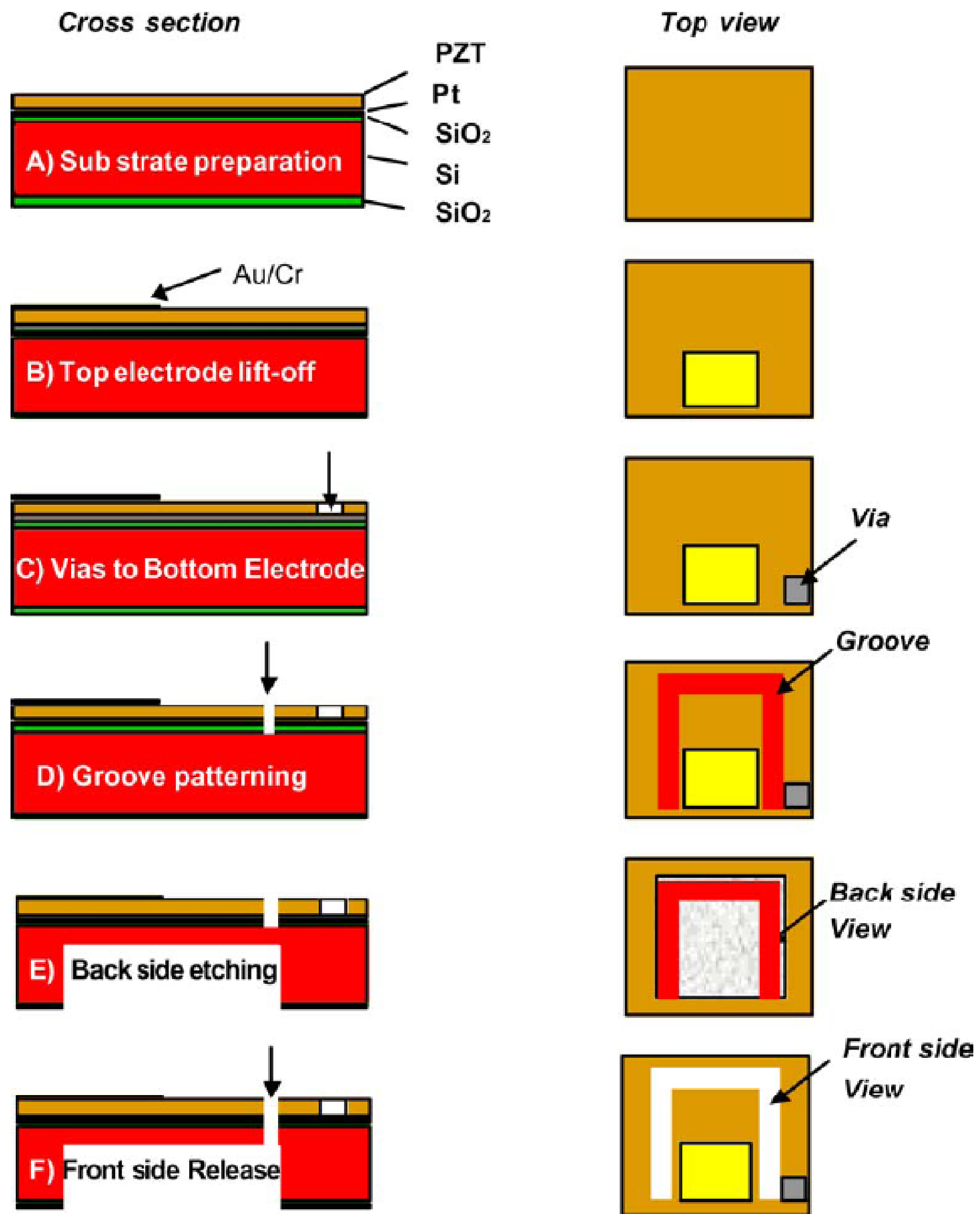

Figure 2-11 Typical process flow for the microfabrication of PZT/Si cantilever (cross section and top view)

For issue 1, numerous researchers [20, 30, 81-83, 86, 88, 89, 92, 93] had put their efforts to develop, optimize and fabricate PZT films with excellent properties. Utilizing SOI wafer and DRIE technique can greatly solve the problems in issue 3. However, the

precise control of the stress in PZT film and MEMS device still remain unclear. If the overall residual stress exists, serious bending (Figure 2-12) may occur, and it can degrade electrical-mechanical energy conversion or even destroy the device sensitivity.

Since the fabrication of ferroelectric thin films involves the growth of the film on a different substrate material and high temperature treatment, residual stress commonly build up in a film after processing. There are three types of residual stresses developed in thin film process: intrinsic stress, thermal stress, and extrinsic stress. Intrinsic stress can be produced by the formation of grain boundaries as the crystal grain grows and interacts with neighboring grains, shrinkage due to water and solvent evaporation, decomposition and pyrolysis of nonvolatile organic species during heat treatment, and by the phase transformation at the transition temperature. Thermal stress is induced by the mismatch between thermal expansion coefficients of the film and the substrate. The extrinsic stress originates from the lattice parameter mismatch between the film and the substrate. Residual stresses on the order of several hundred MPa have been reported for ferroelectric thin films [94-96]. The effects of residual stress on the electrical, mechanical and piezoelectric properties of the piezoelectric films have been reported [97, 98]. The change of remanent polarization, dielectric constant, domain structures due to residual stress was focused. Efforts to reduce or to compensate for such stress have been made via controlling process parameters.

Apparently, PZT films often exhibit a mechanical stress (tensile or compressive) that degrades the properties of the freestanding MEMS structures by deforming them. Although lots of research works including analytical and experimental methods have been pursued to investigate the influence of residual stress on the properties of PZT films,

few reports on the piezoelectric properties of MEMS devices are available. Development of analytical solutions in conjunction with experimental methods for exploring the influence of residual stress is therefore needed to design MEMS device for better performance.

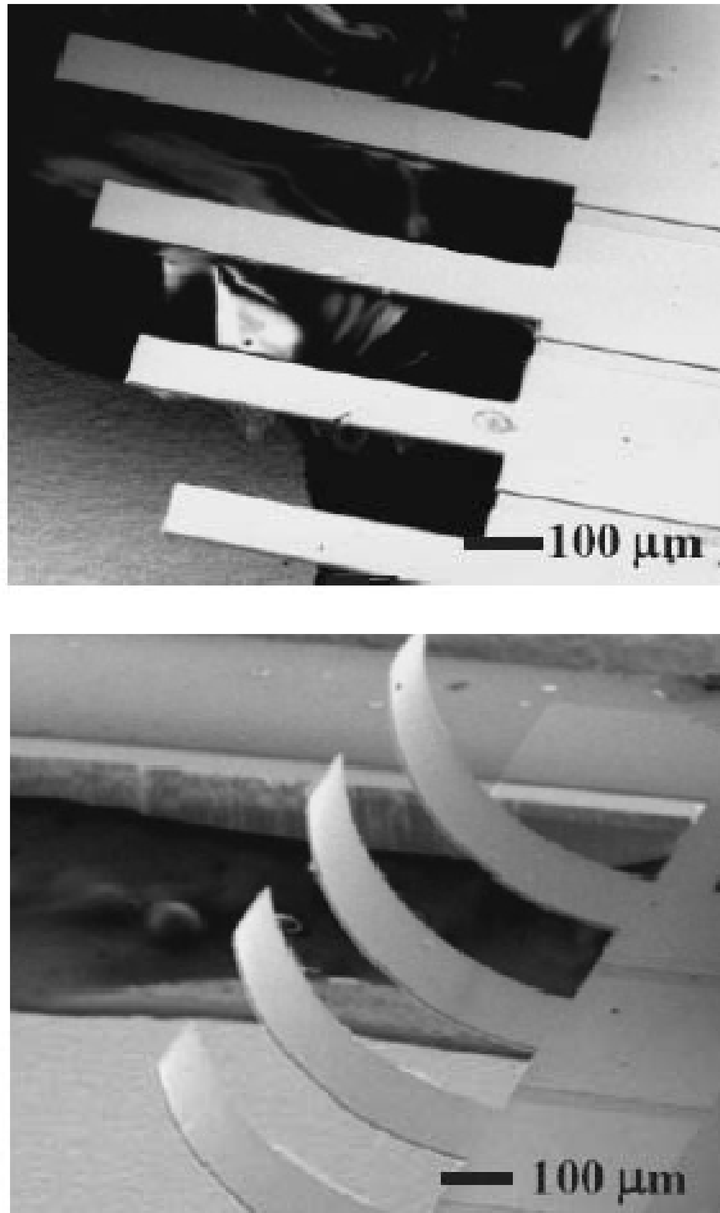

Figure 2-12 The effect of residual stress on ferroelectric PZT cantilever MEMS structure

Chapter 3 Investigation of the Effect of Substrates on the Measured Mechanical and Electrical Properties of PZT Films

3.1 Structure layer materials for MEMS devices - SiO_2 and SiNx

The most common material system for the fabrication of MEMS devices utilizes polycrystalline Si as a primary structural material, SiO_2 as the sacrificial material, and Si_3N_4 for electrical isolation of device structures [99]. In some fabrication routes, SiO_2 and SiNx are also used as a structure layer to construct MEMS devices.

Thermal oxidation and LPCVD are widely used techniques for the SiO_2 growth and deposition. SiO_2 is commonly used as a sacrificial material because it can be dissolved easily using etchants that do not attack polysilicon. In a less prominent role, SiO_2 is used as an etch mask for dry etching of thick polysilicon films because it is chemically resistant to dry polysilicon etch chemistries. Thermal SiO_2 is well known as an electrical insulator. The dielectric constants and dielectric strength of thermal oxide are 3.9 and 1.1×10^6 V/cm, respectively.

SiNx is widely used in MEMS for electrical isolation, surface passivation, and etch masking and as a mechanical material. Two deposition methods are commonly used to deposit SiNx thin films: LPCVD and PECVD. PECVD offers the potential to deposit nearly stress-free SiNx films, which is very useful in encapsulation and packaging. While

LPCVD SiNx is commonly used as an insulating layer to isolate device structures from the substrate and from other device structures because it is a good insulator with a resistivity of 106Ω-cm and a field breakdown limit of 10^7 V/cm.

In this study, they are used as the electrical and diffusion buffer layer during the CSD process and structure layer for the released MEMS structures. Table 3.1 shows some material parameters of SiO_2 and SiNx [100-102]. SiO_2 and SiNx present advantages in mechanical properties, which make them as good candidates to investigate the substrate effect on the properties of PZT films.

Table 3.1 Material properties of SiO_2 and SiN_x

Material	Density ρ, (kg/m^3)	Modulus *E* (GPa)	Hardness *H* (GPa)	Thermal expansion at 300K (10^{-6}/°C)	Thermal conductivity at 300K (W/m K)
SiO_2	2200	73	14~18	0.4~0.55	1.4
SiNx	3300	304	21	2.8	1.9

3.2 PZT film fabrication

There are different methods to deposit PZT films, including physical vapor deposition (PVD), such as flash and electrode beam evaporation [103], ion-beam deposition [104] and radio-frequency magnetron sputtering [105]; metalorganic chemical vapor deposition (MOCVD) [106]; and chemical solution deposition (CSD). Among them, the vacuum based deposition methods require large capital investments, while chemical solution deposition (CSD) method is easy to control material composition in

multicomponent systems, to produce uniform large area coatings and to cost less. Therefore, the CSD method was employed in this study for deposition of PZT films.

One of the CSD methods is sol-gel process [14, 17, 50, 92], which can be defined as a chemical elaboration of ceramic materials through synthesis of precursor solution, gelation of the sol, drying and pyrolysis of organics, and a crystallization at high temperature. The deposition is based on multiple spin coating of a liquid precursor on a platinized wafer. Pyrolysis is performed to decompose the residual organics at about 350^0C and then the annealing process is followed to crystallize the film at 650^0C.

The growth of high quality PZT films needs controlled conversion of as-deposited amorphous structure to a PZT crystalline phase. Usually, the crystallization consists of three stages. The amorphous phase can transform into oxygen deficient pyrochlore/fluorite structure, $Pb_2(Zr,Ti)_2O_{7-x}$, when heating in the temperature range of 350^0C to 600^0C. Above ~470^0C, the crystallization of perovskite phase can start. After long exposure above 700^0C, the formation of a lead deficient phase $Pb(Zr,Ti)_3O_7$ is observed at the surface of the film due to volatilization of PbO. However, the crystallization process may depend on a lot of factors or the combined conditions such as pyrolysis conditions, thermal treatments, annealing atmosphere, substrate electrode structure, solution chemistry, and the lead excess in the precursor.

In this study, the commercial PZT sol-gel solutions (Pb:Zr:Ti=110:52:48) (Inostek Inc.) were spin-coated on 10 × 10 mm^2 Pt(111)/Ta/SiO_2/Si and Pt(111)/Ta/SiNx/Si substrates at 4000 rpm for 20 seconds followed by drying at 150 ^{0}C for two minutes and pyrolysis at 300 ^{0}C for 10 minutes to remove residual organics. Such coating and pyrolysis treatments were repeated for 6, 9, 12 times to achieve the desired

thicknesses which are 580,830,1130nm, respectively and a pre-annealing process was carried out at 650 ^{0}C for 15 minutes every three times. After the thin films achieved the desired thicknesses, a final annealing was given at 650 ^{0}C for 1 hour. Figure 3-1 shows the schematic diagram for the preparation of PZT films.

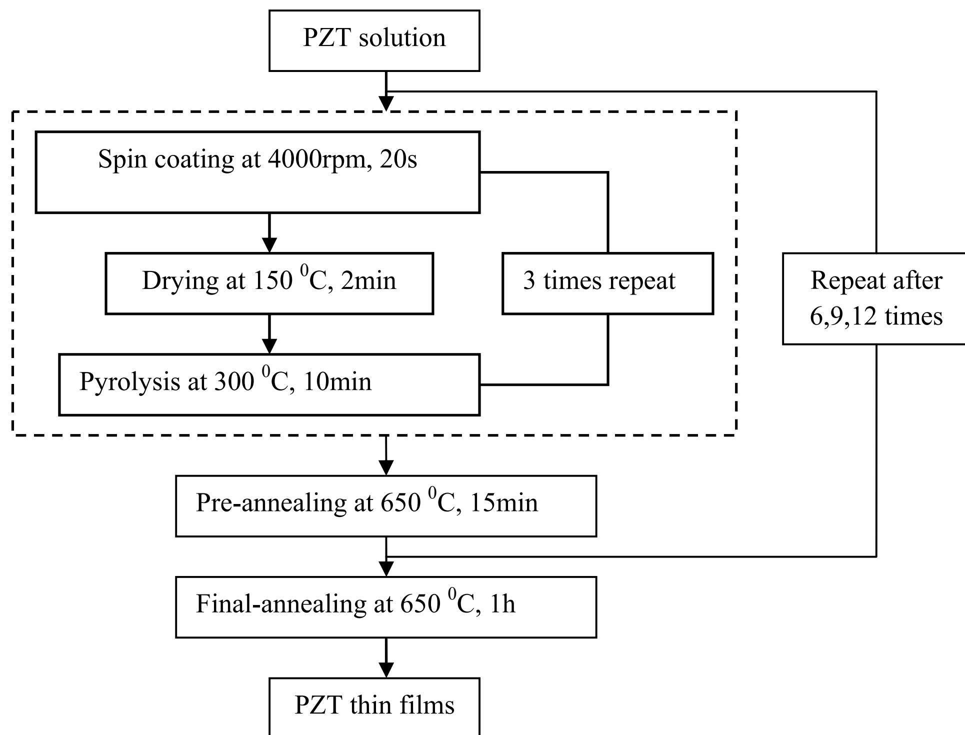

Figure 3-1 Schematic diagram for the preparation of PZT films

As mentioned before, SiO_2 and SiNx layers were grown on 4 inch Si wafers by using thermal oxidation and LPCVD, respectively, in microelectronics fabrication laboratory at Auburn University. The adhesion layer Ta (20nm) and electrode layer Pt (120nm) were deposited by magnetron sputtering system (deposition conditions refer to Appendix A).

3.3 Measurement of mechanical property of PZT films

3.3.1 Principle of measurement using nanoindentation

As introduced in chapter 2, based upon the method developed by Oliver and Pharr [60], the hardness and Young's modulus can be determined by an indentation load-displacement curve (Figure 2-6) according to Equation (2-13) and (3-1):

$$E = (1-\nu^2)\left[\frac{2}{\sqrt{\pi}}\beta\frac{\sqrt{A}}{S} - \frac{1-\nu_i^2}{E_i}\right]^{-1} \tag{3-1}$$

Equation (3-1) is obtained by substituting Equation (2-14) into Equation (2-15). When the mechanical properties of PZT films were measured by a nanoindentation method, the following statements were commonly advised:

1) The indentation depths were limited to less than a tenth of the thin film thickness (Figure 3-2a) (Here, The PZT sample with 12 times deposition was taken as an example) according to the one-tenth "rule of thumb" which suggests the measured mechanical property is very close to the true value of the films if a film has a thickness of ten times of the indentation depth [18, 107, 108]. And also microcracks and pile-ups do not occur in PZT films because the indentation depths are less than 20% of the film thickness [17]. As we can see from the curves of load-displacement in Figure 3-2a, no discontinuity is observed, which indicates no occurrence of micro-cracks in the indentation process [13, 14].
2) The Young's Modulus is obtained from the flat regions (Figure 3-2b) where the values are relatively constant and considered to be representative of the true film modulus [56].

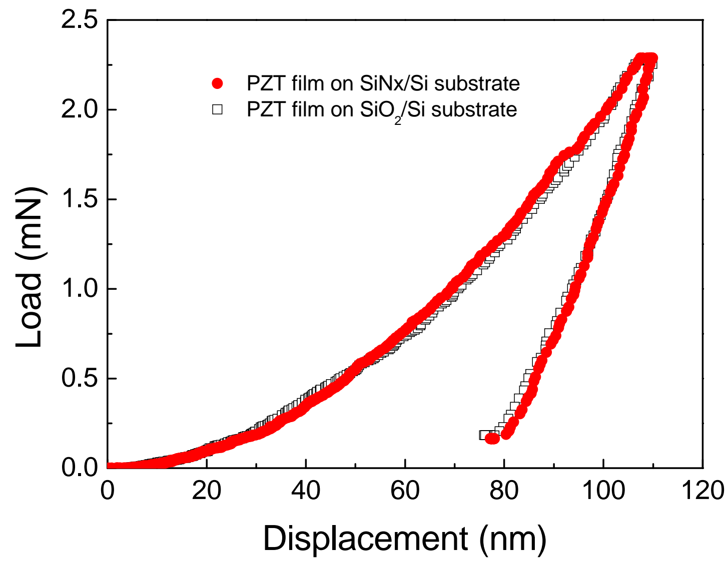

(a)

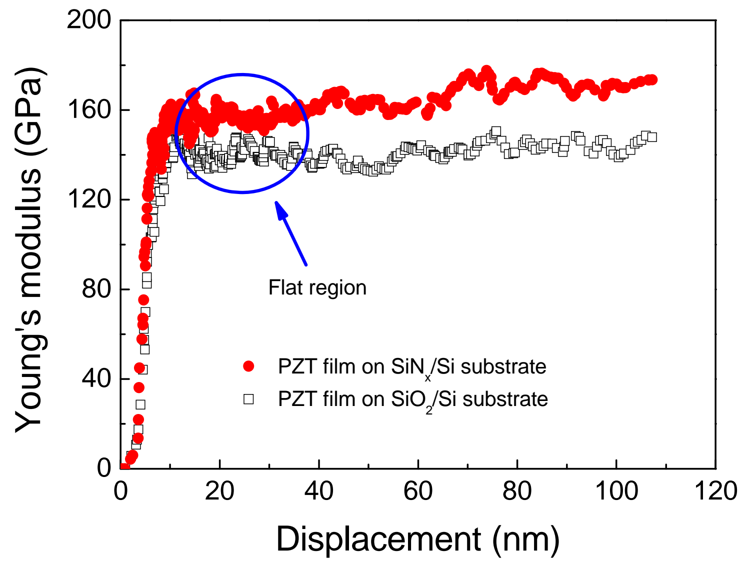

(b)

Figure 3-2 (a)Load-Displacement and (b) Young's Modulus-Displacement curves of 1130nm PZT films

3.3.2 Experimental setup of nanoindentation

Indentation tests were performed with an MTS Nanoindenter XP system at ambient pressure and temperature (Figure 3-3). The tip used in the nanoindenter system is a Berkovich diamond indenter. The system was fully calibrated using the fused silica as a standard sample before the measurements. The continuous stiffness method (CSM) was employed in the experiment. It was depth-controlled and the harmonic displacement target was set to 2 nm. The allowable thermal drift rate was limited as 0.05 nm/s. The corresponding Poisson's ratio of bulk material was employed as the one of the film. The Poisson’s ratio of the substrate was set as 0.28 for <100> silicon. For each sample, ~20 CSM tests were performed with same depth limitation. Film Young’s modulus was determined from the load-displacement curve and the CSM modulus-displacement curve.

Figure 3-3 Nano indenter assembly parts

3.4 Measurements of electrical properties and residual stress of PZT films

Prior to electrical measurements, platinum top electrodes were deposited at room temperature on PZT films through a shadow mask, using dc magnetron sputtering. The typical thickness of Pt top electrodes was 120 nm. A TF-2000 ferro/piezoelectric tester (aixACCT Systems GmbH, Germany) was used to measure field-induced polarization (Figure 3-4). The dielectric properties were characterized by using a HP 4192A impedance analyzer (Figure 3-5). The oscillation signal used was typically 10 kHz in frequency and 0.1Vrms in amplitude. Micro-stress within the PZT films was measured by Raman spectroscopy that was performed by using a 441.6 nm line from a He-Cd laser (80 mW). Raman spectra were collected using a spectrometer (JY-550) equipped with two 3-inch holographic gratings (2400 lines/mm, 3600 lines/mm), and a thermoelectrically-cooled charge coupled device (CCD) detector (2048 × 512 pixels).

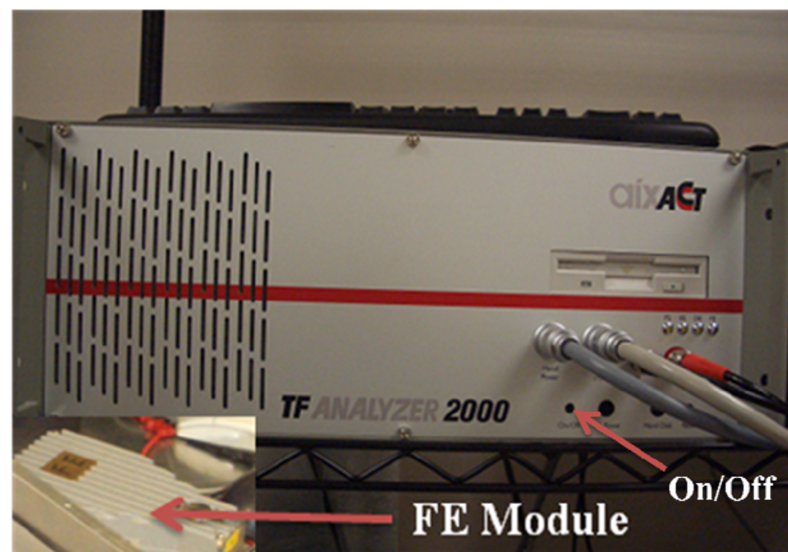

Figure 3-4 A TF analyzer 2000 for measuring piezoelectric properties of thin films

Figure 3-5 An impedance analyzer for measuring dielectric properties

3.5 Results and discussion

3.5.1 Mechanical properties of PZT films on different substrates

Three different thickness of PZT films and two types of structural layers were prepared and characterized. For each sample, 20 CSM tests were conducted at the same indentation depth. Figure 3-6 shows the evolutions of Young's modulus as a function of PZT thickness at different substrates. Since the preferred orientation and the microstructure of the PZT films can contribute to different mechanical properties [12, 17, 18, 50], all samples were characterized using scanning electron microscopy (SEM) and X-ray diffraction (XRD). Figure 3-7 shows the XRD patterns of PZT films prepared with different substrates and thin film thicknesses. All samples show strong (111) orientation because lattice matching between PZT and (111) platinum bottom electrode seems

dominant in these films irrespective of the types of structural layer [109]. Figure 3-8 shows the surface morphologies of the crystallized PZT films. Almost identical surface topography were observed and the grain sizes are in the range of 60-280nm. The above results indicate that the influences of orientation and microstructure on the measured Young's moduli of PZT films can be neglected. When comparing PZT films on different structural layers, the PZT films on SiNx-based substrates show higher Young's moduli than those on SiO_2-based substrates even at penetration depths less than 10% of the film thickness. These results indicate that the commonly used one-tenth rule may not be adequate to determine the true mechanical properties of PZT films grown on different substrates.

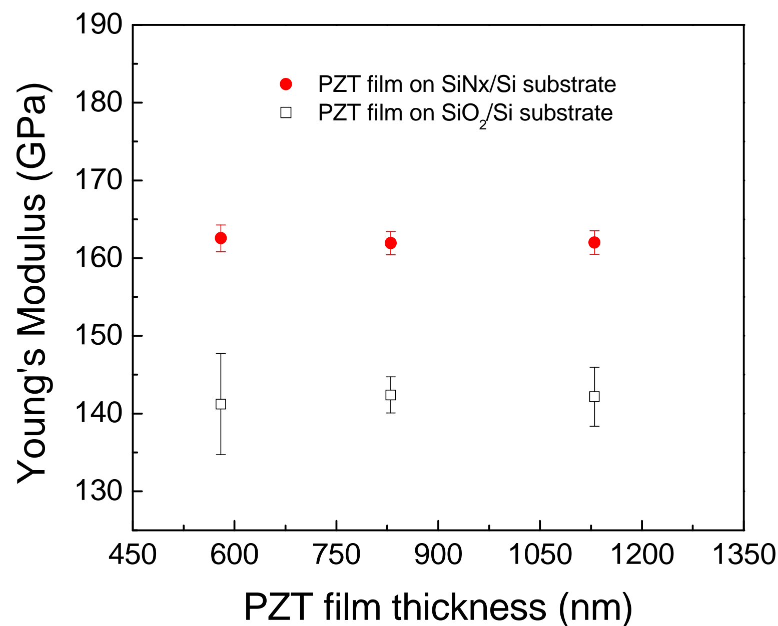

Figure 3-6 Young's Modulus as a function of the thickness of PZT films on SiO_2/Si and SiNx/Si substrates

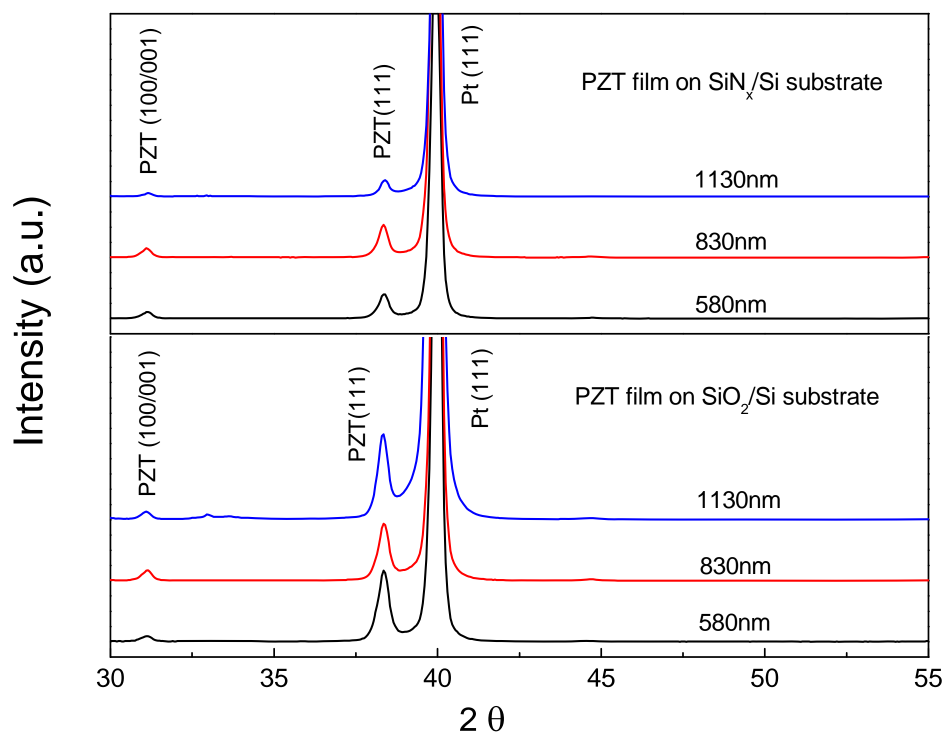

Figure 3-7 XRD patterns of PZT films with different substrates and thickness

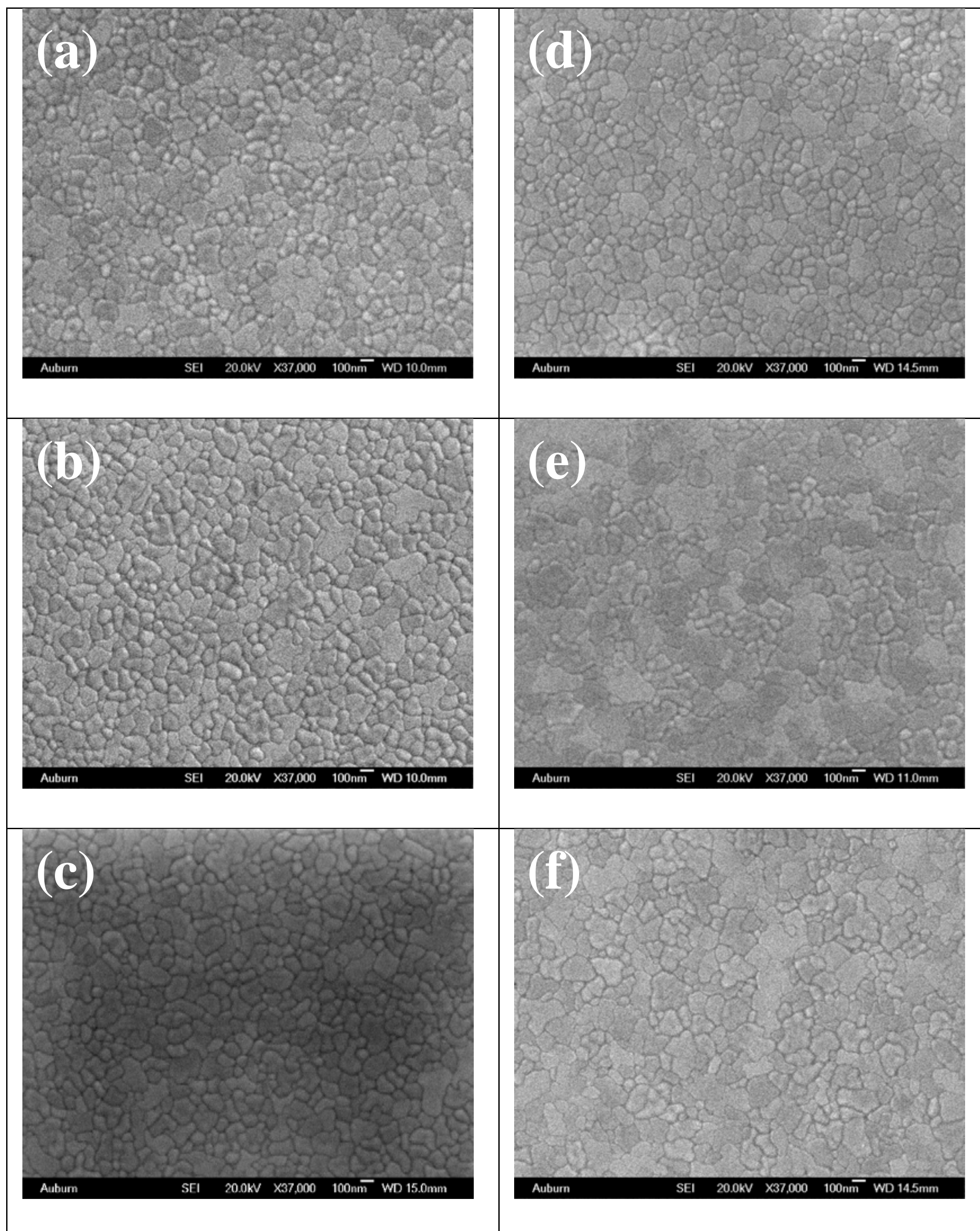

Figure 3-8 SEM images for PZT films on SiO_2/Si (left) and SiNx/Si (right) substrates with different thickness: (a)& (d)580nm; (b)& (e)830nm; and (c)& (f)1130nm (all have 60–280nm grain size)

Recently, Zhou and Prorok's work [79] proposed a two-layer model which works very well for 25 different combinations of 5 films on 5 substrates to extract the actual Young's modulus of a thin film on a substrate. The obtained data revealed that the flat region to determine the true Young's modulus does not solely depend on the film. In fact, the substrate may greatly influence the mechanical properties even at indentation depth less than 2% of the film thickness. Therefore, for the PZT multilayer structures employed in current experiments, the flat region may be influenced by substrates in more complicated ways. In order to clearly identify the influence of the substrate on the mechanical properties of PZT films, it is better to measure over a long range of indentation depth instead of 10% of the film thickness.

To explore the substrate effect as the function of the indentation depth, the 2,200nm was chosen as the depth limit. Since the Young's modulus of the PZT film does not change evidently with increasing film thickness (Figure 3-6), which may be attributed to similar orientation and microstructure of PZT films at different thicknesses, we only employed the PZT films with 12 times deposition. Figure 3-9 shows the evolutions of Young's modulus versus the indentation depth of PZT films on two different substrates.

For the PZT film on SiNx-based substrate, the measured Young's modulus increases as the indentation depth increases until the depth reaches around 300nm. Then the value decreased until the fracture point is observed at the indentation depth of 1,122nm where the PZT film and substrate become separated, which can be clearly observed by the load-displacement curve (Figure 3-10). The discontinuity on the loading curve indicates there was delamination and cracking occurring at the PZT/Pt interface,

which was then proved by the SEM picture as shown in Figure 3-11. The delamination and corresponding discontinuity on load-displacement curve were also reported by other researchers [13, 14].

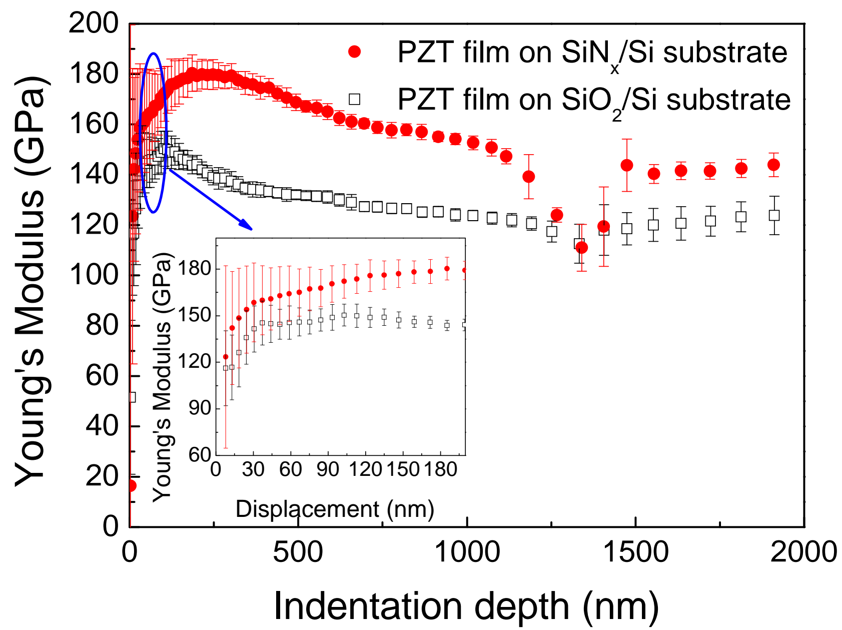

Figure 3-9 Young's modulus as a function of displacement with 2200nm depth limit for PZT on SiO_2/Si and SiNx/Si substrates

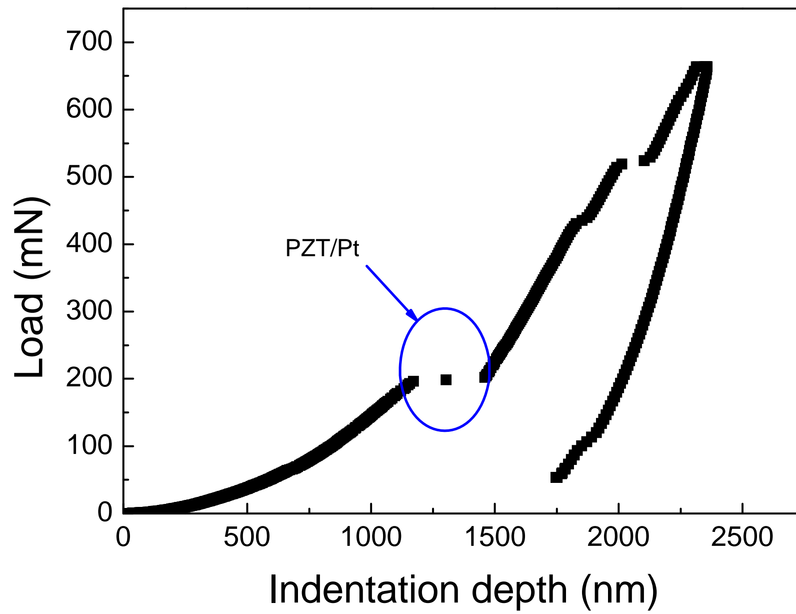

Figure 3-10 Load-displacement curve of PZT film on SiNx-based substrate with 2,200nm depth limit indicating fracture point

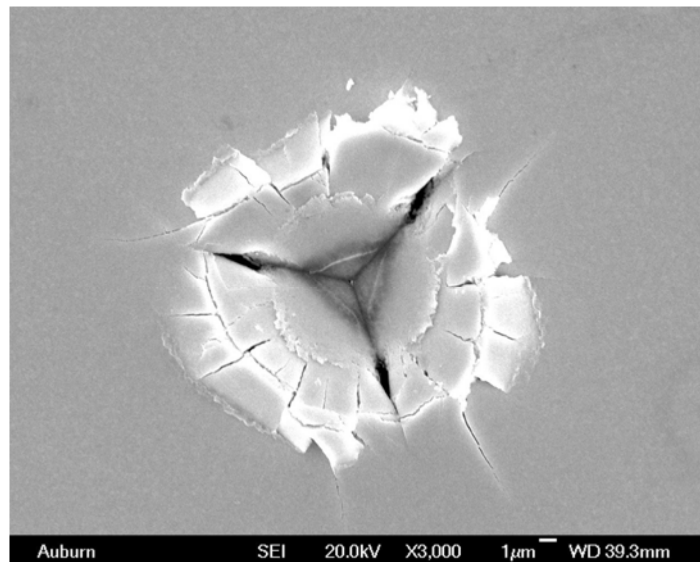

Figure 3-11 SEM showing delamination and cracking around indentation

For PZT film on SiO_2-based substrate, the curve shows very similar trend to the one of PZT film on SiNx-based substrate. However, the difference on maximum modulus

value and the position of fracture point clearly show the influence of substrates on measured results. As shown in the Figure 3-9, the maximum modulus value of the PZT film on SiO_2-based substrate was obtained around 200nm, which is smaller than that of the PZT film on SiNx-based substrate. At the early stage of the nanoindentation, the modulus increases as the indentation depth increases when the harder Pt thin layer dominates the substrate effect. The measured modulus of the PZT film on SiO_2-based substrate soon decreases due to the influence of softer SiO_2 substrate, while the measured value of PZT film on SiNx-based substrate still increases because of harder SiNx substrate. After reaching the maximum value, the measured moduli and the modulus difference between two set of samples gets smaller when the Si layer is dominating the substrate effect as the indentation depth increases. It should be pointed out that, in a multilayer structure, the substrate effect is attributed to the combined effect from different layers during the nanoindentation measurement. Therefore, the measured values of the PZT films on SiNx-based substrate are always larger than those of the PZT films on SiO_2-based substrate even when an indenter penetrates into the Si substrate. The facture point was observed at the indentation depth of 1,255nm which is larger than the one of PZT film on SiNx-based substrate, and the reason is probably since the softer SiO_2 layer is able to absorb more applied strain [110].

The hardness change as a function of the indentation depth is also given in Figure 3-12. The measured hardness of PZT films on two substrates are almost same (~8.8GPa) until the indentation depth is approximately below 400nm. As the indentation depth increases, the hardness values become different probably due to the occurrence of delamination and buckling in the PZT structures. However, the interfacial cracks do not

propagate extensively [13]. The measured hardness of PZT film on SiNx-based substrate is slightly smaller than the one of PZT film on SiO_2-based substrate, probably because the SiN_x layer can absorb less applied strain compared to SiO_2 layer as mentioned above, which may result in more severe fracture and larger contact area. According to equation (3-1), the smaller hardness vaule of PZT film with SiNx-based substrate was expected, but the difference is very small (<1GPa) because the interfacial cracks have not propagate extensively yet. When the indentation depth is above 1,100nm, the serious delamination occurs in both structures and results in larger difference on measured hardness. We should notice this difference caused by the contact area change is not so significant (maximum difference being ~ 2GPa). Based on equation (3-2), the effect of the square root of the contact area change on measured Young's modulus is even negligible compared with the substrate effect, except for the complete fracture condition.

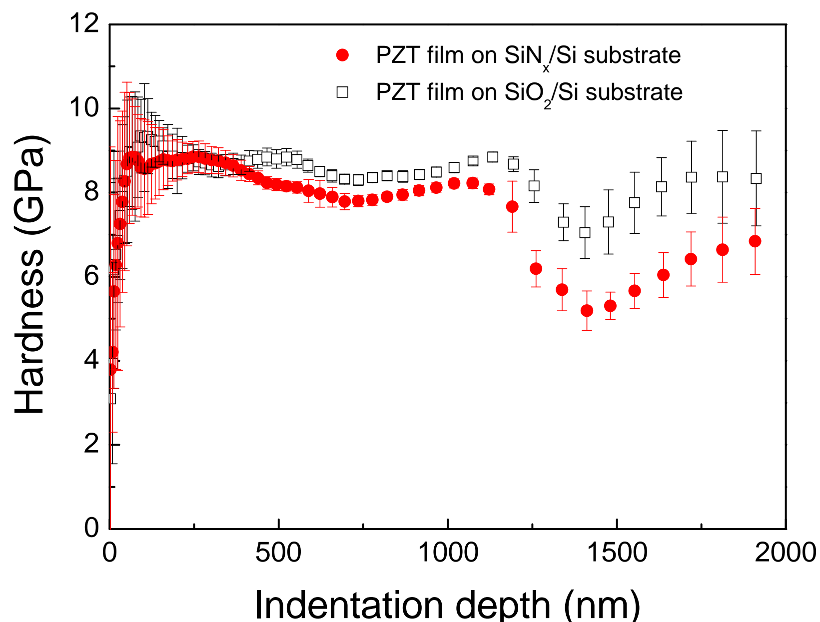

Figure 3-12 Hardness as a function of indentation depth with 2200nm depth limit for PZT on SiO_2/Si and SiNx/Si substrates

One may argue that the difference in the measured hardness could also be caused by the different substrate. For the measurement of elastic modulus of PZT film, the result will be greatly affected by the substrate even if the indentation depth is very small because the elastic deformation is not confined to the film itself; rather, it is a long-range effect that extends into the substrate [63]. However, for the measurement of hardness of PZT film, the plastic deformation will be confined within the film as the hardness of the substrates is larger than the one of thin film in both cases (Table 3.2) and the measured hardness should represent the true thin film hardness. This explains why the measured hardness of PZT films on two different substrates show almost identical value before delamination starts.

Table 3.2 Description of PZT film structure

Layer material	Thickness (μm)	Modulus(GPa)	Hardness(GPa)
PZT	0.580,0.830,1.130	125-190[17, 18, 50]	5.1-8.6[11, 17, 50]
Pt(111)	0.120	170[111]	9[11]
SiO_2	0.5	70[112]	14.4-18[113]
SiNx	0.5	220[114]	21.0[114]
Ta	0.010	178[115]	11.6[115]

3.5.2 Electrical properties of PZT films on different substrates

Table 3.3 The electric properties of PZT films with different thickness on two types of substrate

Thickness (nm)	Pr of PZT film with SiO_2-based substrate at 25V($\mu C/cm^2$)	Pr of PZT film with SiNx-based substrate at 25V($\mu C/cm^2$)	ε of PZT film with SiO_2-based substrate at 10K Hz	ε of PZT film with SiNx-based substrate at 10K Hz
580	19.55	19.89	1134.38	1171.62
830	21.58	22.46	1197.61	1169.81
1130	20.64	21.63	1213.24	1215.71

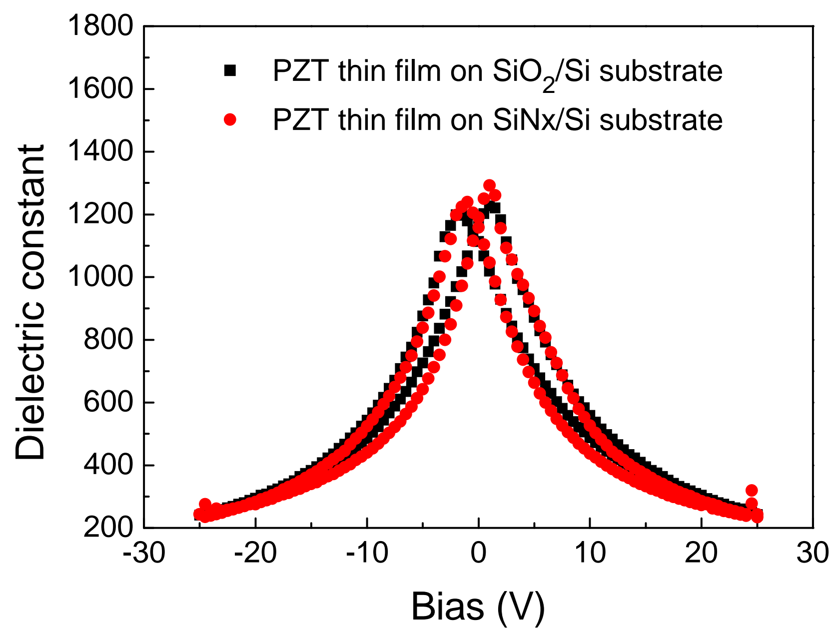

(a)

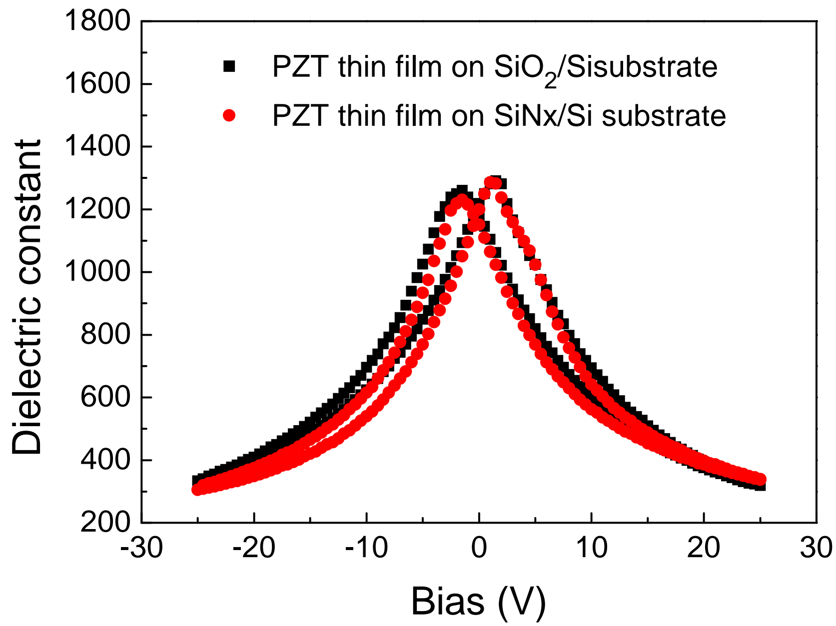

(b)

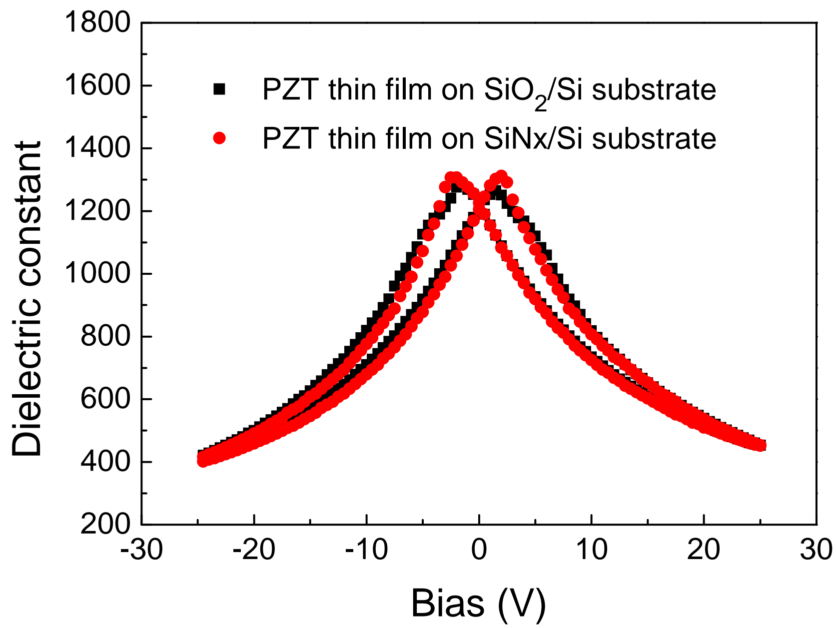

(c)

Figure 3-13 The dielectric constants of PZT films with different substrate as a function of DC bias (a) 580nm (6t) (b) 830nm (9t) (c) 1130nm (12t)

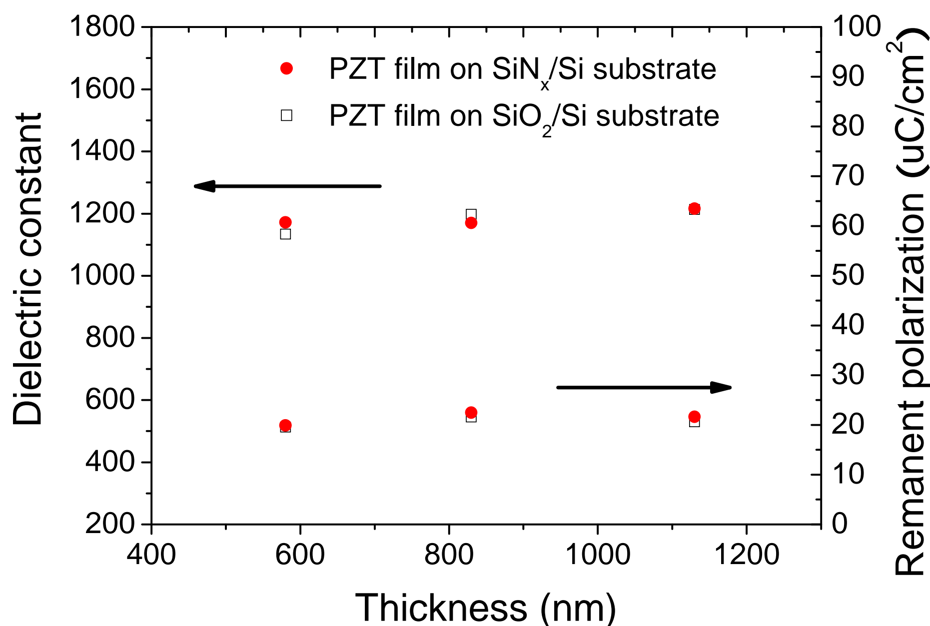

Figure 3-14 The electrical properties as a function of the thickness of PZT films on SiO_2/Si and SiNx/Si substrates

The remanent polarization and the dielectric constants of the PZT films were characterized as shown in Figure 3-13&14. All data were listed in Table 3.3. Both properties were not significantly influenced by the types of structural layer and the observed range of PZT film thickness. It is commonly reported that the remanent polarization and the dielectric constants increase as film thickness increases due to smaller residual stress and/or bigger grain size [116-118]. There exists a critical thickness where this scaling effect becomes negligible, typically in the range of 0.3-0.6µm, depending on the fabrication conditions. No significant change of the polarization and dielectric constant can be due to thicker films (0.58-1.13µm) that exceed the critical thickness. The PZT films on different structural layers also showed similar electrical properties. The results can be attributed to similar crystallographic properties such as orientation and microstructure and/or comparable residual stress conditions for the PZT

films grown on both structural layers as observed by the XRD and SEM results. Although the structural layer may affect the stress conditions [1], comparable residual stress values from PZT films on both structural layers were estimated that were due to the constraint of the PZT film by the much thicker Si substrate.

To confirm the conjecture, Raman scattering was conducted to investigate the residual stress condition in all PZT films. For PZT, the Raman spectra in the tetragonal phase have the following modes [119]:$A_1(TO_i)$,$A_1(LO_i)$, $E(TO_i)$,$E(LO_i)$ (i=1,2,3) and some mixed modes such as B1+E et al. To avoid the effect of Rayleigh scattering which is strong in the low-frequency region [120, 121], the $A_1(TO_3)$ mode was chosen for calculating the residual stress. From Lydane-Sach-Teller (LST) relation, the dielectric constant is proportional to the square of the phonon frequency of the $A_1(TO_3)$ mode, therefore, the following equation can be used to calculate the residual stress in PZT films [122, 123]:

$$\omega^2 = \omega_0^2 (1 - \frac{\sigma}{\sigma_1}) \qquad (3\text{-}2)$$

Where σ_1 is the stress under which the phonon frequency becomes zero and ω_0 is the phonon frequency under zero stress. By using the bulk-PZT sample, and fitting the obtained data, the σ_1=-640.7MPa and ω_0=528.8cm^{-1} for the $A_1(TO_3)$ mode was calculated [123].

The Raman spectra for PZT films were shown in Figure 3-15 and summarized in Table 3.4 after background correction and Lorentzian fitting. It's well known that the phonon frequency shift is related to residual stress, crystal size, temperature and crystal structure [120]. The last two factors can be excluded at first, because the Raman scattering was conducted at room temperature and the crystal structures were identical as

checked above. For the grain size, all samples show similar range and it's found the wave number shift of $A_1(TO_3)$ mode is less than 2 cm^{-1} for grain size larger than 17nm [123]. Therefore, the frequency shift in our case should be caused by residual stress. The obtained results show stress values of PZT films with different thickness are very close and in the range of 88 to 101 MPa. It should be noted that the 10 MPa difference of stresses of PZT film on different substrates will not result in significant change of electric properties since previously reported work [118] showed a 30MPa change in applied stress caused only a 2% change in electric properties.

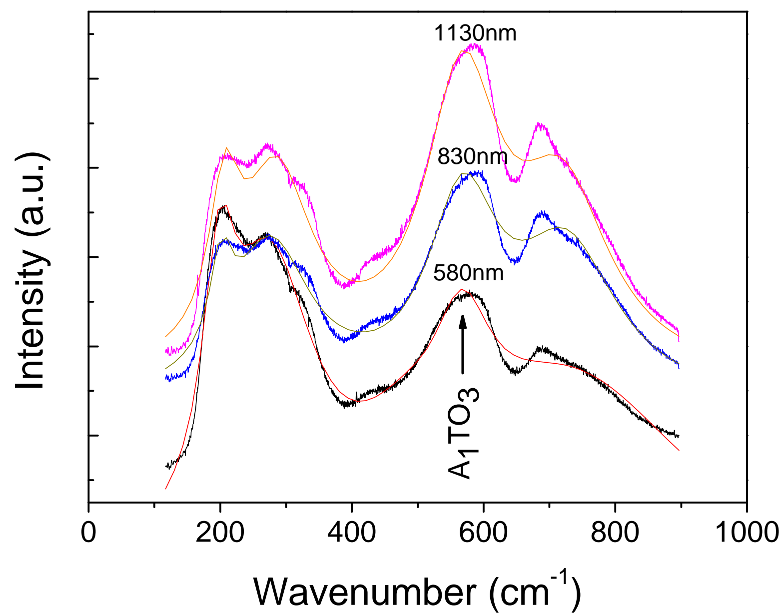

(a)

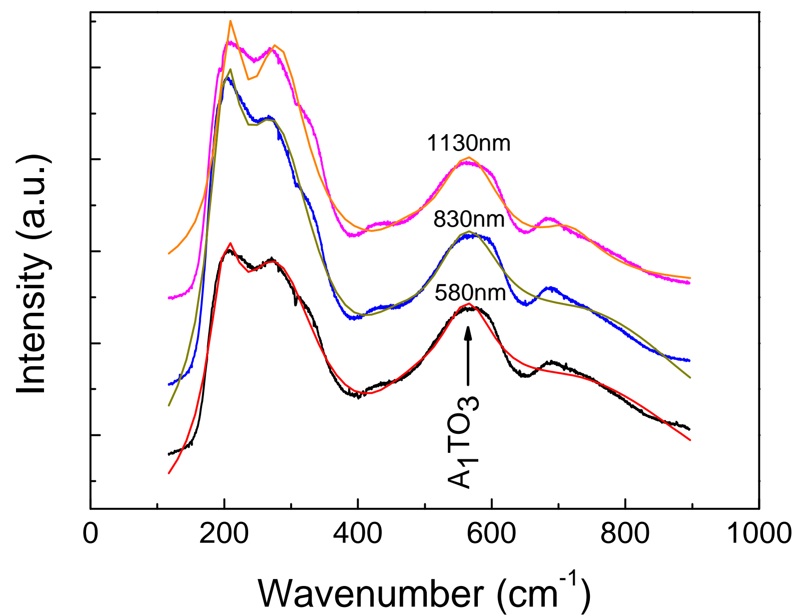

(b)

Figure 3-15 Raman spectra of PZT films on (a) SiO_2/Si and (b) SiNx/Si substrate

Table 3.4 The extracted residual stresses in the PZT films based on $A_1(TO_3)$ mode after background substraction and lorentz fitting

Thickness (nm)	PZT on SiO_2-based substrate		PZT on SiNx-based substrate	
	Freq.(cm^{-1})	Stress (MPa)	Freq.(cm^{-1})	Stress (MPa)
580 (6t)	568	98	564	88
830 (9t)	569	101	564	88
1130 (12t)	568	98	566	93

3.6 Chapter summary

Employing different structural layer materials (e.g. silicon dioxide or silicon nitride) will lead to different measured mechanical properties of PZT films. The measured Young's moduli of PZT films on SiNx-based substrates always shows higher value than those of PZT films on SiO_2-based substrate, which is attributed to the substrate effect throughout the whole indentation process. Since the measured values in both cases are affected by the substrate, it is necessary to develop a multilayer model in the future work to get the true modulus. The substrate effect on film hardness, however, was negligible since hardness value of around 8.8GPa was measured for both PZT on SiNx- and SiO_2-based substrates. Significant influences of the film thickness and substrate type on the electrical properties were not observed for the investigated thickness range of the PZT films due to the similar residual stresses conditions.

Chapter 4 Investigation of the Orientation Effect on the Mechanical Properties of PZT films on Different Substrate

4.1 Introduction

It is known that highly oriented crystalline thin films are required in the application of piezoelectric MEMS devices with desirable electromechanical properties. Thus, determination of the mechanical properties of oriented PZT film becomes crucial. However, only few studies focusing on mechanical properties [14, 17, 18, 50, 51, 124] were performed using the Si/SiO_2/Ti/Pt/PZT structure. For the multilayer structure, in order to measure 'film-only' mechanical properties, the most common method is to use one-tenth rule of thumb [60, 64] which suggests to limit the indentation depth within 10% of the film thickness so that the substrate effect could be ignored. This rule is not considered to be always applicable by some researchers [56, 63] , especially when the film is very thin. Since most above reported works did the measurement based on the one-tenth rule and with only one type of substrate, the orientation dependence of mechanical properties of thin films on different substrates remains unclear. In order to explore the possible substrate effect on the mechanical properties of oriented PZT films, it is necessary to employ a combined experimental and analytical method. In this letter, SiO_2 and SiNx-based substrates were used to fabricate PZT films since they are most

common layer material used in MEMS application and have distinct Young's modulus. A new model of thin film indentation based on discontinuous transfer of elastic strain [125, 126] is employed to assess properties.

4.2 Fabrication of oriented PZT films on different substrates

The sol-gel PZT solutions were prepared using 2-methoxyethanol (2-MOE) as the solvent. The major starting materials include lead acetate trihydrate (Aldrich, PbOAc, $Pb(CH_3CO_2)_2 \cdot 3H_2O$), titanium isopropoxide (Aldrich, TIP, $Ti[OCH(CH_3)_2]_4$), and zirconium propoxide (Aldrich, ZNP, $Zr(OCH(CH_3)_2)_4$), which are dissolved in 2–MOE solvents. Besides, acetylacetone (Aldrich, AcAc, $C_5H_8O_2$) was used as a chelating agent during the fabrication process. Therefore, precursors with acetylacetone and without acetylacetone were prepared, as shown in Figure 4-1 and 4-2.

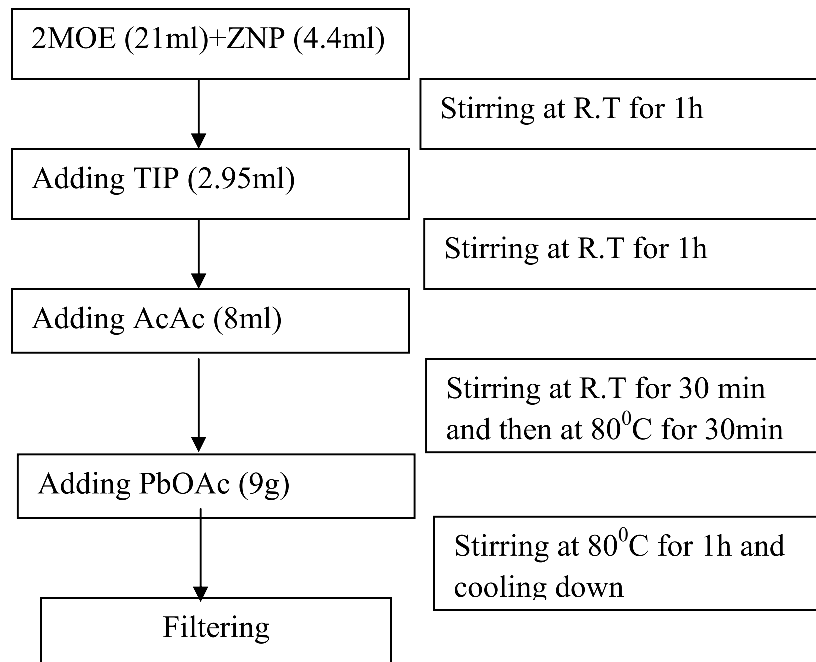

Figure 4-1 Flow chart for preparation of 0.5M PZT precursor with AcAc

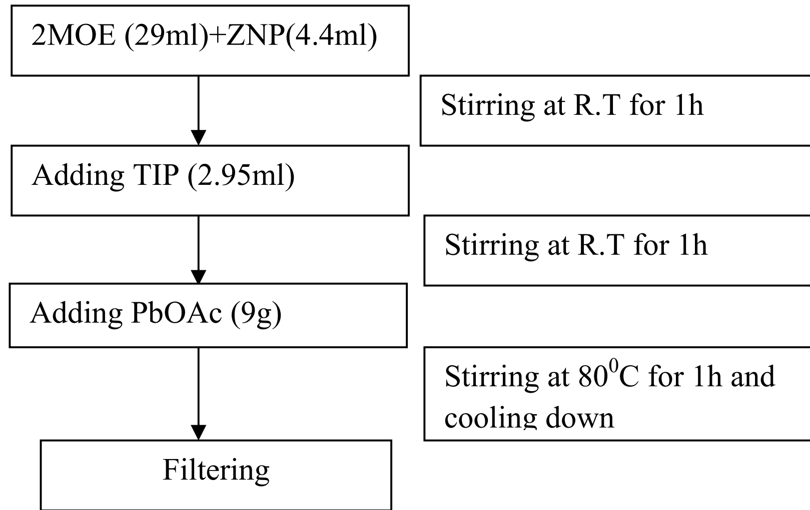

Figure 4-2 Flow chart for preparation of 0.5M PZT precursor without AcAc

The ratio of Zr to Ti is 0.52 to 0.48, which is the composition near the morphotropic phase boundary (MPB). 10 mol% excess lead sources were included in the precursor to compensate PbO volatilization during heat treatment. After filtering, the resultant solution was found clear and homogeneous after 3 days aging. The home-made and commercial solutions were then used to deposit the PZT films on two different kinds of substrates (Pt(120nm)/Ti(10nm)/X(500nm)/Si(500µm) (x=SiO_2 and SiNx)) according to the procedure shown in Figure 3-1. The final film thickness is about 1130nm through 12 deposition cycles. The varying pyrolysis temperatures at 250, 300, 350, and 500^{0}C were employed. The fabrication conditions and obtained results were listed in Table 4.1.

Table 4.1 Summary of the fabrication parameters and measured Young's Modulus

Sample #	Meas. flat region values (GPa)	Cal. values (GPa)		Orientation	Fabrication conditions*
SiO_2/Si	85±5	80±3			
SiNx/Si	290±35	312±29			
PZT /SiO_2/Si		1st	2st		
1	154±11	161±9	160±6	001	350C-WOAC
2	142±20	150 ±17	148±13	111	COMMERCIAL
3	133±15	139±12	136±9	110,111	250C-WOAC
PZT /SiNx/Si					
4	175±9	160±6	158±4	001	300C-WOAC
5	168±11	153±11	150±5	111	500C-WOAC
6	162±10	150±2	147±5	110,111	COMMERCIAL
PZT/Pt structure (Assumed)					
	133	130			
	150	148			
	170	171			
	175	176			

*350C-WOAC and 350C-WAC denote 350^0C pyrolysis temperature without AcAc and with AcAc, repectively

4.3 Results and discussion

Figure 4-3 shows the XRD patterns of PZT films on two substrates. Sample 1 and 4 have strong (001) orientations; samples 2 and 5 are mainly (111) orientated. Sample 3 and 6 have mixed orientations of (110) and (111) and the percentage of a certain orientation can be determined by the relative peak intensity according to the simple

formula:(hkl)%=$I_{(hkl)}/I_{total}$. The calculated percentage of (110) orientation of sample 3 is 59%, which is slightly larger than the 53% of sample 6.

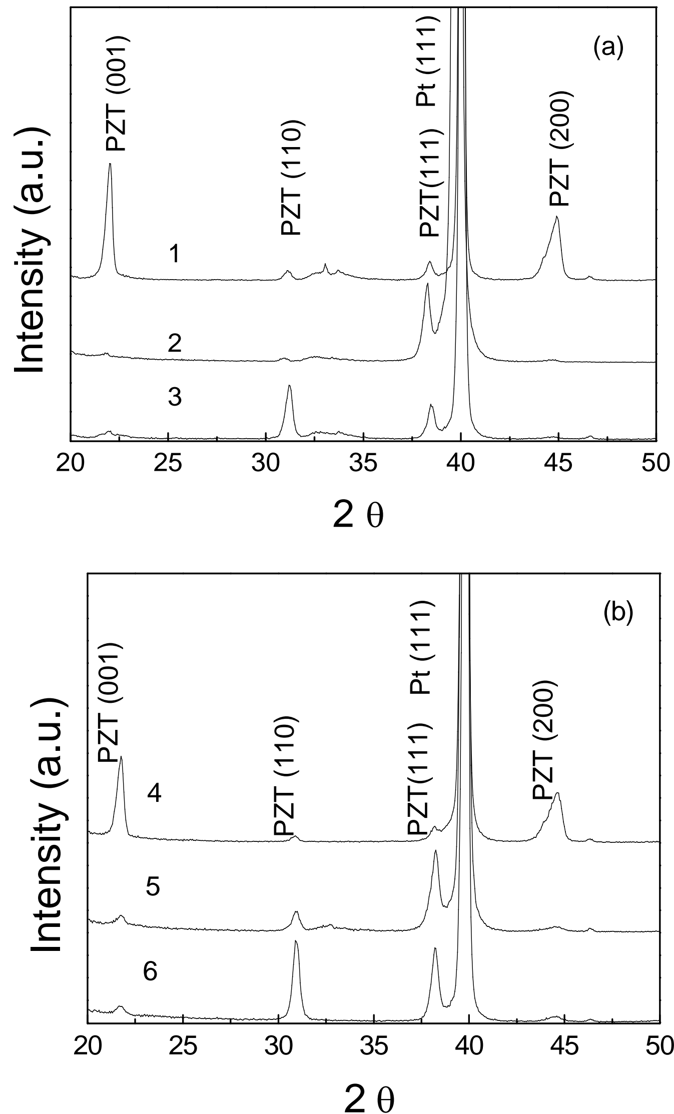

Figure 4-3 (a) XRD patterns of PZT films with SiO_2-based substrates. (b) XRD patterns of PZT films with SiNx-based substrates.

To characterize the mechanical properties of the PZT films, a nano-indenter (MTS Nano-indenter XP system) with a Berkovich type diamond tip and the continuous stiffness method (CSM) were employed. Since the Young's modulus of SiNx and SiO_2 in

the literature varies with the different fabrication conditions, the nanoindentation experiments were also performed on Si/SiO_2 and Si/SiNx two-layer composites. For each sample, 20 tests were performed with the same depth limit. The averaged data for each set of 20 indents is given in Figure 4-4 to Figure 4-7.

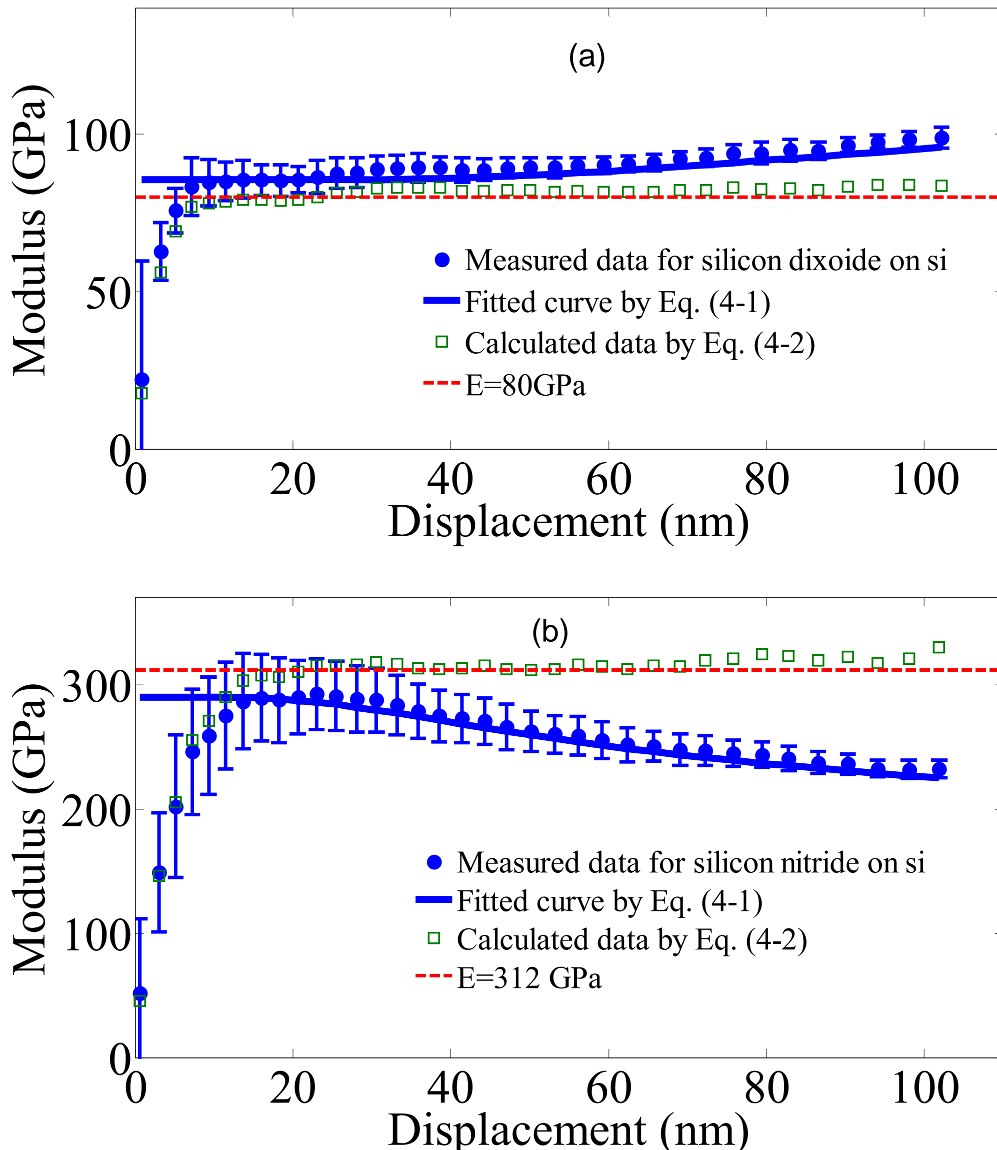

Figure 4-4 Plots of experimental and calculated data for (a) SiO_2/Si (b) SiNx/Si

Figure 4-4 shows the measured modulus-displacement curves of the SiO_2 and SiNx film on the Si (100) substrates. The data sets began with low values of modulus at small penetration depths that increased with penetration depth before leveling off at the so-called "flat" region and then slightly increasing or decreasing when the substrate was softer than the film. The low values of elastic modulus at the early stage of the intents indicated that the indenter tip lost contact with the film during the unloading stages of the continuous stiffness measurement, effects recently identified by Pharr et al.[127]. A recent model developed by Zhou et al [125, 126] was applied to the experimental data. This model, called the Discontinuous Elastic Interface Transfer Model, accounts for discontinuity in elastic strain transfer at the film/substrate interface resulting from different moduli and Poisson's ratios of the two components. It has the following form:

$$\frac{1}{E'} = \frac{1}{E'_{flat}}(1-\Phi_s) + \frac{1}{E'_s}\Phi_f \tag{4-1}$$

where E' is the composite modulus, E'_{flat} is the measured flat region value, $E'_s = E_s/(1-\upsilon_s^2)$, is the substrate modulus and $\Phi_f = e^{-\alpha_f(t/h)}$ and $\Phi_s = e^{-\alpha_s(t/h)}$ are the weighting factors to account for the effects of the film on the substrate and substrate on the film, respectively. t is the film thickness, h is the indentation depth and α_f and α_s are the constants for the film and substrate respectively, corresponding to their bulk Poisson's ratios. Here, The Poisson's ratio is 0.28 [114] for SiNx , 0.17 [112] for SiO_2 and 0.28 [128] for Si; the modulus of Si is 173 [128]. The solid lines in Figure 4-4 represent the Discontinuous Elastic Interface Transfer model for the film/substrate combinations in this work. They show an excellent fit to all data sets with the exception of low penetration depths where contact was lost. All data sets exhibited a "flat" region,

which has been considered by some to indicate the film modulus. However, recent work by Zhou et al. [126] has indicated this value is substrate dependent and represents the film/substrate composite modulus. Therefore, to extract the true film modulus from the experimental data, they proposed a power function to relate the film and substrate modulus to the measured flat region value, the Equation (4-1) was then re-written as

$$\frac{1}{E'} = \frac{1}{E_f'}(1-\Phi_s)\bullet\left(\frac{E_f'}{E_s'}\right)^{0.1} + \frac{1}{E_s'}\Phi_f \tag{4-2}$$

where $E_f' = E_f / (1-\nu_f^2)$ is the film modulus. The additional term $\left(\frac{E_f'}{E_s'}\right)^{0.1}$ accounts for the early influence of the substrate. In applying this equation, the film modulus of SiO_2 and SiNx can be calculated based on the measured flat region values (Table 4.1). The calculated values from each data points are relatively uniform with displacement into the surface in both cases.

The modulus-displacement curves of all PZT films were presented in Figure 4-5 to Figure 4-7. The flat region values were summarized in Table 4.1. For the PZT film on SiO_2-based substrate, it was observed that PZT film with significant (001) orientation has a flat region value of 154GPa and the sample with strong (111) orientation has a smaller value of 142GPa, while the one with mixed orientation of (110) and (111) has the smallest value of 133GPa. The tendency is in agreement with the reports by Delobelle et al. [14, 17, 50] and Wang et al. [18]. As far as PZT films on SiNx-based substrate, the same inequality regarding orientation effect is observed: $E_{<001>} > E_{<111>} > E_{<110,111>}$. However, even with similar orientation, the measured values appear much larger than those of PZT films on SiO_2-based substrate. It is known the elastic modulus depends on

the nature of atomic bonding instead of the microstructure of the materials, although some researchers [129] reported the size dependence of Young's modulus of the pure metal, which was found to be due to the porosity of the material. And Delobelle [17] pointed out the Young's modulus of oriented PZT films is independent on grain size, especially when the applied load in nanoindentation is low [124]. In our experiments, the applied maximum load in the flat region is about 2mN, which can be considered as a low pressure condition. Therefore the significant difference of measured moduli between PZT films on two different kinds of substrates should be attributed to the varying structural layer; otherwise we could get very close moduli.

The multi-layer composite could be assumed as PZT/X/Si three-layer structure in the calculation (X=SiO_2,SiNx), since the Ti layer was very thin and the Pt layer possessed a modulus 170GPa [111], close to that of PZT, it was not considered to be a component of the film (this will be demonstrated later). To apply this model to the PZT film structure, we firstly assume a composite film (PZT/SiO_2 or PZT/SiNx) on the Si substrate. Here, the Poisson's ratio is 0.3 [130] for PZT film. The fitted curves by using Equation (4-1) were shown in Figure 4-5(a) to Figure 4-7(a), matching the experimental data very well. The calculated PZT film values for the PZT/SiO_2 (open symbols) and PZT/SiNx (solid symbols) structures by using Equation (4-2) were presented in Figure 4-5(b) to Figure 4-7(b), which are still under the influenced of the Si substrate although it is not expected to be significant due to the close modulus of Si to that of the PZT (for the same reason with Pt).

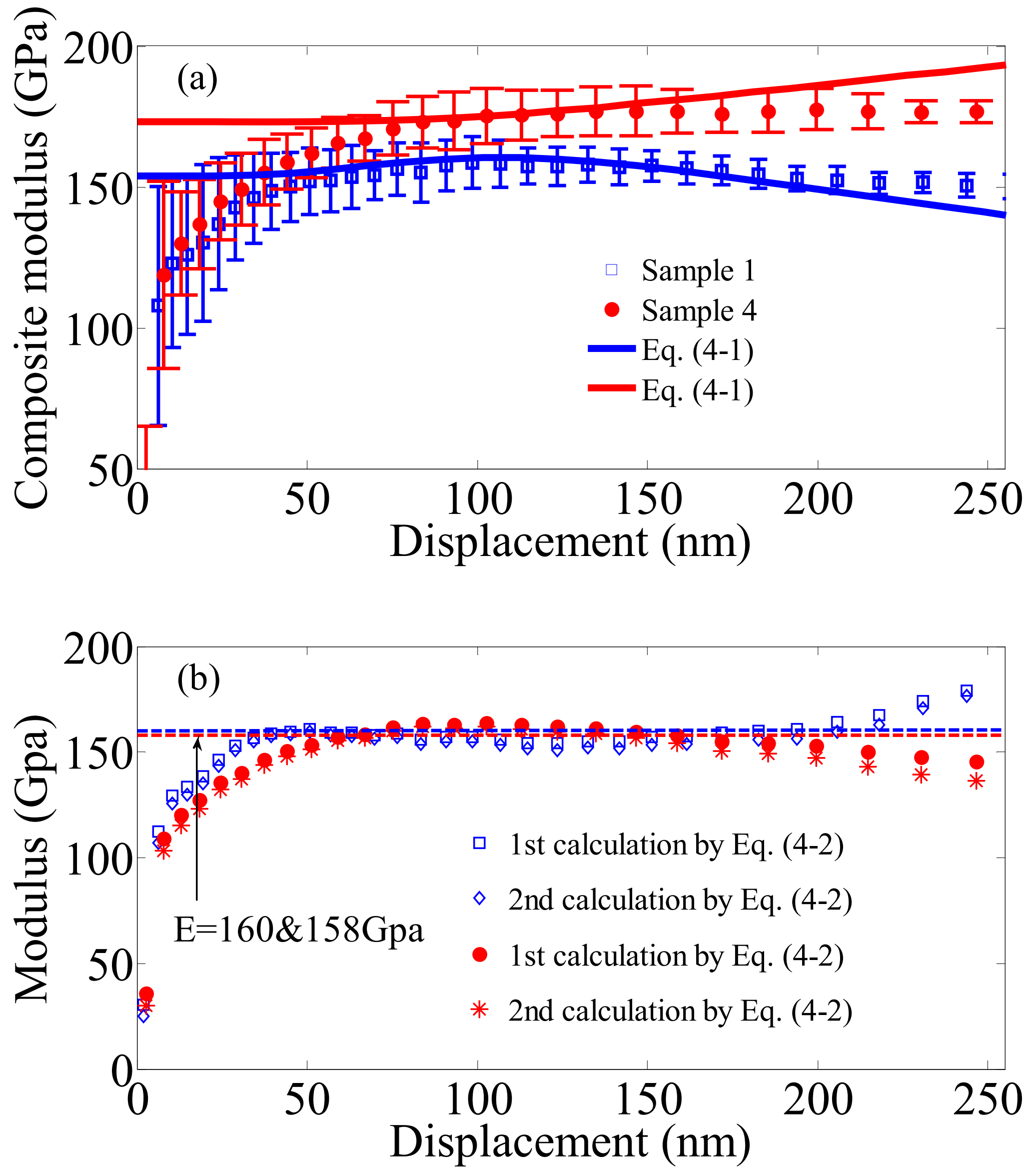

Figure 4-5 (a) Experimental and (b) calculated data of PZT films with (001) orientation on SiO_2/Si and SiNx/Si substrates

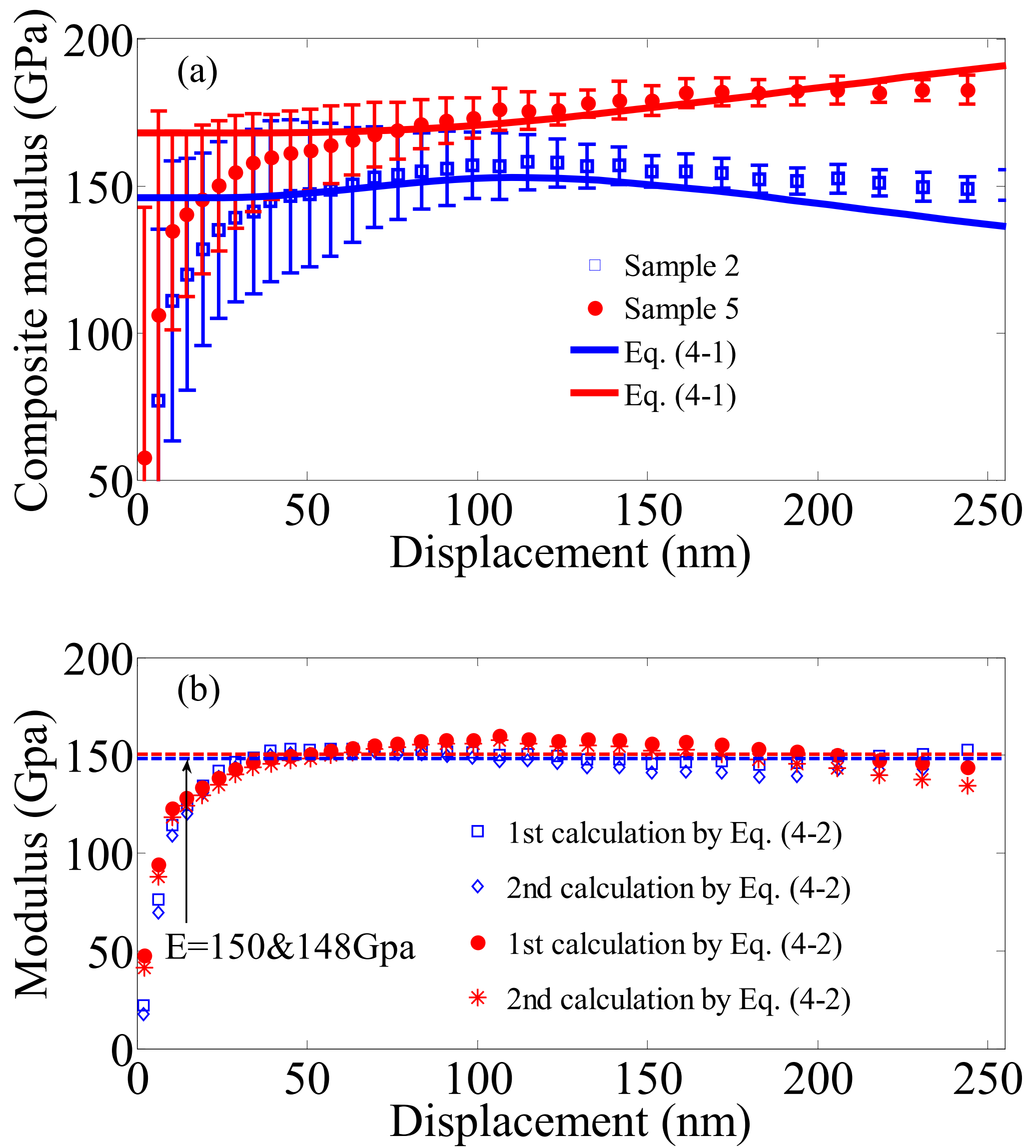

Figure 4-6 (a) Experimental and (b) calculated data of PZT films with (111) orientation on SiO_2/Si and SiNx/Si substrates

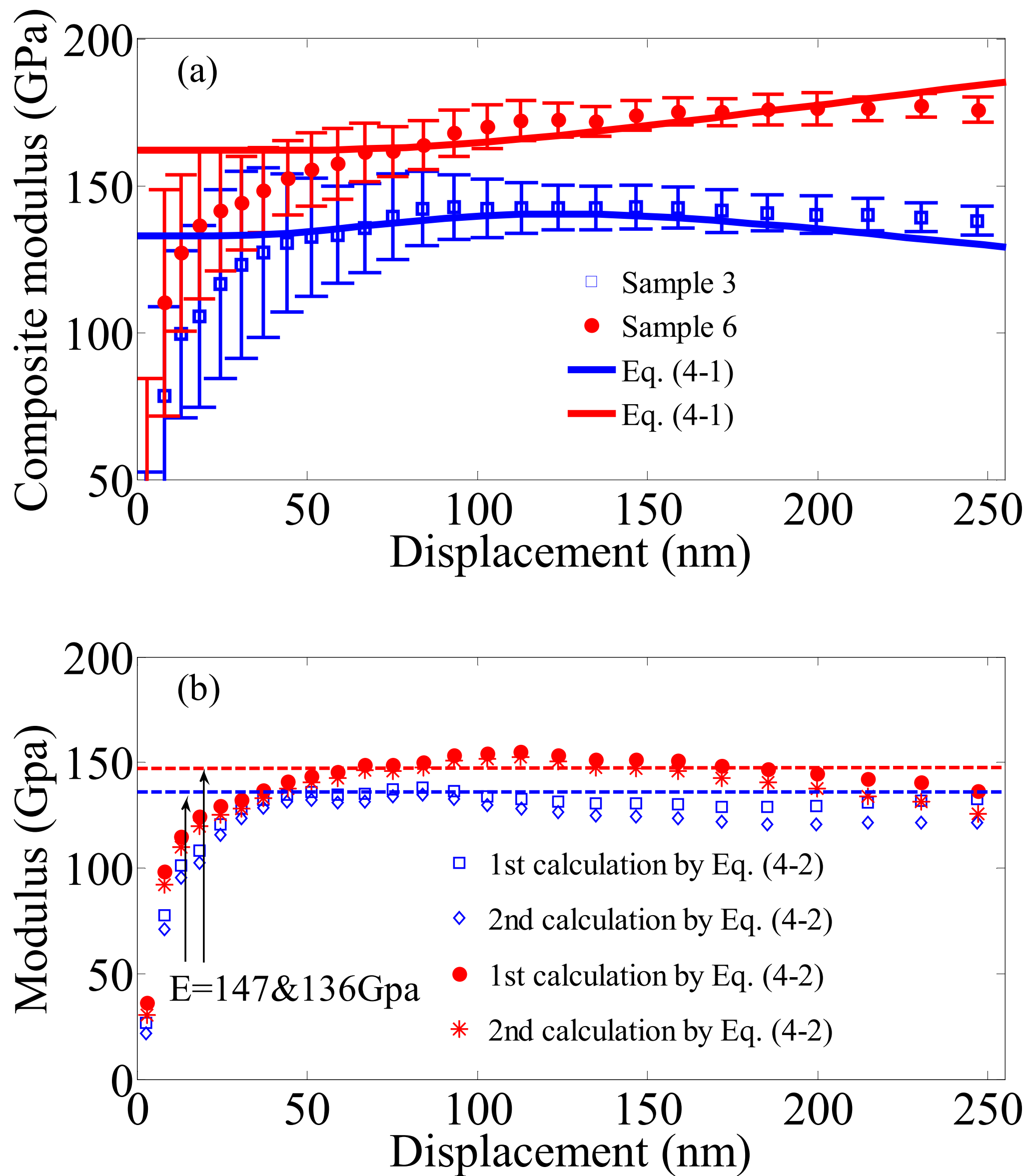

Figure 4-7 (a) Experimental and (b) calculated data of PZT films with mixed orientation on SiO_2/Si and SiNx/Si substrates

Equation (4-2) was applied again in the composite film/Si structure to get true PZT film modulus. Here, the values of *E*' are the previously calculated results by Equation (4-2) and the film thickness is the combined thickness value of PZT and SiO_2 or

SiNx films. The calculated values were presented in Figure 4-5(b) to Figure 4-7(b). Data for PZT film on SiO_2 and SiNx-based substrate are represented by diamonds and stars, respectively, and relatively uniform with displacement into the surface in defined range. Calculated flat region values through Equation (4-2) were all listed in Table 4.1. In the case of PZT films on SiO_2-based substrates, the second calculated values are larger than the measured flat region values, which clearly indicates the moduli of the PZT films are underestimated due to the softer SiO_2 structural layer. While for the PZT films on SiNx-based substrates, the overestimated film modulus was observed due to the harder SiNx structural layer. However, in both cases, the previously obtained inequality: $E_{<001>} > E_{<111>} > E_{<110,111>}$ remain unchanged. It should be noted that obtained true values of two PZT films with similar orientation on different substrate are supposed to be the same. Among the samples listed in Table 4.1, PZT films with significant (001) and (111) orientation appear to agree well with less than two percent difference between their average values for two substrates. For PZT films with mixed orientation of (110) and (111), it was observed the modified modulus of PZT film on SiNx-based substrate is still larger than the one of PZT film on SiO_2-based substrate. This result could be attributed that the (111) orientation account for a large portion of the measured modulus since we randomly choose the indentation positions.

Based on Equation (4-2), we then go back to check the influence of the Pt layer on the measurement. Since we know the following inequality $E_{SiO2} < E_{Pt} < E_{SiNx}$, the measured flat region values should be in the range of 133GPa to 175GPa for a PZT/Pt two-layer structure. 133 and 175GPa correspond to the smallest one of measured flat region values in the case of PZT film on SiO_2-based substrate and the largest one of

measured flat region values in the case of PZT film on SiNx-based substrate, respectively. Using several values in the range of 133 to 175, we could get the corresponding fitted values by using Equation (4-2) and the calculated results are listed in Table 4.1. It was observed that the fitted values are very close to the assumed flat region values, which indicates the substrate effect for the PZT/Pt structure is not so significant and the Pt layer can be ignored as we apply the developed model to the PZT film structure.

4.4 Chapter summary

The orientation effect on Young's modulus of PZT film with different structural layers was investigated. The result shows the measured values will vary with different substrates but the obtained relationship (E_{001}>E_{111}>$E_{(110,111)}$) between measured modulus of PZT films with different orientation will remain the same. By using the model developed by Zhou et al, we could extract true orientation effect from the experimental data and get good consistency between highly oriented PZT films on different substrates.

Chapter 5 Investigation of the Influence of Varying Si Substrate Thickness on the Electrical and Piezoelectric Properties of the PZT Cantilevers

5.1 Device design and fabrication

5.1.1 Device design

5.1.1.1 Cantilever dimension

Cantilevers with three kinds of dimensions were designed, as shown in Figure 5-1. The dotted area is the top electrode, whose size was reduced compared to the PZT layer to prevent possible electric shortage between the top and bottom Pt electrode after fabrication. All cantilevers are 2mm wide and the length for a type cantilever is 8mm, 6mm for b type cantilever and 4mm for c type cantilever.

There are two ways to fabricate to get PZT cantilevers with different Si thicknesses. One method involves setting cantilever thickness for one piece of wafer, so every cantilever from the piece of wafer has the same Si substrate thickness. This method requires multiple pieces of wafer to fabricate PZT cantilevers with varying Si thickness. The other method involves performing back-side etching on one piece of wafer, so the PZT cantilevers in one specific region will have the same Si substrate thickness, as shown in Figure 5-2. The former method will have a slightly easier fabrication process,

but will significantly increase the fabrication period, since each fabrication of PZT cantilevers with a certain Si substrate thickness will repeat the processes before back-side etching. Knowing this, the second method was employed in this study. The fabrication process will be discussed in detail later. The corresponding thicknesses in Figure 5-2 are 250, 125, and 65μm, respectively.

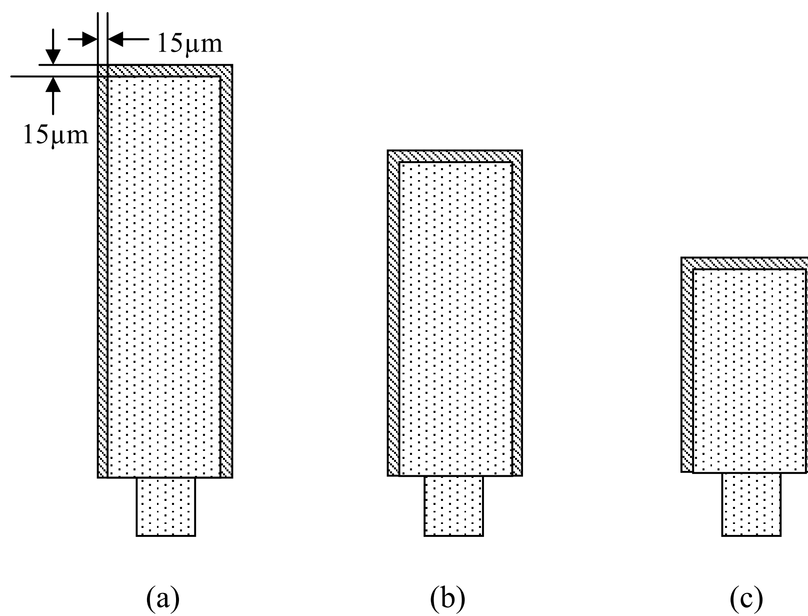

Figure 5-1 Schematic of the designed cantilevers

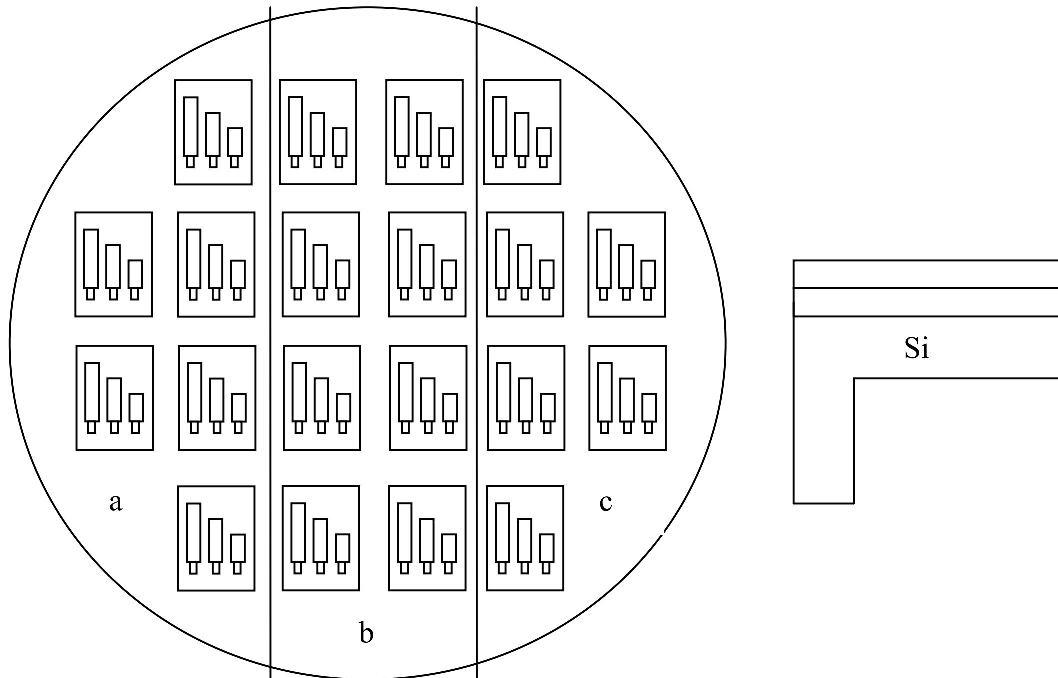

Figure 5-2 Schematic of the designed cantilevers on the wafer with different Si thickness

5.1.1.2 Layer structure design

A 500 nm thick SiO2 was grown on a 4 inch silicon wafer by thermal oxidation, which is the layer structure in PZT cantilevers. Due to its high electrical conductivity and thermal stability at high temperatures, 120nm Pt was then deposited by sputtering on the Si-based substrate as a bottom electrode. Prior to the deposition of Pt as a bottom electrode, a very thin Ti layer was sputtered on the substrate to improve the adhesion between Pt and SiO_2. For the PZT cantilever application, the PZT film has to have been grown on an electrode. Therefore, ~1µm PZT film was deposited subsequently on the Pt bottom electrode by sol-gel, as introduced before. Finally, 120nm Pt was deposited again

as a top electrode. The schematic of the PZT multi-layer configuration before PZT cantilever fabrication was shown in Figure 5-3.

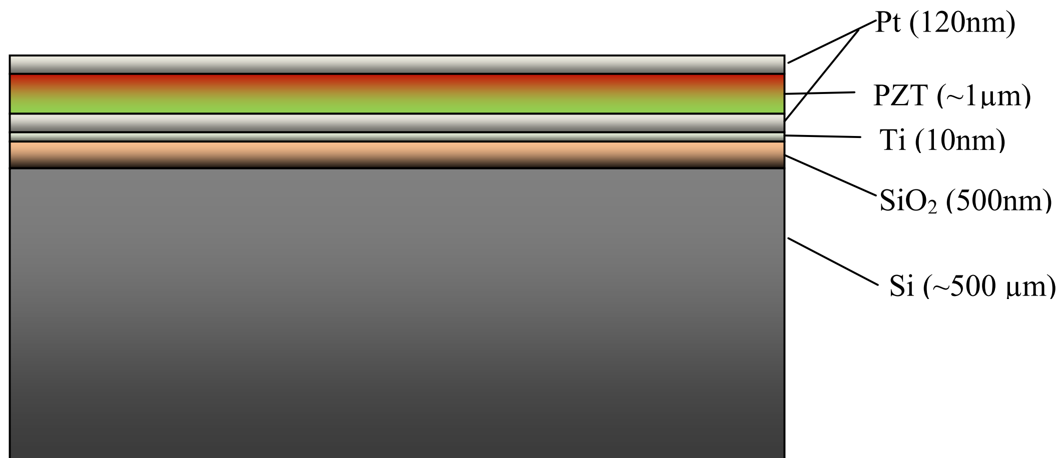

Figure 5-3 Schematic of the multi-layer configuration for the PZT cantilever

5.1.1.3 Mask design

Fabrication of PZT cantilevers is an established process requiring 4 masks to complete, as shown in Figure 2-11. The first mask (Figure 5-4) was designed for electrode patterning. Four different sizes (0.01, 0.04, 0.09, 0.25 mm^2) of square electrodes were also patterned for measuring the piezoelectric and dielectric properties of the PZT film before microfabrication of PZT cantilevers. The second mask (Figure 5-5) was designed to define the cantilever structure and bottom electrode. The third mask (Figure 5-6) was designed to obtain cantilever structures with different Si thickness

without damaging bottom electrode. The pattern of back-side etching was defined by the fourth mask (Figure 5-7) and the cantilever structure was finally released by Si RIE.

Figure 5-4 Mask for top electrode patterning

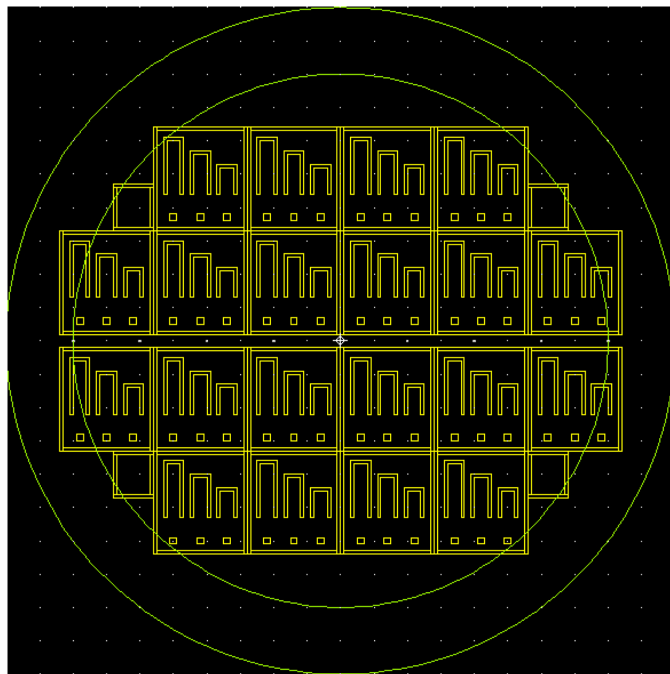

Figure 5-5 Mask for 1st cantilever patterning

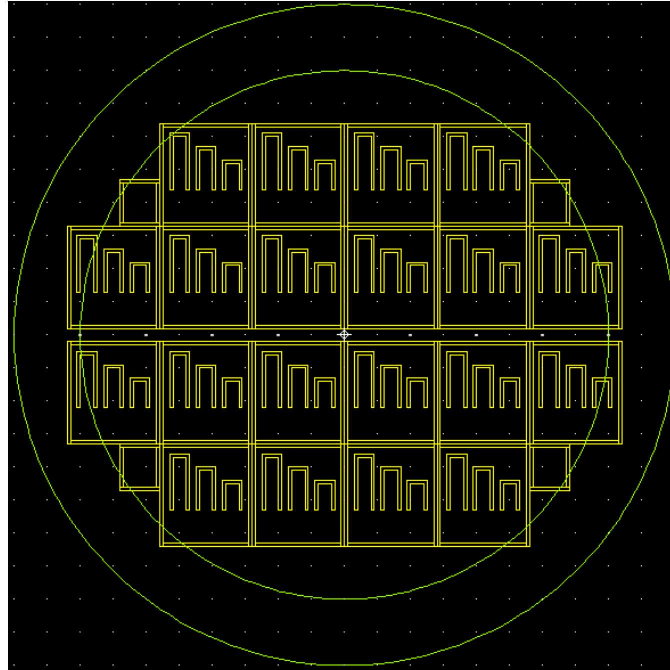

Figure 5-6 Mask for 2st cantilever patterning

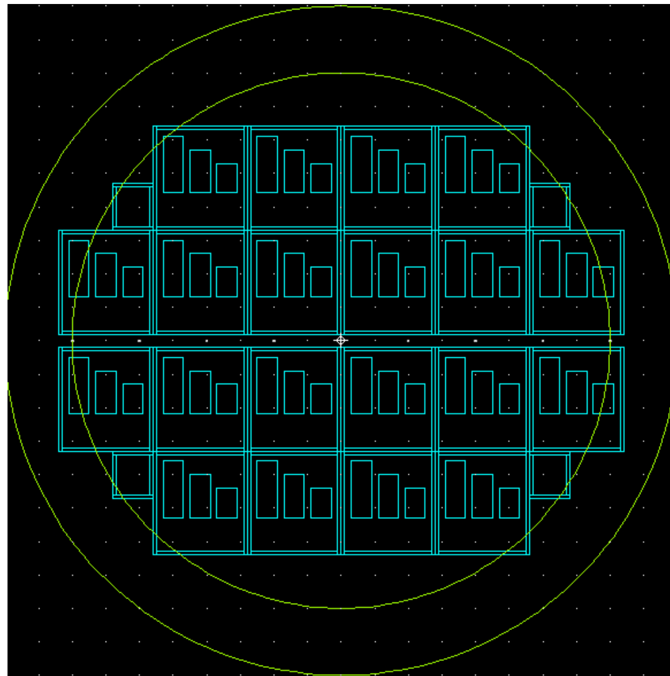

Figure 5-7 Mask for back-side etching

5.1.2 Device fabrication

The PZT cantilever fabrication process is based on several iterations of photolithography and etching, as shown in Figure 2-11. The details of the PZT cantilever fabrication process are described in the following chapters and outlined in Appendix B.

5.1.2.1 Photolithography

The first step in the fabrication of PZT cantilever is to define the top electrode pattern. This process started with a PZT film stack on a 4 inch wafer, as described in Figure 5-3. Before patterning the top electrode, the wafer was put in a microprocessor for 20 minutes at 120^0C to remove moisture 20min. Any moisture on the wafer surface would interfere with the photolithography process, causing it to yield poor results. Unfortunately, the surfaces of many of the materials for depositing resist oxidize very easily. Bonding with water adsorbed from the air, the surface oxide will form long range hydrogen. When the resist is spun onto such a surface, it adheres to the water vapor instead of the surface and poor adhesion results. Hexamethyldisilazane (HMDS) is a common primer used before spin coating that serves as an adhesion promoter for photoresist. Therefore, HMDS was applied to increase the adhesion between photoresist and the PZT film after the dehydration of the wafer.

~2 µm Negative photoresist (nLOF 2035) was then spin coated on the 4 inch wafer and exposed to a pattern of intense light using a mask aligner. After developing with an AZ 300 MIF developer solution, the photoresist pattern was inspected under the

microscope to make sure the undesired resist was completely removed. Next, the top electrode was obtained by lift-off process after Pt deposition on the layer of patterned photo resist (PR).

In the next step, the second mask was employed to do the first cantilever patterning and bottom electrode access. At the experiment's outset, photoresist AZ5214E was chosen for pattern transfer. A spin speed of 500 rpm makes a thickness of ~5 μm. For cantilever patterning and bottom electrode access, a total thickness of ~15 μm will be necessary for etching the front side without damaging the Pt top electrode [131]; this requires three depositions of AZ5214. Unfortunately, the multi-cycle procedure was found to be inappropriate for the following reasons:

1) Repeated bake and deposition of PR will generate a lot of nitrogen gas, causing many bubbles formed in PR.
2) The defects formed in the first layer will influence the quality of the following layers.
3) The first and second layers are over-baked in the repeated process.
4) It is hard to precisely control developing time.

As a result, the AZ 5214E was replaced by AZ P4620, which can generate a much thicker layer, from 5 μm to 20 μm, depending on the spin speed. The process parameters for two photoresist are listed in Table 5.1. In this study, a spin speed of 1000 rpm gave ~15 μm thick photoresist by a single deposition. After deposition, the multi-exposure and developing processes were performed to get the desired pattern.

For the second cantilever patterning and back-side etching, the same resist process described above was used.

Table 5.1 Comparison of process conditions of two photoresists for cantilever patterning

Resist	Thickness per layer (μm)	Spin speed (rpm/acc/time)	Prebake (ºC/min)	Exposure time (sec)	Developing (min/developer)
AZ 5214E	~5	500/500/50	105/1	12	1 / AZ400K(1:3)
AZ P4620	~15	1000/250/30	110/1.5	25x3, Interval-60	3.5-4/ AZ400K(1:2.5)

5.1.2.2 Etching

Etching is to selectively remove deposited films or parts of substrates to make desired patterns and/or shapes. This process involves the removal of a solid surface of a material by physical and/or chemical means. Wet chemical etching and dry etching (sputtering, ion beam milling, reactive ion etching, plasma etching, etc.) are used in fabrication processes to make the desired MEMS.

Wet etching is the process of removing material by immersing the wafer in a liquid bath of the chemical etchant. It can be categorized as either isotropic etching or anisotropic etching. Isotropic etching has a uniform etch rate at all crystal orientations. For isotropic etching of silicon, the most commonly used etchants are mixtures of hydrofluoric (HF) and nitric (HNO_3) acids in water or acetic acid (CH_3COOH) [132]. The reaction between Si and the etchant system (HNA) is

$$Si + HNO_3 + 6HF \rightarrow H_2SiF_6 + H_2NO_2 + H_2O + H_2$$

Ethylene-diamine-pyrocatecol (EDP), potassium hydroxide (KOH) and hydrazine are usually used as anisotropic etchants of silicon, etching silicon along different crystal orientations with different etch rates.

Dry etching is based on plasmas, fully or partially ionized gas molecules and neutral atoms/molecules sustained by the applied electromagnetic field. Plasma etching processes involve highly reactive particles in a relatively cold medium. The gas and flow rate, excitation power, frequency, reactor configuration and pumping determine the electron density and distribution, gas density and residence time defining the reactivity. These parameters, along with wafer parameters, define the surface interaction and etching characteristics.

In this study, dry etching was chosen over wet etching, due to dry etching's excellent shaping ability, such as good control of etch rate, directionality of etching, high resolution and less undercutting. There were two types of ICP etch source used in fabrication of PZT cantilevers: Advanced Oxide Etcher (AOE) for PZT, metal and oxide layer etching and Advanced Silicon Etcher (ASE) for Si etching.

For the application of AOE, various gases and their mixtures are widely used. The most favorable gases are CHF_3, CF_4 and SF_6 combined with Ar or C_2F_6. In order to achieve a high oxide etch rate, good selectivity to the utilized mask material and an improved ability to etch substantially narrower features to ever greater depths without excessive RIE lag, various combinations of process parameters such as coil and platen power, pressure, gas flow and bias were tested in the experiments [131]. The optimized parameters and detailed recipe for AOE were listed in Park's dissertation [131], and

found to be able to provide a moderate etching rate without damaging the PZT films or over-etching the photoresist mask.

Similar experiments were performed for obtaining optimized ASE parameters [131]. Different from AOE, larger etching depth is required in silicon etching, therefore two modes are alternately repeated to achieve nearly vertical structures:

1) A nearly isotropic plasma etching. The plasma contains some ions, which attack the wafer from a nearly vertical direction. (For silicon, this often uses sulfur hexafluoride [SF_6])

2) Deposition of a chemically inert passivation layer. (C_4F_8 source gas yields a substance similar to Teflon.)

In this study, the etching process was performed first and lasted for 13 seconds, using SF_6 and O_2. Then the passivation process continued for 7 seconds with C_4F_8 as etching gas. The passivation layer protects all surfaces from further chemical attack and prevents further etching. However, during the etching phase, the directional ions will attack the passivation layer at the bottom of the trench, but not along the sides. Therefore, the repeated etching/deposition steps will result in a smooth and vertical wall.

Since we want to achieve a different Si substrate thickness in three different regions on one wafer, the photoresist will be deposited onto an etched area as a protective mask to prevent further etching before the etching process continues. The schematic front-side etching process was shown in Figure 5-8.

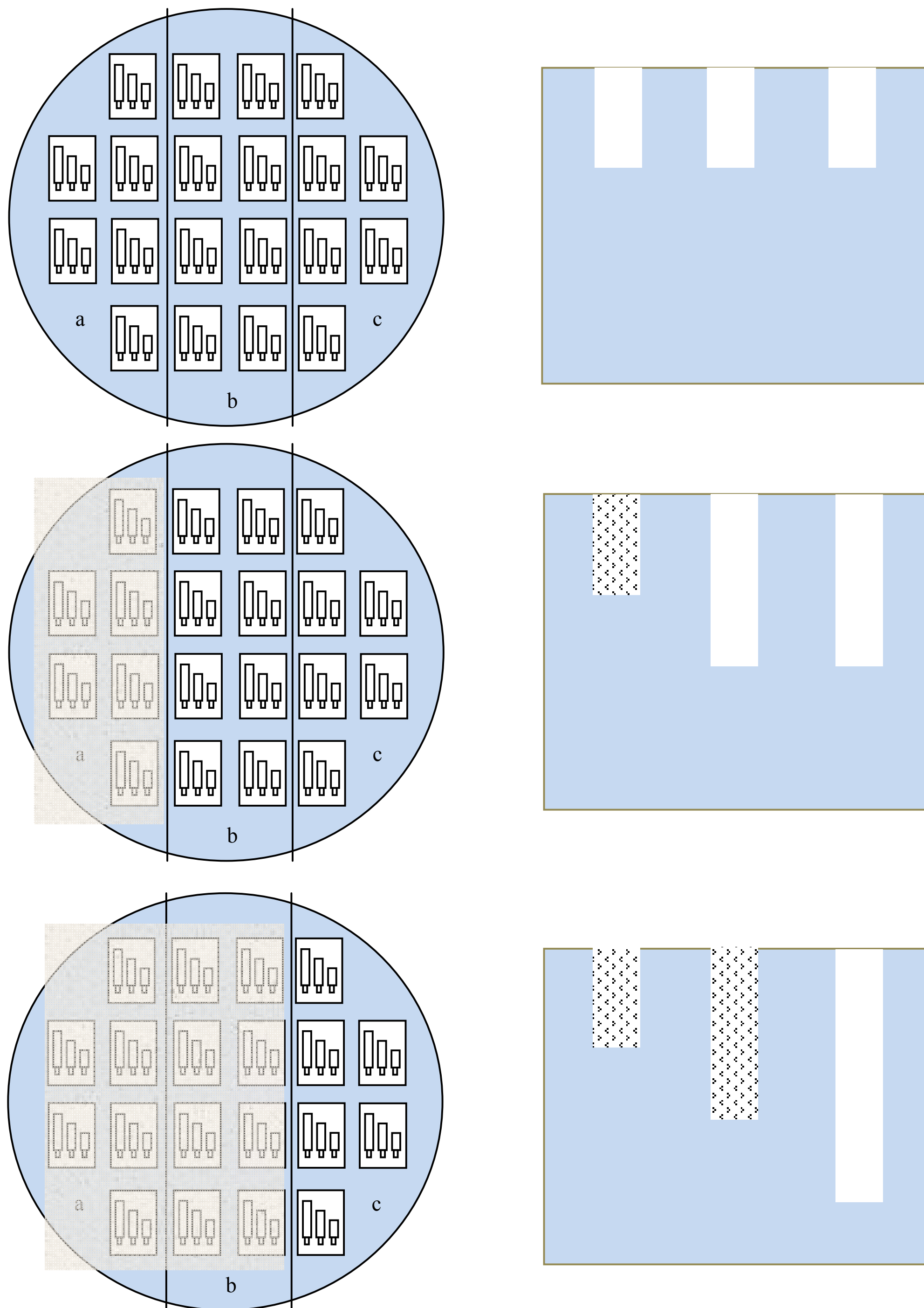

Figure 5-8 Schematic of the front-side etching for the PZT cantilevers

5.2 Experimental setup and measurement of electric properties of PZT cantilevers with different Si thickness

The thickness of the Si substrate of the PZT cantilevers was measured by SEM (JEOL 7000 FE). The polarization hysteresis loops and dielectric properties were characterized by the TF-2000 analyzer and 4192A impedance analyzer as described in Chapter 3.4. The major instrumentation in the experimental setup for the measurement of piezoelectric coefficients and tip-deflections of the cantilevers, shown in Figure 5-9, includes a Keithley 617 programmable electrometer, a MTI2000 Fotonic Sensor (MTI Instruments, Albany, NY) and an oscilloscope (Tektronix, TDS3014B). The applied voltage was provided by the electrometer, changing from -30V to +30V. In order to reduce errors caused by ambient noise and unstable readings etc, the voltage was increased by 2V every time, which can generate relatively large deflection. The tip-deflection of the cantilever was recorded by the Fotonic Sensor. By connecting the Fotonic Sensor to the oscilloscope, the voltage output of the Fotonic Sensor, corresponding to the tip-deflection of the cantilever, can be monitored when we apply the sine-wave signal to the cantilever. Finally, the effective transverse piezoelectric coefficient can be calculated from Equations (5-14) & (5-15), which are related to the tip-deflection, dimension and mechanical properties of samples.

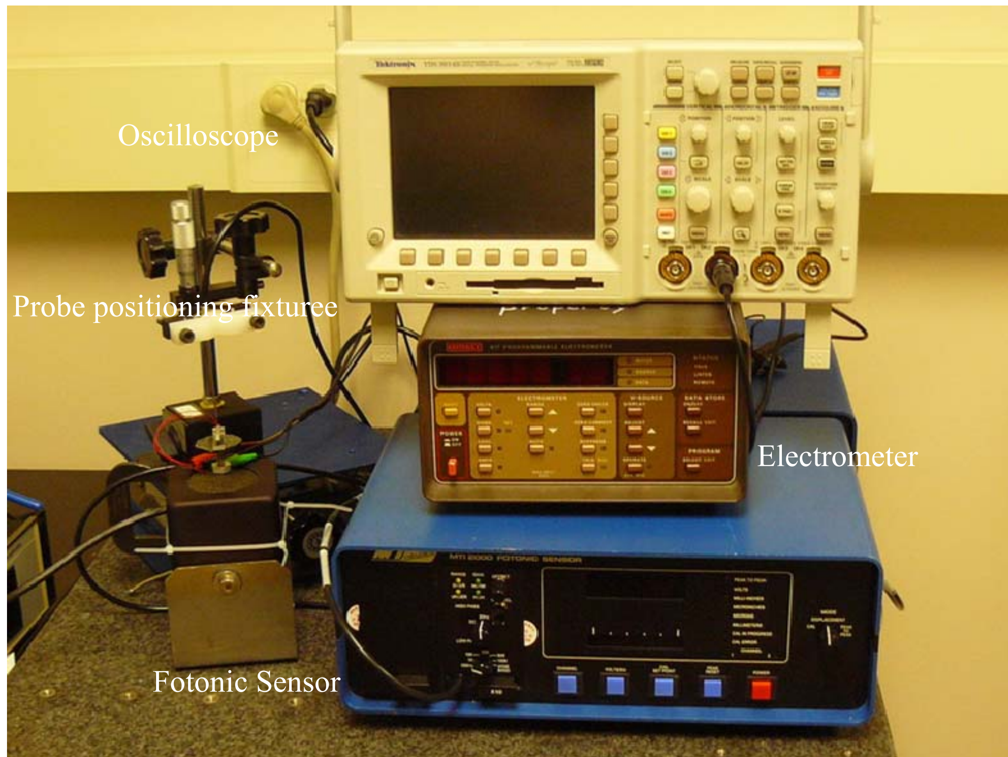

Figure 5-9 Setup for measurement of piezoelectric coefficients of the cantilevers

The Fotonic Sensor (FS) is a dual-channel, fiber-optic system which can perform noncontact displacement and vibration measurements [133]. It will not impose load on the measuring surface with fiber-optic technology. This is very useful for the measurement of displacement in the case of a PZT cantilever, where special attention is required to avoid the damage of the very thin Pt electrode layer and the cantilever itself. FS is based on the principle of intensity modulation of reflected light. The light is passed through one fiber and it is made to incident on the surface of the object. The light reflected from the surface is captured by the other fiber. The intensity of detected light depends on the distance between the object surface and probe tip (Figure 5-10).

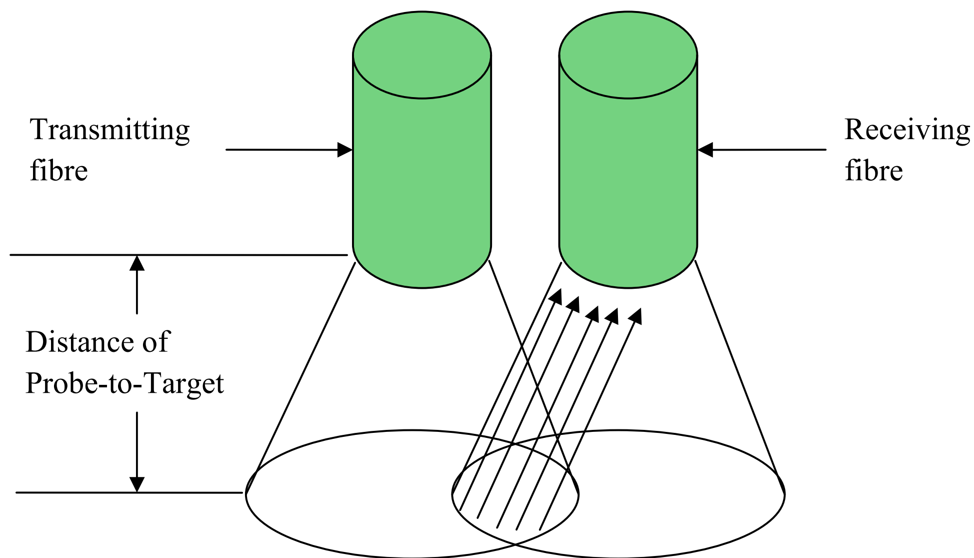

Figure 5-10 Schematic of displacement sensing mechanism of FS

There are two linear ranges within which the deflection of PZT cantilevers under applied electric filed can be measured (Figure 5-11) [134]. Range 1 has a highly sensitive positive slope response from direct contact to the optical peak. Range 2 has a less sensitive negative slope of the response extending from the peak to larger gaps. The optical peak is the zero slope portion of the response curve, where the maximum reflected light was captured by the receiving fiber. Range 1 provides higher sensitivity, however, it also provides a smaller range of measurement. Range 2 provides a relatively larger measurement range with a lower resolution. Selection of the range type will depend on the details of the measurement. The specific parameters (measurement range, resolution, et al) of the probe module can be found in the instrument manual [133]. In this study, 2032R and 2032RX module were employed.

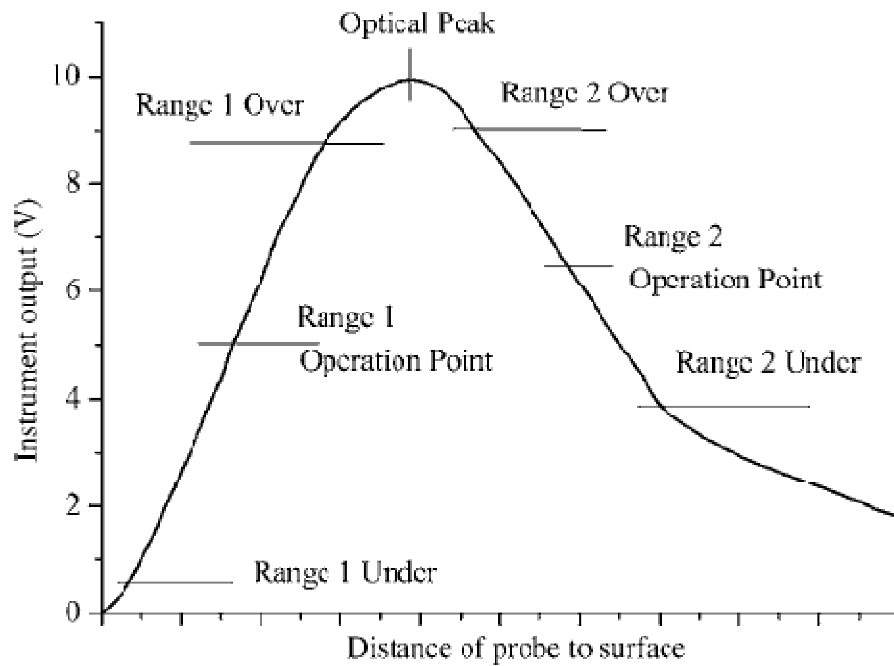

Figure 5-11 Typical calibration curve of FS

5.3 Analytical model for predicting the distribution of residual stress in PZT cantilever

As discussed before, residual stress is one of the most important factors that affect the electrical properties of PZT films. Therefore, investigation of stress distribution in the released PZT cantilevers will greatly help us to design the structures of devices and improve their performance. In this study, the microstructure, orientation and process conditions of the PZT film layers of the devices are the same; the residual stress will be the function of Si substrate thickness.

In the case of PZT film with un-etched Si substrate, the residual stress originates from the growth of film and the heat treatment. Since the same experimental conditions were employed to fabricate the PZT films on the Si based wafer, the residual stress conditions in the multilayer should remain constant. However, after PZT cantilevers were released through back-side etching, the structures will bend due to the removal of the constraints, resulting in a partial relaxation of the stress and different residual stress distribution [135]. Thus, the residual stress of released PZT cantilever consists of two parts: (1) the initial one in the constrained planar state, which causes the PZT cantilever to deform after constrains are removed; (2) the one from the bending of the devices. Figure 5-12 is the schematic of the stress distribution of the PZT multilayered structure. Figure 5-12 (a) shows the initial stress distribution. Figure 5-12 (b) shows the stress distribution caused by the bending of the released PZT cantilever.

The residual stress in the released PZT cantilever can be expressed as the following equation:

$$\sigma_{res}(z) = \sigma_{ini} + \sigma_{ben}(z) \quad (0 \le z \le t) \tag{5-1}$$

where σ_{res} is the residual stress in the released PZT cantilevers, z is the distance from the bottom of the structure, and t is total thickness of the PZT film structure.

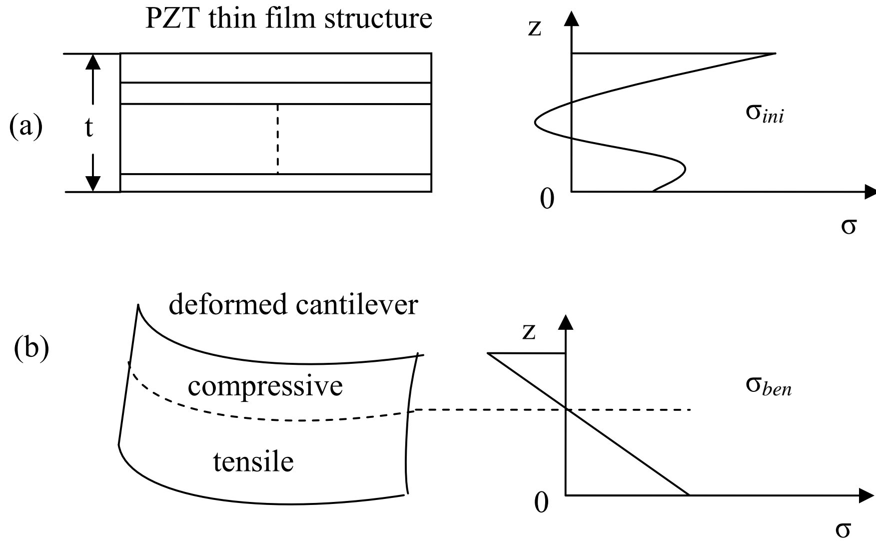

Figure 5-12 Schematic of the stress condition (a) an arbitrary profile of the distributed stress in the constrained PZT thin film (b) the "bending stress"

During the cooling process, PZT will experience a structural phase transition from a high-temperature paraelectric phase into a low-termperature ferroelectric phase. Since the Si substrate is much thicker than other layers, we may estimate the initial stress resulting from the thermal mismatch between film and substrates according to the following equations [136]:

$$\sigma_r(T) = (\alpha_{para}^{PZT} - \alpha^{Si})(650 - T)E_f / (1 - \nu_f) \quad \text{for } T \geq T_c \qquad (5\text{-}2)$$

$$\sigma_r(T) = \left[(\alpha_{para}^{PZT} - \alpha^{Si})(650 - T_c) + (\alpha_{ferro}^{PZT} - \alpha^{Si})(T_c - T)\right]E_f / (1 - \nu_f) \quad \text{for } T < T_c \qquad (5\text{-}3)$$

where α_{para}^{PZT} , α_{ferro}^{PZT} , and α^{Si} are the coefficients of thermal expansion (CTEs) of paraelectric , ferroelectric PZT and Si, respectively. The corresponding values are $6.1\text{x}10^{-6}\text{K}^{-1}$ [137], $32.1\text{x}10^{-6}\text{K}^{-1}$ [137]and $5.0\text{x}10^{-6}\text{K}^{-1}$ [138]. E_f ,ν_f are the modulus and Poisson's ration of the PZT film, respectively. $T_c \approx 300^0\text{C}$ is the Curie temperature for the

PZT films [136]. The annealing temperature we used in experiments for crystallization of PZT is 650^{0}C.

According to previous experimental results, we know the modulus for (111)-oriented PZT film is 152GPa and the Poisson's ratio is 0.3. Therefore, the calculated residual stress at room temperature (25^{0}C) is 1.73GPa. In chapter 3, we reported that the measured residual stress in (111)-oriented PZT film is 95.5MPa by Raman. Since the same fabrication conditions of PZT films were employed in both cases, the residual stress value in un-released PZT cantilevers should be close to those in PZT films discussed in chapter 3; however, the calculated value is much larger than the one we measured. Zhao et al [136] reported similar phenomena. They pointed out that the relaxation of film stress may be a possible reason to decrease the film stress level, by means of the evolution of the electric domain, Ti diffusion or dislocation nucleation. Xu et al [139] also found that various stress-relief mechanisms, such as dislocation nucleation and multiplication, film cracking, surface roughening, etc., will operate to release the residual stress as film thickness increases. Therefore, the calculated value significantly overestimates the residual stress in the PZT film due to the influence of one or more stress relaxation mechanisms. For the calculation of the residual stress distribution in PZT cantilevers, the measured initial stress, 95.5MPa, will be employed.

The Stoney's equation is widely used for assessing the stress from the curvature [135, 140-143]. Equation (5-4) is the expression of Stoney's equation for the residual stress of a film-substrate structure [143].

$$\sigma_{St} = \frac{E_s^{'} t_s^2}{6 t_f} K \tag{5-4}$$

where σ_{St} is the residual stress in the film, $E_s^{'} = \frac{E_s}{1-\nu}$ is the biaxial modulus of the substrate, *K* is bending curvature of the structure and t_s , t_f are the thickness of the substrate and film, respectively.

However, the application of Stoney's equation requires a thin-film approximation which usually needs a film to substrate thickness ratio of less than 1% such that the error does not exceed 5%. Since the designed Si thickness varies from 500μm to 65μm, Stoney's equation may not be accurate enough to evaluate the residual stress distribution in PZT cantilevers with a wide range of Si thickness. The following work will assess the accuracy of Stoney's equation when the film/substrate thickness ratio varies from 0 to 0.5.

Klein [143] gave an equation based on Townsend's work [144] to describe the stress distribution in the film, accounting for the planar contribution resulting from the initial strain mismatch plus the bending contribution, which is expressed as follows:

$$\sigma_f(z) = E_f^{'}\left[\frac{E_s^{'}t_s}{E_s^{'}t_s + E_f^{'}t_f}\Delta\varepsilon_0 + \left(\frac{t_s + t_f}{2} - \theta - z\right)K\right] \tag{5-5}$$

where $E_f^{'} = \frac{E_f}{1-\nu}$ is the biaxial modulus of the film, $\Delta\varepsilon_0$ characterizes the strain mismatch prior to any mechanical relaxation.

$$K = \frac{-E_s^{'}t_s E_f^{'}t_f(t_s + t_f)}{G(E_s^{'}t_s + E_f^{'}t_f)}\Delta\varepsilon_0 \tag{5-6}$$

$$G = E_s^{'}t_s^2(t_f/2 - t_s/6 - \theta) - E_f^{'}t_f\left[t_s(t_s + t_f/2) + t_f^2/6 + \theta(2t_s + t_f)\right] \tag{5-7}$$

The parameter θ,

$$\theta = \frac{t_s t_f(E_s^{'} - E_f^{'})}{2(E_s^{'}t_s + E_f^{'}t_f)} \tag{5-8}$$

specifies the position of the neutral plane, which deviates from the half-thickness plane for bilayered structures having different elastic moduli.

The first term of Equation (5-5) in the square bracket represents the initial stress contribution resulting from strain mismatch and the second term represents the bending stress contribution. For the time being, we assume the PZT film structure as a two-layer structure by ignoring other very thin layers and the residual stress is uniform in the film. With z set equal to $t_s + t_c / 2$, we thus obtain the average stress in the film according to Equation (5-5)

$$\overline{\sigma_f} = E_f^{'} \left[\frac{E_s^{'} t_s}{E_s^{'} t_s + E_f^{'} t_f} \Delta\varepsilon_0 - (\frac{t_s}{2} + \theta) K \right] \tag{5-9}$$

Combined with Equation (5-4), the ratio of average stress to the “Stoney stress” can be expressed as follows:

$$\frac{\overline{\sigma_f}}{\sigma_{St}} = \frac{6E_f^{'} t_f}{E_s^{'} t_s} \left[\frac{E_s^{'} t_s}{E_s^{'} t_s + E_f^{'} t_f} \frac{\Delta\varepsilon_0}{t_s K} - (\frac{1}{2} + \frac{\theta}{t_s}) \right] \tag{5-10}$$

with $\gamma = E_f^{'} / E_s^{'}$, $\delta = t_f / t_s$ the equation (5-10) can be rewritten as follows:

$$\frac{\overline{\sigma_f}}{\sigma_{St}} = \frac{1 + \gamma\delta^3}{1 + \delta} \tag{5-11}$$

an “error” is then defined to assess the accuracy of the Stoney’s equation, which is listed below:

$$\varepsilon_{St} = \left(\sigma_{St} - \overline{\sigma_f}\right) / \overline{\sigma_f} \tag{5-12}$$

substituting in Equation (5-11) leads to,

$$\varepsilon_{St} = \frac{\delta\left(1 - \gamma\delta^2\right)}{1 + \gamma\delta^3} \tag{5-13}$$

With E_{Si}=163GPa [145] and E_{PZT}=152GPa, the dependence of error on the thickness ratio can be obtained, as shown in Figure 5-13. The error increases as the increasing thickness ratio, which means Stoney's equation becomes less accurate as the thickness of Si substrate decreases. 1% error corresponds to 100 µm Si substrates in the curve. Therefore, when the Si thickness is above 100µm, application of Stoney's equation will not result in serious error and the cantilever bending could be very small and negligible. Consequently, the influence of cantilever bending on residual stress distribution in PZT film is not so significant and the initial strain mismatch dominates. Since the initial strain is almost the same, the residual stress condition in PZT cantilevers with Si substrate larger than 100 µm could be expected to be similar. For PZT cantilevers with thinner Si substrate, Equation (5-9) should be employed to describe the residual stress distribution.

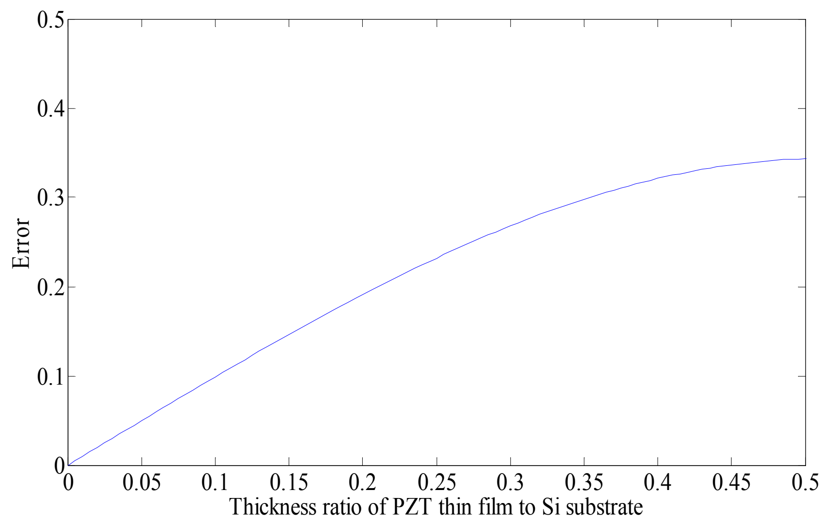

Figure 5-13 The errors involved in using Stoney's equation to calculate the residual stress in PZT film structure with varying Si thickness

5.4 Results and discussion

5.4.1 Si substrate thickness measurement

The fabricated cantilever arrays on the whole wafer are presented in Appendix C and the released cantilever arrays are shown in Figure 5-14. Since the well-known lag effect during the DRIE results in various etching rates [131] on different feature sizes and the non-uniform distribution of plasma also causes different etching rate in different regions, the actual Si thickness of each cantilever in different positions of the wafer will be different from the designed one. This was also demonstrated by the observed various releasing times of the cantilevers. During the back-side etching process, the cantilevers experiencing a high etching rate will be released at first; however, since the etching process will be continued until the last one is released, the excess etching time will generate some thinner cantilevers than expected. To accurately determine Si substrate thickness for each cantilever, SEM characterization was employed. The cantilevers were detached from the anchors after the electric properties were measured and then vertically attached to the sample holder so that the cross-section could be focused on directly. Figure 5-15 shows a SEM image for a PZT thin film structure cross-section. Several locations of the cross-section were employed to obtain the average value of film thickness. At each location, at least 3 tests were performed to get the average film thickness for the specific location. The measured values were summarized in Table 5.3

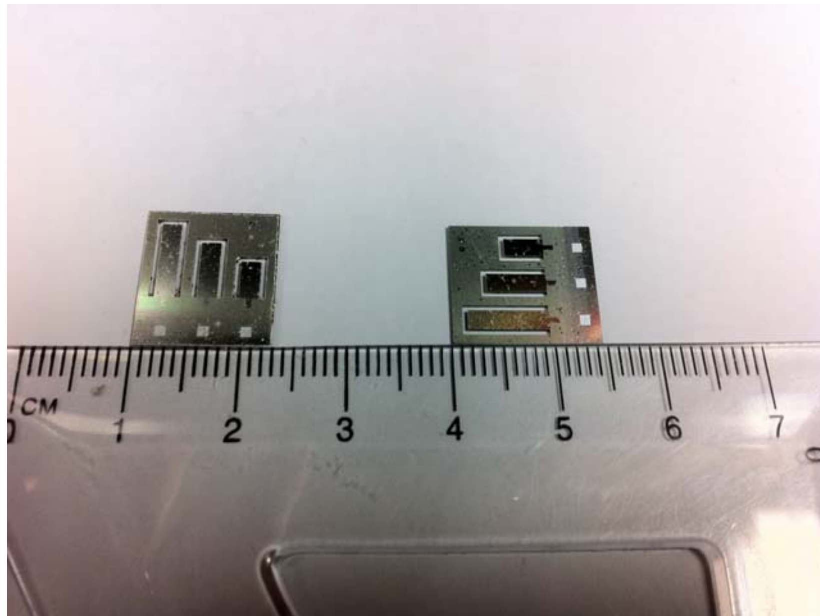

(a)

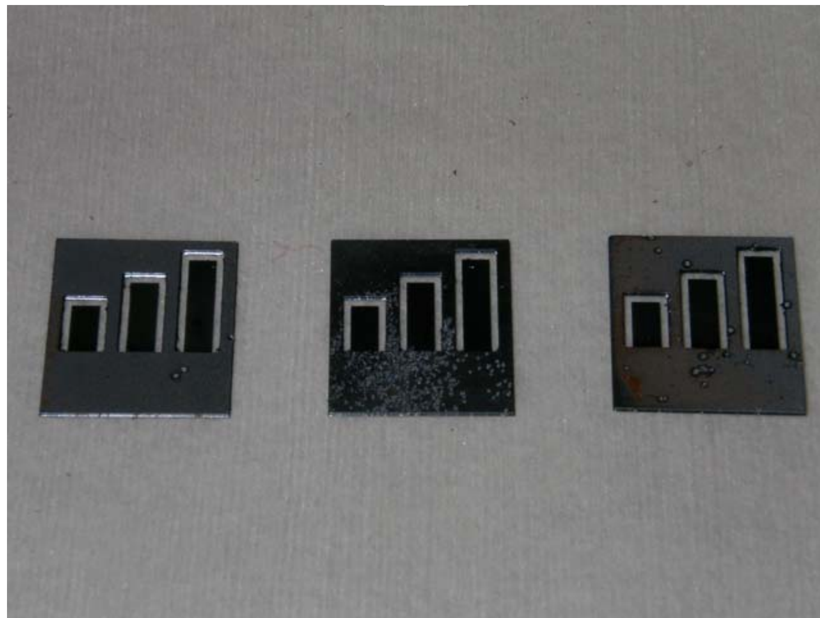

(b)

Figure 5-14 Picture of fabricated cantilever array (a) front view (b) back view

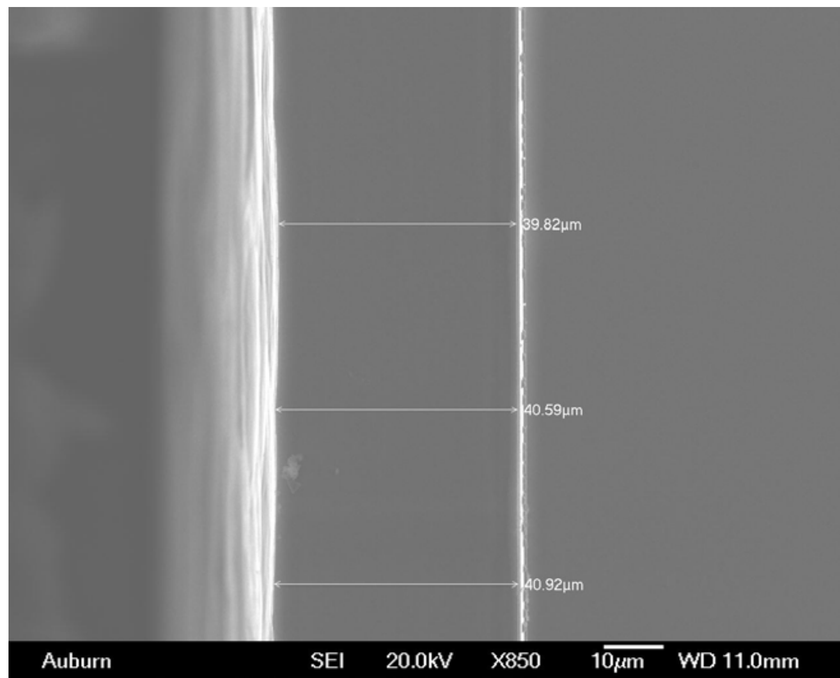

Figure 5-15 The cross-sectional SEM image of a PZT thin film structure

5.4.2 Calculated residual stress by the developed model

Figure 5-16 shows residual stress and bending curvature as a function of Si substrate thickness, which was determined by substituting parameters of PZT film and Si substrate into Equation (5-9).

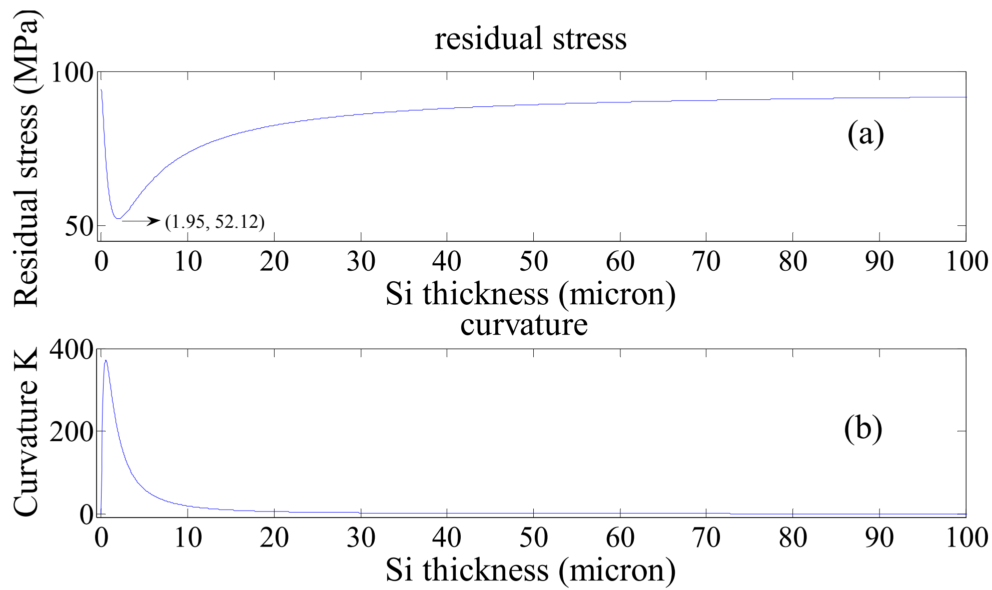

Figure 5-16 The plots of (a) the residual stress and (b) bending curvature as a function of Si substrate thickness

It was observed that residual stress decreases as Si thickness decreases. When the Si thickness is close to ~30µm, the reduction of residual stress starts to become significant. However, the serious bending of the cantilever has not started, as indicated by the bending curvature in Figure 5-16 (b). This is probably due to the thick Si substrate which suppresses the influence of the residual stress. As Si thickness keeps decreasing, the Residual stress-Si thickness curve becomes steep and residual stress decreases rapidly, which indicates the bending contribution to the residual stress becomes significant. After reaching the minimum value at 1.95 µm of the Si thickness, the tensile residual stress begins to increase. This should be attributed to the bending induced tensile stress transiting from the substrate to the film as the neutral axis approaches the PZT film.

For the verification of this model, the tip displacement and remaining Si substrate thickness of two released cantilevers with length of 6mm (Figure 5-18) and 8mm (Figure 5-19) were measured by SEM. The obtained values were listed in Table 5.2.

Table 5.2 Comparison of calculated curvatures from the experimental results and developed model for two cantilevers

#	Length (mm)	Tip disp. (μm)	Si thickness (μm)	Curvature (Eq.5-17)	Curvature (model)	Residual stress (MPa)
1	6	7.9~10.7	87.97	0.44~0.6	0.49	90.93~89.86,90.60
2	8	10.2~12.3	99.99	0.32~0.38	0.38	91.58~91.10,91.10

It is known that the reciprocal of the curvature radius (*R*) of a curve *w*(x), namely, bending curvature (*K*), equals the value of the second derivative of *w*(x) [146], as listed below,

$$K = \frac{1}{R} = w^{'}(x) \qquad (5\text{-}14)$$

For the cantilever structure (Figure 5-17), with boundary conditions: $w(0) = 0, w^{'}(0) = 0$, the solution of Equation (5-14) is

$$w(x) = \frac{1}{2R} x^2 \text{, } (0 \le x \le L) \qquad (5\text{-}15)$$

where *L* is the length of the cantilever.

Then the tip displacement δ can be written as

$$\delta = w(L) = \frac{1}{2R} L^2 \qquad (5\text{-}16)$$

The corresponding bending curvature will be

$$K = \frac{2\delta}{L^2} \qquad (5\text{-}17)$$

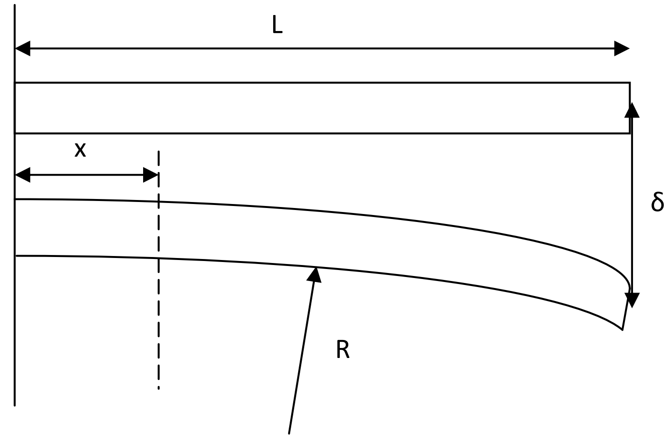

Figure 5-17 The schematic of the deformed cantilever

Substituting the length and measured tip displacement of the cantilevers into Equation (5-17), the bending curvatures can be determined. Due to the large gap between the cantilever and anchor, they couldn't be focused simultaneously. Therefore, the estimated tip displacement is in the range of 7.90μm to 10.70μm for the 6mm long cantilever, and 10.2μm to 12.3μm for the 8mm long cantilever, respectively. The measured tip displacement of the 6mm long cantilever is in the range of 7.90μm to 10.70μm. The corresponding bending curvatures calculated by Equation (5-17) were listed in Table 5.2.

With the measured Si thickness, the bending curvature can be calculated based on the developed model (Eq.5-6~Eq.5-8). The results were also listed in Table 5.2, which reasonably match the calculated results by Equation (5-17) based on experimental data , with no significant difference was observed. Substituting those curvature values into Equation (5-9), the corresponding residual stress values can be obtained. The calculated

values based on Equation (5-17) were found to match rather well with those based on the developed model for both cantilevers. Therefore, the model will be able to predict the residual stress condition in the released cantilever if we know the stress condition in PZT film.

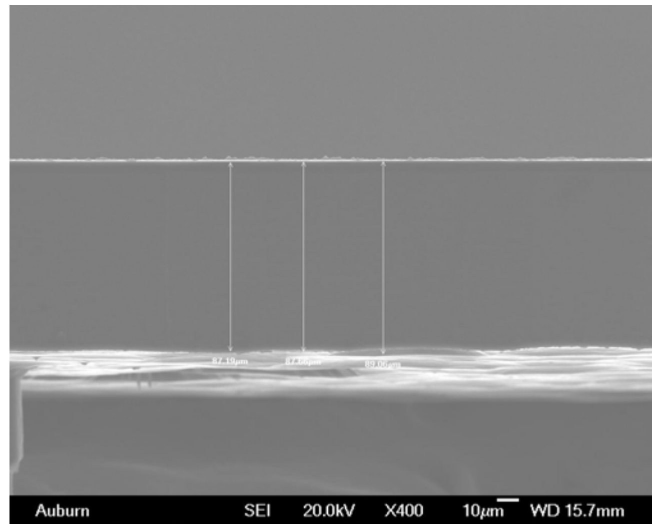

(a)

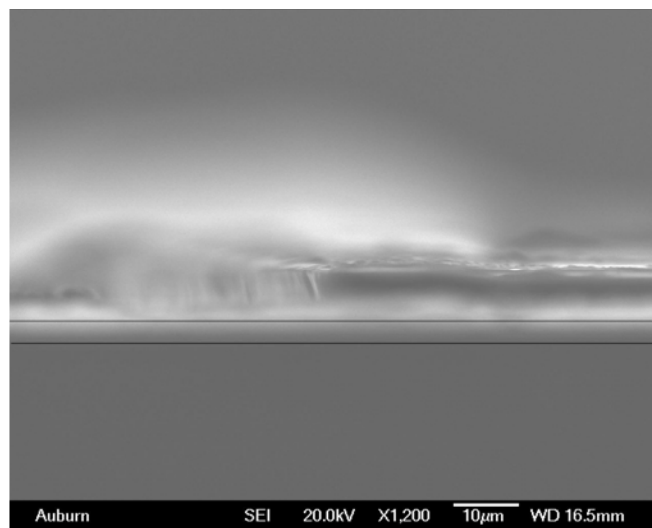

(b)

Figure 5-18 SEM images of (a) the cross-section of Si substrate (b) free end of the curved cantilever (6mm)

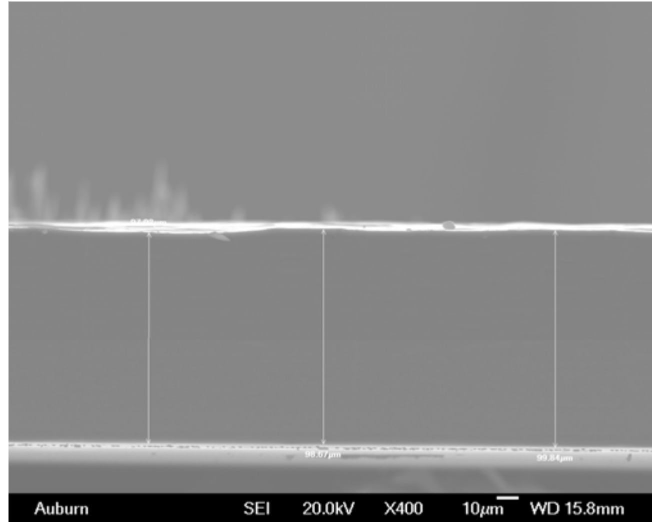

(a)

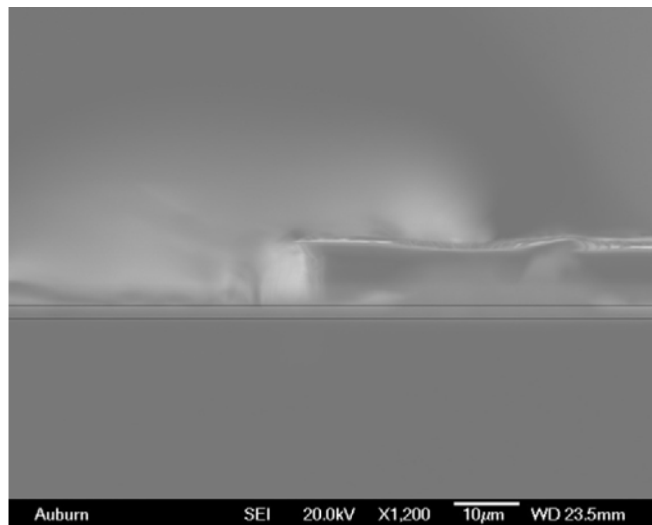

(b)

Figure 5-19 SEM images of (a) the cross-section of Si substrate (b) free end of the curved cantilever (8mm)

5.4.3 Electrical properties and piezo-response of PZT cantilevers with different Si substrate thickness

It is known that the electric properties of ferroelectric films depend on many factors such as composition, microstructure, orientation, film thickness, interface between the electrode and the film, residual stress etc [116, 120, 147, 148]. In this work, since other factors have been held constant, the change of residual stress due to varying Si thickness is expected to be the exclusive reason which results in variations in the ferroelectric properties, dielectric properties and piezoelectric property. After lithography, patterning, etching and cleaning processes, some of the obtained devices were found broken, and the top electrodes of some cantilevers were peeled off. The c type of cantilevers were found to be least damaged and included a broader range of Si thickness. Therefore, they were chosen for investigation of the Si thickness dependence of electrical and piezoelectric properties.

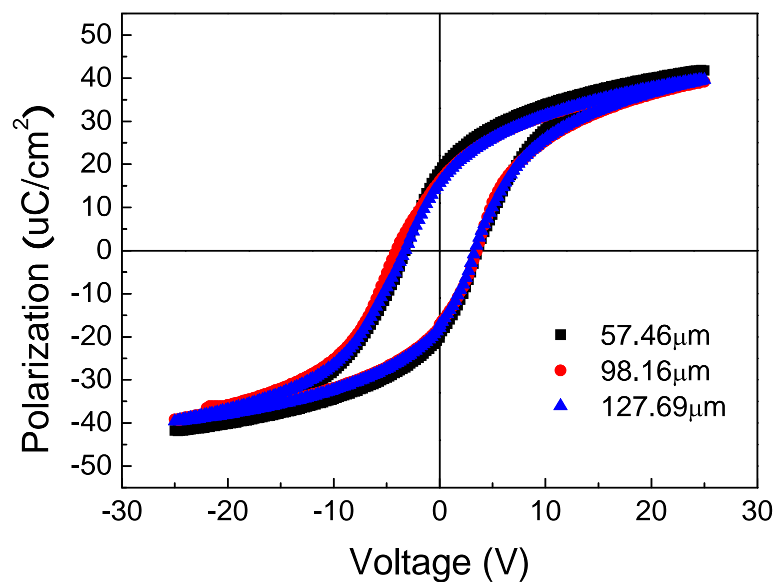

Figure 5-20 Ferroelectric hysteresis loops measured at maximum applied voltage of 25V for all cantilevers

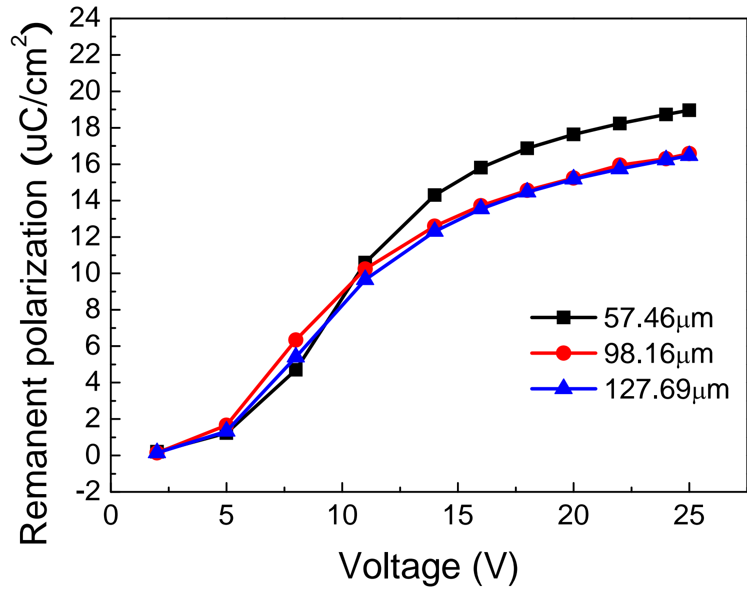

Figure 5-21 The remanent polarization as a function of the applied voltage for all cantilevers

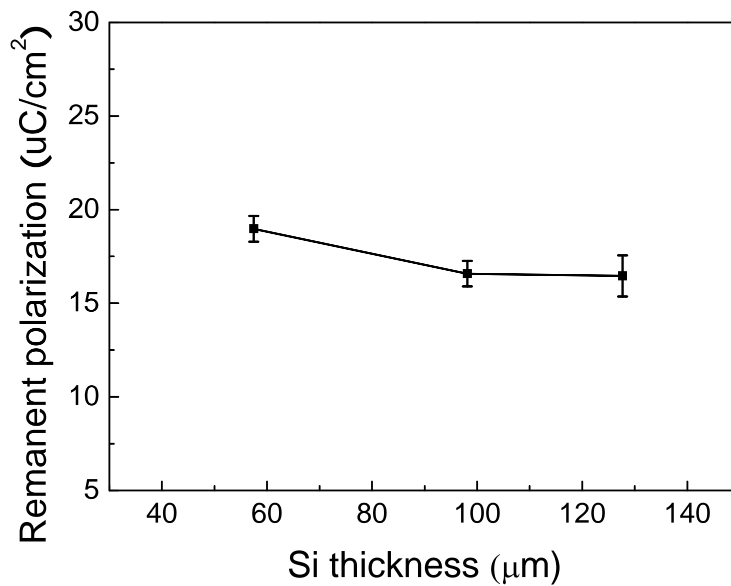

Figure 5-22 The remanent polarization as a function of the Si thickness

The polarization hysteresis loops for cantilevers with different Si thicknesses were measured at a maximum applied voltage of 25V, as shown in Figure 5-20. The plot of the

remanent polarization as a function of the applied voltage was given in Figure 5-21.The values of remanent polarization are the average of the positive and negative remanent polarization values ($P_{r.avg} = (|P_r^+| + |P_r^-|)/2$). The remanent polarization value increases as the voltage increases and eventually reaches a relatively constant value, which is considered the saturated value. In this work, the value at an applied voltage of 25V was employed and listed in Table 5.3 for all of the samples. The Si substrate thickness dependence of remanent polarization was shown in Figure 5-22. The value decreases as the Si substrate thickness increases at the very beginning and becomes relatively constant as the Si thickness reaches a critical value. This is expected because the residual stress increases as Si thickness increases; however, the change of residual stress will not be significant as the Si substrate becomes relatively thicker, as we demonstrated by using the model developed previously. It is known that residual stress affects the reorientation of perovskite domains [149-151]. Compressive stress usually results in the domains orienting along the longitudinal direction of the sample. Tensile stress, however, tends to causes the domains parallel to the lateral direction. Since the polarity in PZT is along the longer c axis [151], the residual tensile stress will cause the reduction of ferroelectric properties.

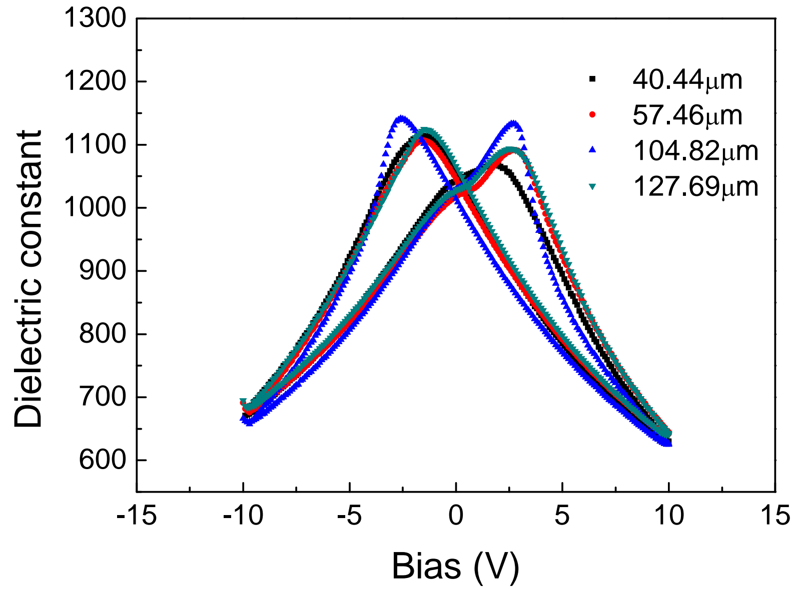

Figure 5-23 Field dependence of the dielectric constant of all cantilevers

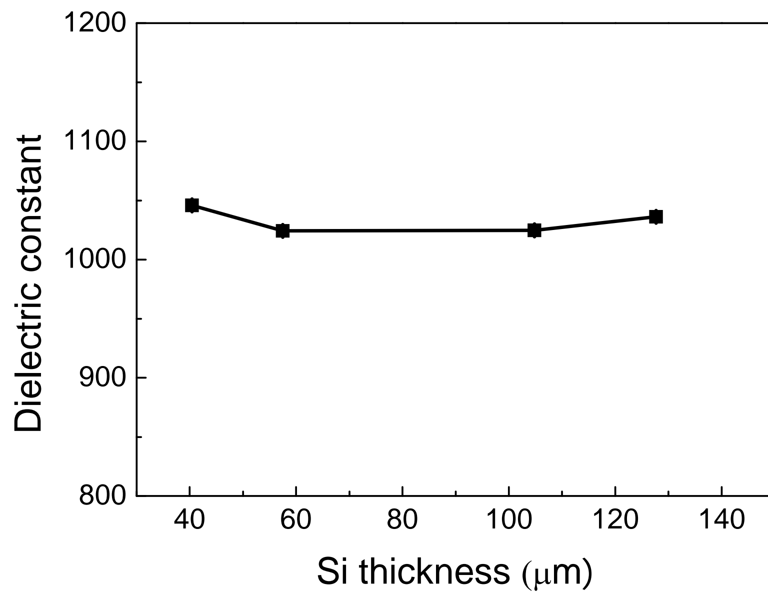

Figure 5-24 The dielectric constant as a function of the Si thickness

Figure 5-23 illustrates room temperature dielectric constants of PZT cantilevers with different Si thicknesses as a function of dc bias at 1000Hz. The typical symmetric

"butterfly"' curves were observed for all samples. The Si substrate thickness dependence of dielectric constant is shown in Figure 5-24. This tendency is very similar to the one for ferroelectric properties. Many researchers reported that the dielectric constant decreased as tensile stress increased [116, 150, 152]. It has been suggested that the reduced properties were attributed to increasing suppressing effect of residual stress on the polarization switching and domain motions. In addition, Fu et al. proposed a modified Devonshire theory to quantitatively evaluate the stress dependence of dielectric constant [153]. The free energy of the PZT material was described as a function of polarization and stress based on conventional Landau-Devonshire approach. Under the assumption of only a biaxial stress in the plane of the film, which is true in the case of PZT film, the relationship between the residual stress and dielectric constant can be expressed as:

$$\frac{\partial \varepsilon^{-1}}{\partial \sigma} = \text{Constant } (>0) \tag{5-14}$$

This equation clearly shows that the dielectric constant will decrease as the increasing residual stress (tensile).

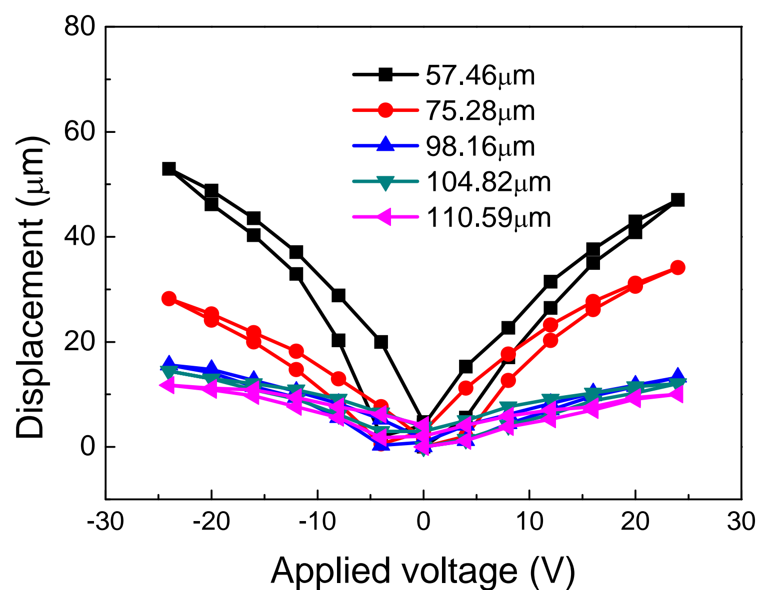

Figure 5-25 Tip displacement of the cantilevers as a function of the applied voltage

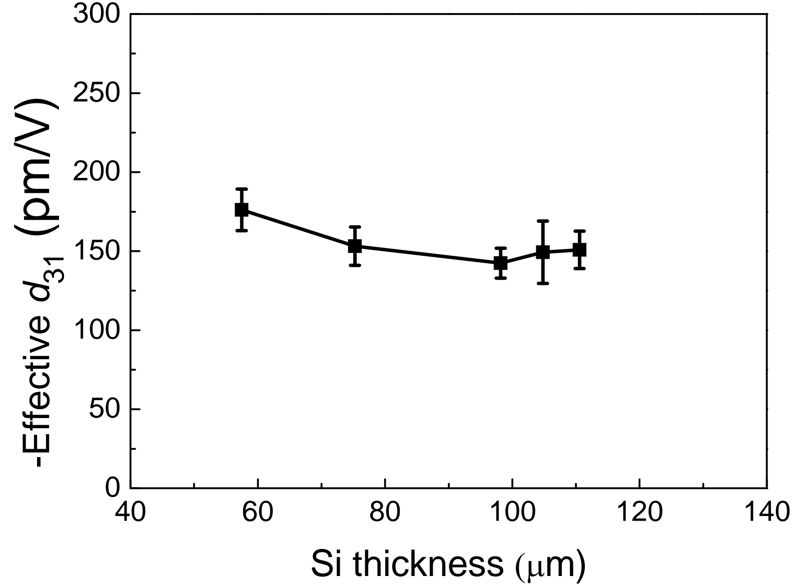

Figure 5-26 The piezoelectric coefficient d_{31} as a function of Si thickness

Figure 5-25 shows the tip displacement of PZT cantilevers with different Si thicknesses as a function of applied electric field. It is a plot of the simple displacement of each cantilever and therefore cannot be used as a direct comparison of piezo-response because of differences in Si substrate thickness and effective beam length. Therefore, the following equations were used to calculate the effective coefficients d_{31},

$$d_{31,eff} = -\frac{4E_sE_ft_st_f(t_s^2+t_f^2)+E_s^2t_s^4+E_f^2t_f^4+6E_sE_ft_s^2t_f^2}{3E_sE_ft_s(t_s+t_f)L^2V} \bullet h \tag{5-15}$$

where h is the tip displacement of the PZT cantilever under 24V DC voltage. E_s and E_f are modulus (E_s=170 GPa and E_f=152 GPa^{-1}), t_s and t_f the thickness (t_f=1.13[μm]), of the Si substrate and PZT cantilever. L is the effective cantilever length. The calculated effective d_{31} values were listed in Table 5.3 and the evolution of the effective d_{31} as a function of the Si substrate thickness was shown in Figure 5-26. - $d_{31,eff}$ decreases quickly

at small Si thickness and becomes relatively constant at a larger Si thickness. The Si thickness dependence of the piezoelectric coefficient ($d_{31,\mathrm{eff}}$) is also related to a varying residual stress condition in the PZT film. The residual stress was reported to result in ferroelectric domain pinning [154], which results in reduction in both linear and nonlinear contribution from domain motion to the piezoelectric coefficient [116].

Table 5.3 Summary of measured properties of PZT cantilevers

Cantilever #	Remanent polarization (μC/cm^2)	Dielectric constant at 1000Hz	Displacement h of the cantilever tip under 24V DC voltage (μm)	Effective cantilever length L (mm)	Si thickness t_s (μm)	Calculated d_{31} (pm/V)
6-11-1-1	-*	1046.65	-	-	40.44	-
6-7-3-1	18.97	1023.72	47.06	3.7	57.46	176.15
6-17-3-1	-	-	34.12	3.7	75.28	153.24
6-7-1-1	16.58	-	13.24	3.7	98.16	142.43
6-7-4-1	-	1025.66	12.06	3.6	104.82	149.33
6-17-2-1	-	-	10.00	3.7	110.59	150.85
6-5-3-1	16.46	1035.19	-	-	127.69	-

*- indicates the devices were shorted or damaged after certain measurement. Therefore, the data are not available.

5.5 Chapter summary

Cantilevers with different sizes and Si thickness were designed and fabricated. The Si thickness was measured by the SEM. The ferroelectric, dielectric and piezoelectric properties (d_{31}) were measured and analyzed. The commonly used Stoney's equation was found to be infeasible to evaluate the residual stress condition in PZT cantilevers with Si

thickness less than 100 micron. An analytical model was developed and used to predict the residual stress condition in the released PZT cantilevers. The calculated results were similar to the measured experimental results.

It was observed that the ferroelectric, dielectric and piezoelectric properties of investigated PZT cantilever showed very similar Si thickness dependence. The measured values decrease with increasing Si thickness at the beginning and become relatively constant as Si thickness increases. The change of these properties was attributed to the different residual tensile stress conditions in PZT cantilevers with varying Si thicknesses. A PZT cantilever with a thicker Si substrate will experience less bending contribution, thus resulting in smaller relaxation of the stress. The higher residual stress level causes larger reduction of polarization switching and domain mobility, which is indicated by the lower measured properties.

Chapter 6 Conclusion and Future Work

6.1 Conclusions

The effects of the structural layer in substrates on the mechanical and electrical properties of $Pb(Zr_{0.52}Ti_{0.48})O_3$ films for MEMS were investigated. The PZT films were deposited by a sol-gel method on platinized silicon substrates where silicon nitride and silicon oxide were used as a structural layer. The mechanical properties of PZT films were characterized by nanoindentation. The ferroelectric and dielectric properties as a function of film thickness and layer material were investigated. Residual stresses in PZT films were also characterized by Raman spectroscopy. The use of a structural layer such as silicon dioxide or silicon nitride resulted in a difference in the Young's moduli of the PZT films obtained from nanoindentation measurement. The flat region modulus values at small depths represent the combined response of PZT films and substrates and scale with the substrate modulus. The measured Young's moduli of the PZT films on SiNx-based substrates show higher values than those of the PZT films on SiO_2-based substrate for indentation depths up to 2200nm. The results indicate that the substrate effect may be unavoidable during the whole indentation process without a complete analytical solution in order to extract the true values from the flat region of the modulus values; however, the structural layer does not show significant influence on the hardness of PZT films. The measured values were about 8.8GPa because the plastic deformation was entirely

contained in PZT film due to the harder substrate material. Irrespective of the types of structural layer, similar electrical properties were observed in the characterized PZT thickness range. Similar microstructure and texture of the PZT films in addition to residual stress conditions determined by Raman characterization appear to be the reasons for similar electrical properties.

To extract the film modulus value from the measured flat region and get the true crystalline orientation dependence of the modulus of PZT film, a new model of film indentation based on discontinuous transfer of elastic strain was employed to assess properties. The crystalline orientations of the PZT films on two different types of substrates were controlled by both a chelating agent and pyrolysis temperature. It was found that the measured modului of PZT films on the two types of substrates showed similar orientation dependence ($E_{001}>E_{111}>E_{(110,111)}$) but distinct values, which indicated a clear substrate effect. By using the new model, the effects of film orientation and structural layer type on the Young's modulus were deconvoluted. PZT films with significant (001) and (111) orientation appear to agree well with less than two percent difference between their average values for two substrates. For PZT films with mixed orientation of (110) and (111), it was observed that the modified modulus of PZT film on SiNx-based substrate is still larger than the one of PZT film on SiO_2-based substrate. This result could be attributed to the fact that the (111) orientation account for a large portion of the measured modulus since we randomly chose the indentation positions.

PZT cantilevers with different sizes and thicknesses were designed and fabricated. The ferroelectric, dielectric and piezoelectric properties of the MEMS devices were measured and the Si thickness dependence of those properties was investigated. Results

obtained show that varying Si thickness changed the residual stress condition in the PZT cantilever, due to the bending contribution stemming from the curvature K. The developed model appears adept at predicting the residual stress in the released cantilevers. The residual stress increases with increasing Si substrate and becomes relatively constant as the Si substrate thickness is getting larger, as do the measured properties.

6.2 Future works

The structural layer was proved to affect the measured mechanical properties due to the substrate effect. Meanwhile, it was also found to result in different fracture behaviors when a high load was applied to the samples. One of the major concerns of MEMS devices is their relatively poor reliability caused by the fracture, delamination and fatigue degradation of their multilayer structure. Therefore, it is necessary to perform a study on the influence of the structural layer on fracture behavior of PZT thin film and MEMS devices. Nanoindentation is still a very useful, commonly used tool.

In the finished work, the multilayer structure was assumed a three layer structure by ignoring several thin layers to extract the film modulus. The experiment will generate more accurate results if a multilayer model can be developed.

The Si thickness of the PZT cantilevers could be precisely controlled if a SOI wafer was used for fabrication. The model for predicting the residual stress in the PZT cantilevers could be improved by considering gradient stress.

Bibliography

[1] J. Baborowski, "Microfabrication of piezoelectric MEMS," *Journal of Electroceramics,* vol. 12, pp. 33-51, 2004.

[2] M. Tanaka, "An industrial and applied review of new MEMS devices features," *Microelectronic Engineering,* vol. 84, pp. 1341-1344, 2007.

[3] V. K. Varadan, K. J. Vinoy, and S. Gopalakrishnan, *Smart Material Systems and MEMS: Desigh and Development Methodologies*. USA: Wiley, 2006.

[4] S. Trolier-Mckinstry and P. Muralt, "Thin film piezoelectrics for MEMS," *Journal of Electroceramics,* vol. 12, pp. 7-17, 2004.

[5] S. Xiong, H. Kawada, H. Yamanaka, and T. Matsushima, "Piezoelectric properties of PZT films prepared by the sol-gel method and their application in MEMS," *Thin Solid Films,* vol. 516, pp. 5309-5312, 2008.

[6] B. Jaffe, W. R. Cook, and H. Jaffe, *Piezoelectric Ceramics*. London: Academic press, 1971.

[7] P. Muralt, "Ferroelectric thin films for micro-sensors and actuators: a review," *Journal of Micromechanics and Microengineering,* vol. 10, pp. 136-146, 2000.

[8] I. Kanno, S. Fujii, T. Kamada, and R. Takayama, "Piezoelectric properties of c-axis oriented Pb(Zr, Ti)O3 thin films," *Applied Physics Letters,* vol. 70, pp. 1378-1380, 1997.

[9] K. Lefki and G. J. M. Dormans, "Measurement of piezoelectric coefficients of ferroelectric thin films," *Journal of Applied Physics,* vol. 76, pp. 1764-1767, 1994.

[10] J. F. Shepard, Jr., P. J. Moses, and S. Trolier-McKinstry, "The wafer flexure technique for the determination of the transverse piezoelectric coefficient (d31) of PZT thin films," *Sensors and Actuators, A: Physical,* vol. 71, pp. 133-138, 1998.

[11] D. F. Bahr, J. S. Robach, J. S. Wright, L. F. Francis, and W. W. Gerberich, "Mechanical deformation of PZT thin films for MEMS applications," *Materials Science & Engineering A: Structural Materials: Properties, Microstructure and Processing,* vol. A259, pp. 126-131, 1999.

[12] H. Wu, L. Wu, Q. Sun, W. Fei, and S. Du, "Mechanical properties of sol-gel derived lead zirconate titanate thin films by nanoindentation," *Applied Surface Science,* vol. 254, pp. 5492-5496, 2008.

[13] X. J. Zheng, Y. C. Zhou, and J. Y. Li, "Nano-indentation fracture test of Pb(Zr0.52Ti0.48)O3 ferroelectric thin films," *Acta Materialia,* vol. 51, pp. 3985-3997, 2003.

[14] P. Delobelle, G. S. Wang, E. Fribourg-Blanc, and D. Remiens, "Mechanical properties measured by nano-indentation of Pb(Zr, Ti)03 sol-gel films deposited on Pt and LaNi03 electrodes," *Surface and Coatings Technology,* vol. 201, pp. 3155-3162, 2006.

[15] X. H. Xu, P. Gu, R. Jiang, G. Zhao, L. Wen, and J. R. Chu, "Characterization of Mechanical Properties of PZT Thin Film by Nanoindentation," in *Proceedings of 1st IEEE International Conference on Nano/Micro Engineered and Molecular Systems*, Zhuhai,China, 2006, pp. 56-60.

[16] C. K. Kwok and S. B. Desu, "Formation kinetics of $PbZr_xTi_{1-x}O_3$ thin-films," *J. Mater. Res.,* vol. 9, p. 1728, 1994.

[17] P. Delobelle, E. Fribourg-Blanc, and D. Remiens, "Mechanical properties determined by nanoindentation tests of [Pb(Zr,Ti)O3] and [Pb(Mg1/3Nb2/3)1-xTixO3] sputtered thin films," *Thin Solid Films,* vol. 515, pp. 1385-1393, 2006.

[18] Q.-M. Wang, Y. Ding, Q. Chen, M. Zhao, and J. Cheng, "Crystalline orientation dependence of nanomechanical properties of $Pb(Zr_{0.52}\ Ti_{0.48})O_3$ thin films," *Applied Physics Letters,* vol. 86, p. 162903, 2005.

[19] I. M. Reaney, D. V. Taylor, and K. G. Brooks, "Ferroelectric PZT thin films by sol-gel deposition," *J. Sol-Gel Sci. Techn.,* vol. 13, p. 813, 1998.

[20] T. Tani, Z. Xu, and D. A. Payne, "Preferred orientations for sol-gel derived PLZT thin layers," in *Materials Research Society Symposium Proceedings*, San Francisco, CA, 1993.

[21] M. J. Madou, *Fundamentals of microfabrication: the science of miniaturization*, 2nd ed. New York, NY: CRC Press, 2002.

[22] P. Muralt, "Recent progress in materials issues for piezoelectric MEMS," *Journal of the American Ceramic Society,* vol. 91, pp. 1385-1396, 2008.

[23] Y. B. Jeon, R. S. , J. H. Jeong, and S.G. Kim, "Energy harvesting MEMS devices based on d_{33} mode piezoelectric $Pb(Zr,Ti)0_3$ thin film cantilever," in *CIRP Seminar on Micro and Nano Technology*, Copenhagen, Denmark,, 2003.

[24] S. Lu, C. Zuo, H. Zeng, W. Huang, and H. Ji, "Residual stress and structure characteristics in PZT ferroelectric thin films annealed at different ramp rates," *Materials Letters,* vol. 60, pp. 255-260, 2006.

[25] T. Ohno, H. Suzuki, H. Masui, K. Ishikawa, and M. Fujimoto, "Effect of back-etching on residual stress in lead titanate thin films on Si wafer," 2004, pp. 6549-6553.

[26] R. N. Torah, S. P. Beeby, and N. M. White, "Experimental investigation into the effect of substrate clamping on the piezoelectric behaviour of thick-film PZT elements," *Journal of Physics D: Applied Physics,* vol. 37, pp. 1074-1078, 2004.

[27] Blom F R, Y. D. J, V. d. P. F. C. M, E. M, F. J. H. J, and P. T. J. A, "Thin film zno as micromechanical actuator at low frequencies," *Sensors and Actuators A: Physical,* vol. 21-23, pp. 226-228, 1990.

[28] W. Tljhen, T. Tamagawa, C. P. Ye, C. C. Hsueh, P. Schiller, and D. L. Polla, "Properties of piezoelectric thin films for micromechanical devices and systems," Nara, Jpn, 1991, pp. 114-119.

[29] J. F. Antaki, G. E. Bertocci, E. C. Green, A. Nadeem, T. Rintoul, R. L. Kormos, and B. P. Griffith, "A gait-powered autologous battery charging system for artificial organs," Hagerstown, MD, United States, 1995, pp. M588-M595.

[30] D. L. Polla and L. F. Francis, "Processing and characterization of piezoelectric materials and integration into microelectromechanical systems." vol. 28 Palo Alto, CA, United States: Annual Reviews Inc, 1998, pp. 563-597.

[31] S. B.-G. Siegfried Bauer, Mario Dansachmueller, Gilles Dennler, Ingrid Graz, martin kaltenbrunner, christoph keplinger, Howard Reiss, Niyazi Serdar Sariciftci, Thokchom Birendra Singh, Reinhard Schwoediauer, "Piezoelectric polymers," in *Materials Research Society Symposium Proceedings*, 2006.

[32] J. L. Sanchez-Rojas, J. Hernando, A. Ababneh, U. Schmid, J. Olivares, M. Clement, and E. Iborra, "Advanced determination of piezoelectric properties of AlN thin films on silicon substrates," Beijing, China, 2008, pp. 903-906.

[33] http://www.piezo.com.

[34] M. Deshpande and L. Saggere, "PZT thin films for low voltage actuation: Fabrication and characterization of the transverse piezoelectric coefficient," *Sensors and Actuators A: Physical,* vol. 135, pp. 690-699, 2007.

[35] L. J. Bowen and K. W. French, "Fabrication of piezoelectric ceramic/polymer composites by injection molding," in *Proc. of the 8th IEEE International Symposium on Application of ferroelectrics*, 1992, pp. 160-163.

[36] http://www.brighthub.com/engineering/mechanical/articles/64859.aspx.

[37] http://www.virginia.edu/bohr/mse209/chapter6.htm.

[38] P. S. Alexopoulos and T. C. O. Sullivan, "Mechanical properties of thin films," *Ann. Rev. Mater. Sci.,* vol. 20, pp. 391-420, 1990.

[39] D. Ma, K. Xu, and J. He, "Numerical simulation for determining the mechanical properties of thin metal films using depth-sensing indentation technique," *Thin Solid Films,* vol. 323, pp. 183-187, 1998.

[40] I. Chasiotis and W. G. Knauss, "A new microtensile tester for the study of MEMS materials with the aid of atomic force microscopy," *Experimental Mechanics,* vol. 42, pp. 51-57, 2002.

[41] R. Liu, H. Wang, X. Li, G. Ding, and C. Yang, "A micro-tensile method for measuring mechanical properties of MEMS materials," *Journal of Micromechanics and Microengineering,* vol. 18, 2008.

[42] D. T. Read, "Silicon-framed tensile specimens: techniques and results," San Francisco, CA, USA, 1998, pp. 167-172.

[43] W. Sharpe Jr., "A new technique for measuring poisson's ratio of MEMS materials," in *Mater. Res. Soc. Symp. Proc.*, 1996, pp. 185-190.

[44] D. C. Hurley, V. K. Tewary, and A. J. Richards, "Thin-film elastic-property measurements with laser-ultrasonic SAW spectrometry," San Diego, CA, United states, 2001, pp. 326-330.

[45] P. Djemia, C. Dugautier, T. Chauveau, E. Dogheche, B. M. I. De, and L. Vandenbulcke, "Mechanical properties of diamond films: A comparative study of polycrystalline and smooth fine-grained diamonds by Brillouin light scattering," *Journal of Applied Physics,* vol. 90, pp. 3771-3771, 2001.

[46] C. J. Shute and J. B. Cohen, "Determination of yielding and debinding in Al–Cu thin films from residual stress measurements via diffraction," *J. Mater. Res.,* vol. 6, p. 950, 1991.

[47] S. Bader, E. M. Kalaugher, and E. Arzt, "Comparison of mechanical properties and microstructure of Al(1 wt.%Si) and Al(1 wt.%Si, 0.5 wt.%Cu) thin films," *Thin Solid Films,* vol. 263, pp. 175-184, 1995.

[48] S. P. Baker, A. Kretschmann, and E. Arzt, "Thermomechanical behavior of different texture components in Cu thin films," *Acta Materialia,* vol. 49, pp. 2145-2160, 2001.

[49] R. M. Keller, S. P. Baker, and E. Arzt, "Stress-temperature behavior of unpassivated thin copper films," *Acta Materialia,* vol. 47, pp. 415-426, 1999.

[50] P. Delobelle, G. S. Wang, E. Fribourg-Blanc, and D. Remiens, "Indentation modulus and hardness of Pb(Zr, Ti)O3 sol-gel films deposited on Pt and LaNiO3 electrodes. An estimation of the Ci jD compliances," *Journal of the European Ceramic Society,* vol. 27, pp. 223-230, 2007.

[51] T.-H. Fang, S.-R. Jian, and D.-S. Chuu, "Nanomechanical properties of lead zirconate titanate thin films by nanoindentation," *Journal of Physics Condensed Matter,* vol. 15, pp. 5253-5259, 2003.

[52] X. Huang and A. A. Pelegri, "Mechanical characterization of thin film materials with nanoindentation measurements and FE analysis," *Journal of Composite Materials,* vol. 40, pp. 1393-1407, 2006.

[53] F. Zhang, R. Saha, Y. Huang, W. D. Nix, K. C. Hwang, S. Qu, and M. Li, "Indentation of a hard film on a soft substrate: Strain gradient hardening effects," *International Journal of Plasticity,* vol. 23, pp. 25-43, 2007.

[54] D. Liu and K. W. White, "Mechanical aspects of epitaxial ferroelectric Pb(Zr0.5Ti 0.5)O3 films investigated by nanoindentation methods and piezoresponse force microscopy," *Applied Physics Letters,* vol. 85, pp. 3459-3461, 2004.

[55] http://www.charfac.umn.edu/InstDesc/nanoindenterdesc.html#Description.

[56] J. L. Hay and G. M. Pharr, "Instrumented indentation testing " in *ASM Handbook*, 10 ed. vol. 8:*Mechanical Testing and Evaluation*, H. Kuhn and D. Medlin, Eds.: ASM International, 2000, pp. 232-243.

[57] X. Li and B. Bhushan, "A review of nanoindentation continuous stiffness measurement technique and its applications," *Materials Characterization,* vol. 48, pp. 11-36, 2002.

[58] I. Sneddon, "The relation between load and penetration in the axisymmetric Boussinesq problem for a punch of arbitrary profile," *Int J Eng Sci,* vol. 3, pp. 47-56, 1965.

[59] G. Simmons and H. Wang, *Single Crystal Elastic Constants and Calculated Aggregate Properties: A Handbook*, 2 ed.: the M.I.T. Press, 1971.

[60] W. C. Oliver and G. M. Pharr, "Improved technique for determining hardness and elastic modulus using load and displacement sensing indentation experiments," *Journal of Materials Research,* vol. 7, pp. 1564-1580, 1992.

[61] J. Mencik, D. Munz, E. Quandt, E. R. Weppelmann, and M. V. Swain, "Determination of elastic modulus of thin layers using nanoindentation," *Journal of Materials Research,* vol. 12, pp. 2475-2484, 1997.

[62] G. M. Pharr and W. C. Oliver, "Measurement of thin film mechanical properties using nanoindentation," *MRS Bulletin,* vol. 17, pp. 28-28, 1992.

[63] R. Saha and W. D. Nix, "Effects of the substrate on the determination of thin film mechanical properties by nanoindentation," *Acta Materialia,* vol. 50, pp. 23-38, 2002.

[64] H. Buckle, in *The Science of Hardness Testing and its Applications*, J. W. Westbrook and H. Conrad, Eds. OH: American Society for Metals, Metal Park, 1973, pp. 453-491.

[65] R. B. King, "Elastic analysis of some punch problems for a layered medium," *International Journal of Solids and Structures,* vol. 23, pp. 1657-1664, 1987.

[66] H. Gao, C.-H. Chiu, and J. Lee, "Elastic contact versus indentation modeling of multi-layered materials," *International Journal of Solids and Structures,* vol. 29, pp. 2471-2492, 1992.

[67] X. Chen and J. J. Vlassak, "Numerical study on the measurement of thin film mechanical properties by means of nanoindentation," *Journal of Materials Research,* vol. 16, pp. 2974-2982, 2001.

[68] H. Xu and G. M. Pharr, "An improved relation for the effective elastic compliance of a film/substrate system during indentation by a flat cylindrical punch," *Scripta Materialia,* vol. 55, pp. 315-318, 2006.

[69] S. M. Han, R. Saha, and W. D. Nix, "Determining hardness of thin films in elastically mismatched film-on-substrate systems using nanoindentation," *Acta Materialia,* vol. 54, pp. 1571-1581, 2006.

[70] P. J. Burnett and D. S. Rickerby, "The mechanical properties of wear-resistant coatings : : II: Experimental studies and interpretation of hardness " *Thin Solid Films,* vol. 148, pp. 51-65 1987.

[71] J. L. Hay, M. E. O'Hern, and W. C. Oliver, "Importance of contact radius for substrate-independent property measurement of thin films," in *Mater Res Symp Proc*, 1998, pp. 27-32.

[72] A. M. Korsunsky, M. R. McGurk, S. J. Bull, and T. F. Page, "On the hardness of coated systems," *Surface and Coatings Technology,* vol. 99, pp. 171-183, 1998.

[73] T. Y. Tsui and G. M. Pharr, "Substrate effects on nanoindentation mechanical property measurement of soft films on hard substrates," in *J Mater Res* 1999, p. 292.

[74] P. J. Burnett and D. S. Rickerby, "The mechanical properties of wear-resistant coatings: I: Modelling of hardness behaviour," *Thin Solid Films,* vol. 148, pp. 41-50, 1987.

[75] Y.-T. Cheng and C.-M. Cheng, "Relationships between hardness, elastic modulus, and the work of indentation," *Applied Physics Letters,* vol. 73, pp. 614-614, 1998.

[76] K. C. Tang and R. D. Arnell, "Determination of coating mechanical properties using spherical indenters," *Thin Solid Films,* vol. 355-356, pp. 263-269, 1999.

[77] H. Y. Yu, S. C. Sanday, and B. B. Rath, "The effect of substrate on the elastic properties of films determined by the indentation test -- axisymmetric boussinesq problem," *Journal of the Mechanics and Physics of Solids,* vol. 38, pp. 745-764, 1990.

[78] B. Zhou and B. C. Prorok, "A discontinuous elastic interface transfer model of thin film nanoindentation " *in press Exp. Mech,* 2010.

[79] B. Zhou and B. C. Prorok, "A new paradigm in thin film indentation," *in press J. Mater. Res.,* 2010.

[80] H. D. Chen, K. R. Udayakumar, C. J. Gaskey, and L. E. Cross, "Electrical properties' maxima in thin films of the lead zirconate-lead titanate solid solution system," *Applied Physics Letters,* vol. 67, pp. 3411-3411, 1995.

[81] D. Remiens, E. Cattan, C. Soyer, and T. Haccart, "Piezoelectric properties of sputtered PZT films: Influence of structure, micro structure, film thickness (Zr,Ti) ratio and Nb substitution," 2002, pp. 123-127.

[82] A. Seifert, N. Ledermann, S. Hiboux, J. Baborowski, P. Muralt, and N. Setter, "Processing optimization of solution derived PbZr1-xTixO3 thin films for piezoelectric applications," Aachen, Germany, 2001, pp. 1889/159-1896/166.

[83] R. A. Wolf and S. Trolier-McKinstry, "Temperature dependence of the piezoelectric response in lead zirconate titanate films," *Journal of Applied Physics,* vol. 95, pp. 1397-1406, 2004.

[84] F. Xu, R. A. Wolf, T. Yoshimura, and S. Trolier-McKinstry, "Piezoelectric films for MEMS applications," Melbourne, VIC., Australia, 2002, pp. 386-396.

[85] I. Kanno, H. Kotera, K. Wasa, T. Matsunaga, T. Kamada, and R. Takayama, "Crystallographic characterization of epitaxial Pb(Zr, Ti)O3 films with different Zr/Ti ratio grown by radio-frequency-magnetron sputtering," *Journal of Applied Physics,* vol. 93, pp. 4091-4096, 2003.

[86] E. Cattan, G. Velu, B. Jaber, D. Remiens, and B. Thierry, "Structure control of Pb(Zr,Ti)O3 films using PbTiO3 buffer layers produced by magnetron sputtering," *Applied Physics Letters,* vol. 70, pp. 1718-1718, 1997.

[87] D. Fu, H. Suzuki, T. Ogawa, and K. Ishikawa, "High-piezoelectric behavior of c-axis-oriented lead zirconate titanate thin films with composition near the

morphotropic phase boundary," *Applied Physics Letters,* vol. 80, pp. 3572-3572, 2002.

[88] P. Lin, Y. K. Wang, and T. Y. Tseng, "Enhanced ferroelectric properties of Pb(Zr0.53Ti0.47)O3 thin films on SrRuO3/Ru/SiO2/Si substrates," *Applied Physics Letters,* vol. 80, pp. 3790-3790, 2002.

[89] Y. Lin, B. R. Zhao, H. B. Peng, B. Xu, H. Chen, F. Wu, H. J. Tao, Z. X. Zhao, and J. S. Chen, "Growth and polarization features of highly (100) oriented Pb(Zr0.53Ti0.47)O3 films on Si with ultrathin SiO2 buffer layer," *Applied Physics Letters,* vol. 73, pp. 2781-2781, 1998.

[90] H. Morioka, G. Asano, T. Oikawa, H. Funakubo, and K. Saito, "Large remanent polarization of 100% polar-axis-oriented epitaxial tetragonal Pb(Zr0.35Ti0.65)O3 thin films," *Applied Physics Letters,* vol. 82, pp. 4761-4763, 2003.

[91] M. J. Madou, *Fundamentals of Microfabrication*. Boca Raton: CRC Press, 1997.

[92] D.-J. Kim, J.-P. Maria, A. I. Kingon, and S. K. Streiffer, "Evaluation of intrinsic and extrinsic contributions to the piezoelectric properties of Pb(Zr1-XTX)O3 thin films as a function of composition," *Journal of Applied Physics,* vol. 93, pp. 5568-5575, 2003.

[93] V. Nagarajan, A. Stanishevsky, L. Chen, T. Zhao, B. T. Liu, J. Melngailis, A. L. Roytburd, R. Ramesh, J. Finder, Z. Yu, R. Droopad, and K. Eisenbeiser, "Realizing intrinsic piezoresponse in epitaxial submicron lead zirconate titanate capacitors on Si," *Applied Physics Letters,* vol. 81, pp. 4215-4217, 2002.

[94] J. Lappalainen, J. Frantti, and V. Lantto, "Electrical and mechanical properties of ferroelectric thin films laser ablated from a Electrical and mechanical properties of ferroeletric thin-films laser ablated from a Pb0.97Nd0.02(Zr0.55Ti0.45)O3 target," *Journal of Applied Physics,* vol. 82, pp. 3469-3477, 1997.

[95] S. S. Sengupta, S. M. Park, D. A. Payne, and L. H. Allen, "Origins and evolution of stress development in sol-gel derived thin layers and multideposited coatings of lead titanate," *Journal of Applied Physics,* vol. 83, pp. 2291-2291, 1998.

[96] G. A. C. M. Spierings, G. J. M. Dormans, W. G. J. Moors, M. J. E. Ulenaers, and P. K. Larsen, "Stresses in Pt/Pb(Zr,Ti)O_3/Pt thin film stacks for integrated ferroelectric capacitors," *Journal of Applied Physics,* vol. 78, pp. 1926-1933, 1995.

[97] T. J. Garino and H. M. Harrington, "Residual stress in PZT thin films and its effect on ferroelectric properties," in *Mat. Res. Soc. Symp. Proc.*, 1992, pp. 341-347.

[98] L. Lian and N. R. Sottos, "Stress effects in sol-gel derived ferroelectric thin films," *Journal of Applied Physics,* vol. 95, pp. 629-634, 2004.

[99] M. Gad-el-Hak, "MEMS: Design and Fabrication ", 2 ed Boca Raton: CRC Press, 2005.

[100] http://www.eng.tau.ac.il/~hanein/teaching/materials%20for%20MEMS.pdf.

[101] http://www.memsnet.org/news/.

[102] S. M. Spearing, "Materials issues in microelectromechanical systems (MEMS)," *Acta Materialia,* vol. 48, pp. 179-196, 2000.

[103] L. S. Phillips and B. S. Ma, "Ferroelectric films by flash evaporation of PZT," *Electronic Components,* vol. 12, pp. 523-526, 1971.

[104] R. N. Castellano and L. G. Feinstein, "Ion-beam deposition of thin films of ferroelectric pzt," *J. Appl. Phys.,* vol. 50, pp. 4406-4411, 1979.

[105] M. Ischida, S. Tsuji, K. Kimura, H. Matsunami, and T. Tanaka, "Epitaxial growth of ferroelectric PLZT [(Pb, La)(Zr, Ti)O3] thin films," *Journal of Crystal Growth,* vol. 45, pp. 393-398, 1978.

[106] Y. Sakashita, T. Ono, H. Segawa, K. Tominaga, and M. Okada, "Preparation and electrical properties of MOCVD-deposited PZT thin films," *J. Appl. Phys.,* vol. 69, pp. 8352-8357, 1991.

[107] "ASTM Standard Test Method E 384," in *Annual Book of Standards 3.01*: American Society for Testing and Materials, 1989, p. 469.

[108] G. N. Peggs and I. C. Leigh, "Recommended procedure for microindentation Vickers hardness test," UK National Physical Laboratory MOM 62, 1983.

[109] J. H. Park, S. H. Yoon, D. Shen, S. Y. Choe, Y. S. Yoon, M. Park, and D. J. Kim, "Effects of preferred orientation on the piezoelectric properties of Pt/ $Pb(Zr_{0.3}Ti_{0.7})O_3$/Pt thin films grown by sol-gel process," *J Mater Sci: Mater Electron,* vol. 20, pp. 366-373, 2009.

[110] D. C. Van Der Laan, J. W. Ekin, C. C. Clickner, and T. C. Stauffer, "Delamination strength of YBCO coated conductors under transverse tensile stress," *Superconductor Science and Technology,* vol. 20, pp. 765-770, 2007.

[111] in *IEEE,Micro Electro Mechanical Systems Workshop*, Napa Vally,California, Feb 1990, p. 174.

[112] M. T. Kim, "Influence of substrates on the elastic reaction of films for the microindentation tests," *Thin Solid Films,* vol. 283, pp. 12-16, 1996.

[113] in *IEEE,Micro Electro Mechanical Systems Workshop*, SanDiego,California, Feb 1996, p. 97.

[114] J. J. Vlassak and W. D. Nix, "A new bulge test technique for the determination of Young's modulus and Poisson's ratio of thin films," *Journal of Materials Research,* vol. 7, pp. 3242-3249, 1992.

[115] M. Zhang, B. Yang, J. Chu, and T. G. Nieh, "Hardness enhancement in nanocrystalline tantalum thin films," *Scripta Materialia,* vol. 54, pp. 1227-1230, 2006.

[116] T. A. Berfield, R. J. Ong, D. A. Payne, and N. R. Sottos, "Residual stress effects on piezoelectric response of sol-gel derived lead zirconate titanate thin films," *Journal of Applied Physics,* vol. 101, 2007.

[117] T. Haccart, E. Cattan, and D. Remiens, "Dielectric, ferroelectric and piezoelectric properties of sputtered PZT thin films on Si substrates:influence of film thickness and orientation," *Semicond. Phys. Quantum Electron. Optoelectron,* vol. 5, pp. 78-88, 2002.

[118] R. J. Ong, D. A. Payne, and N. R. Sottos, "Processing effects for integrated PZT: Residual stress, thickness, and dielectric properties," *Journal of the American Ceramic Society,* vol. 88, pp. 2839-2847, 2005.

[119] J. F. Meng, R. S. Katiyar, G. T. Zou, and X. H. Wang, "Raman phonon modes and ferroelectric phase transitions in nanocrystalline lead zirconate titanate," *Physica Status Solidi (A) Applied Research,* vol. 164, pp. 851-862, 1997.

[120] T. Ohno, T. Matsuda, K. Ishikawa, and H. Suzuki, "Thickness dependence of residual stress in alkoxide-derived Pb(Zr 0.3Ti0.7)O3 thin film by chemical solution deposition," *Japanese Journal of Applied Physics, Part 1: Regular Papers and Short Notes and Review Papers,* vol. 45, pp. 7265-7269, 2006.

[121] H. Yi, M. G. Kim, J. H. Park, and H. M. Jang, "Polarized Raman scattering of highly [111]-oriented Pb(Zr, Ti)O3 thin films in the rhombohedral-phase field," *Journal of Applied Physics,* vol. 96, pp. 5110-5116, 2004.

[122] J. H. Lee, K. S. Hwang, and T. S. Kim, "Microstress relaxation effect of Pb(Zr0.52Ti0.48) O3 films with thicknesses for micro/nanopiezoelectric device," *Applied Physics Letters,* vol. 96.

[123] W. H. Xu, D. Lu, and T. Y. Zhang, "Determination of residual stresses in Pb(Zr0.53Ti0.47)O3 thin films with Raman spectroscopy," *Applied Physics Letters,* vol. 79, pp. 4112-4112, 2001.

[124] P. Delobelle, O. Guillon, E. Fribourg-Blanc, C. Soyer, E. Cattan, and D. Remiens, "True Young modulus of Pb(Zr,Ti)O3 films measured by nanoindentation," *Applied Physics Letters,* vol. 85, pp. 5185-5187, 2004.

[125] B. Zhou and B. C. Prorok, "A discontinuous elastic interface transfer model of thin film nanoindentation," *Exp. Mech.,* vol. 50, pp. 793-801, 2010.

[126] B. Zhou and B. C. Prorok, "A new paradigm In thin film Indentation," *Journal of Materials Research,* vol. 25, pp. 1671-1678, 2010.

[127] G. M. Pharr, J. H. Strader, and W. C. Oliver, "Critical issues in making small-depth mechanical property measurements by nanoindentation with continuous stiffness measurement," *Journal of Materials Research,* vol. 24, pp. 653-666, Mar 2009.

[128] B. Bhushan and X. D. Li, "Micromechanical and tribological characterization of doped single-crystal silicon and polysilicon films for microelectromechanical systems devices," *Journal of Materials Research,* vol. 12, pp. 54-63, Jan 1997.

[129] G. He, J. Eckert, W. Loser, and M. Hagiwara, "Processing dependence of Young's modulus of Ti-base nanostructured alloys," *Solid State Communications,* vol. 129, pp. 711-715, 2004.

[130] W. R. C. Jr., D. A. Berlincourt, and F. J. Scholz, "Thermal Expansion and. Pyroelectricity in Lead Titanate Zirconate and Barium Titanate," *J. Appl. Phys.,* vol. 34, p. 1392, 1963.

[131] J.-h. Park, "Development of MEMS Piezoelectric Energy Harvesters," in *Materials Engineering*. vol. Ph.D Auburn: Auburn, 2010, p. 172.

[132] S. E. Lyshevski, "MES and NEMS: Systems, Devices, and Structures," in *Nano- and Microscience, Engineering, Technology, and Medicine Series* Boca Raton: CRC Press, 2002.

[133] "User's manual for MTI-2000 Fotonic Sensor."

[134] N. P. Vyshatko, P. M. Vilarinho, and A. L. Kholkin, "Electromechanical measurements of electric field-induced displacements of fibers," *Review of Scientific Instruments,* vol. 79, 2008.

[135] C. A. Klein and R. P. Miller, "Strains and stresses in multilayered elastic structures: The case of chemically vapor-deposited ZnS/ZnSe laminates," *Journal of Applied Physics,* vol. 87, pp. 2265-2272, 2000.

[136] M. H. Zhao, R. Fu, D. Lu, and T. Y. Zhang, "Critical thickness for cracking of Pb(Zr0.53Ti0.47)O3 thin films deposited on Pt/Ti/Si(100) substrates," *Acta Materialia,* vol. 50, pp. 4241-4254, 2002.

[137] S. O. Kramarov and J. S. Rez, "Mechanical strength of ferroelectric single crystals and ceramics: Experimental studies and fracture theory," *Progress in Crystal Growth and Characterization of Materials,* vol. 22, pp. 199-244, 1991.

[138] J. F. Shackelford and W. Alexander, *Materials science and engineering handbook*, 3rd ed. Boca Raton,London: CRC Press, 2001.

[139] W.-H. Xu, D. Lu, and T.-Y. Zhang, "Determination of residual stresses in $Pb(Zr_{0.53}Ti_{0.47})O_3$ thin films with Raman spectroscopy," *Applied Physics Letters,* vol. 79, pp. 4112-4114, 2001.

[140] S. Huang and X. Zhang, "An analysis of elastic deformation induced by gradient residual stresses in multilayered MEMS structures," Orlando, FL, United states, 2005, pp. 359-362.

[141] S. Huang and X. Zhang, "Gradient residual stress induced elastic deformation of multilayer MEMS structures," *Sensors and Actuators, A: Physical,* vol. 134, pp. 177-185, 2007.

[142] G. C. A. M. Janssen, M. M. Abdalla, F. van Keulen, B. R. Pujada, and B. van Venrooy, "Celebrating the 100th anniversary of the Stoney equation for film stress: Developments from polycrystalline steel strips to single crystal silicon wafers," *Thin Solid Films,* vol. 517, pp. 1858-1867, 2009.

[143] C. A. Klein, "How accurate are Stoney's equation and recent modifications," *Journal of Applied Physics,* vol. 88, pp. 5487-5487, 2000.

[144] P. H. Townsend, D. M. Barnett, and T. A. Brunner, "Elastic relationships in layered composite media with approximation for the case of thin films on a thick substrate," *Journal of Applied Physics,* vol. 62, pp. 4438-4444, 1987.

[145] W. D. Nix and R. F. Mehl Medalist, "Mechanical properties of thin films," *Metallurgical transactions. A, Physical metallurgy and materials science,* vol. 20 A, pp. 2217-2245, 1989.

[146] C. Huang, Y. Y. Lin, and T. A. Tang, "Study on the tip-deflection of a piezoelectric bimorph cantilever in the static state," *Journal of Micromechanics and Microengineering,* vol. 14, pp. 530-534, 2004.

[147] J.-W. Lee, C.-S. Park, M. Kim, and H.-E. Kim, "Effects of residual stress on the electrical properties of PZT films," *Journal of the American Ceramic Society,* vol. 90, pp. 1077-1080, 2007.

[148] T. Ohno, H. Suzuki, H. Masui, K. Ishikawa, and M. Fujimoto, "Effect of back-etching on residual stress in lead titanate thin films on Si wafer," *Journal of Applied Physics, Part 1: Regular Papers and Short Notes and Review Papers,* vol. 43, pp. 6549-6553, 2004.

[149] M. B. Kelman and P. C. McIntyre, "Effect of applied mechanical strain on the ferroelectric and dielectric properties of Pb(Zr0.35Ti0.65)O3 thin films," *Journal of Applied Physics,* vol. 93, pp. 9231-9236, 2003.

[150] T. Kumazawa, Y. Kumagai, H. Miura, M. Kitano, and K. Kushida, "Effect of external stress on polarization in ferroelectric thin films," *Applied Physics Letters,* vol. 72, pp. 608-608, 1998.

[151] X. Lu, J. Zhu, X. Li, Z. Zhang, X. Zhang, D. Wu, F. Yan, Y. Ding, and Y. Wang, "Effect of uniaxial stress on the polarization of SrBi2Ta2O9 thin films," *Applied Physics Letters,* vol. 76, pp. 3103-3105, 2000.

[152] S. Trolier-McKinstry, C. A. Randall, J. P. Maria, C. Theis, D. G. Schlom, J. Shepard Jr, and K. Yamakawa, "Size effects and domains in ferroelectric thin film actuators," San Francisco, CA, USA, 1996, pp. 363-374.

[153] D. S. Fu, H. Iwazaki, H. Suzuki, and K. Ishikawa, "Phonon mode behaviours of PbTiO3 thin films deposited on Pt/Si substrates," *Journal of Physics Condensed Matter,* vol. 12, pp. 399-414, 2000.

[154] D. Liu, C. Wang, H. Zhang, J. Li, L. Zhao, and C. Bai, "Domain configuration and interface structure analysis of sol–gel-derived PZT ferroelectric thin films," *Surface and Interface Analysis,* vol. 32, pp. 27-31, 2001.

Appendix A

Table A.1 Parameters for sputtering Ti and Pt

Base pressure (Torr)	$5x10^{-6}$	Substrate	Si/SiO_2

	DC sputtering	DC sputtering
Target Material	Pt	Ti
Pre-Sputtering Power (W)	100	400
Pre-Sputtering time (sec)	20	25
Sputtering Power (W)	100	400
Sputtering time (sec)	360	25
Gas 1 (Ar) flow rate (sccm)	25	25
Gas 2 (O_2/N_2) flow rate (sccm)		
Deposition Pressure (mTorr)	5	5
Deposition Temperature (^0C)	R.T	R.T
Substrate holder rotation (%)	50	50
Ignition Pressure (mTorr)		
Expected Film Thickness (nm)	120	10

Appendix B

Table B.1 Fabrication details of PZT cantilevers with different thickness

Procedure	Fabrication method	Thickness	Experimental conditions
Dehydration of PZT wafer	Microprocessor oven		120^0C,20min
Promotion of PR adhesion	HDMS		12-15 drops in the glass chamber, 5min
Top electrode patterning (nLOF 2035)	Lithography	~2µm	3000 rpm 1500 acc 30s, soft bake 1min @110^0C, UV exposure 6s, AZ 300K MIF develop 1~1.2 min, post bake 1 min @ 110^0C
Electrode deposition	Sputtering	120nm	100 W (DC), 360 sec, 25 sccm Ar
Lift-off			Acetone, Methanol, DI water rinse
1st cantilever patterning (AZ P4620)	Lithography	~15µm	1000 rpm 250 acc 30s, soft bake 1.5min @110^0C, (UV exposure 25s+60 interval) 3times, AZ 400K (1:2.5)develop 3.5~4 min, hard bake 1 min @ 120^0C
Front-side etching&bottom electrode access	DRIE-AOE	~1.75µm	600W(c), 150W(p), 30sccm(SF6), 240 V bias
2st cantilever patterning (AZ P4620)	Lithography	~15µm	1000 rpm 250 acc 30s, soft bake 1.5min @110^0C, (UV exposure 25s+60 interval) 3times, AZ 400K (1:2.5)develop 3.5~4 min, hard bake 1 min @ 120^0C
Front-side SiO_2 etching	DRIE-AOE	500nm	600W(c), 150W(p), 30sccm(SF6), 240 V bias
Front-side Si etching	DRIE-ASE	250/125/ 65 µm	Etching: 600W(coil), 12W(platen), 130 sccm (SF_6), 13 sccm (O_2), 13 sec; Passivation : 600W(coil), 0W(platen), C_4F_8 85 sccm, 7 sec;
Back-side patterning	Lithography	~15µm	1000 rpm 250 acc 30s, soft bake 1.5min @110^0C, (UV exposure 25s+60 interval) 3times, AZ 400K (1:2.5)develop 3.5~4 min, hard bake

			1 min @ 120^0C
Back-side SiO_2 etching	DRIE-AOE	500nm	600W(c), 150W(p), 30sccm(SF6), 240 V bias
Back-side Si etching	DRIE-ASE	250/375/ 435 µm	Etching: 600W(coil), 12W(platen), 130 sccm (SF_6), 13 sccm (O_2), 13 sec; Passivation : 600W(coil), 0W(platen), C_4F_8 85 sccm, 7 sec; 17 mTorr, 230 V bias

Appendix C

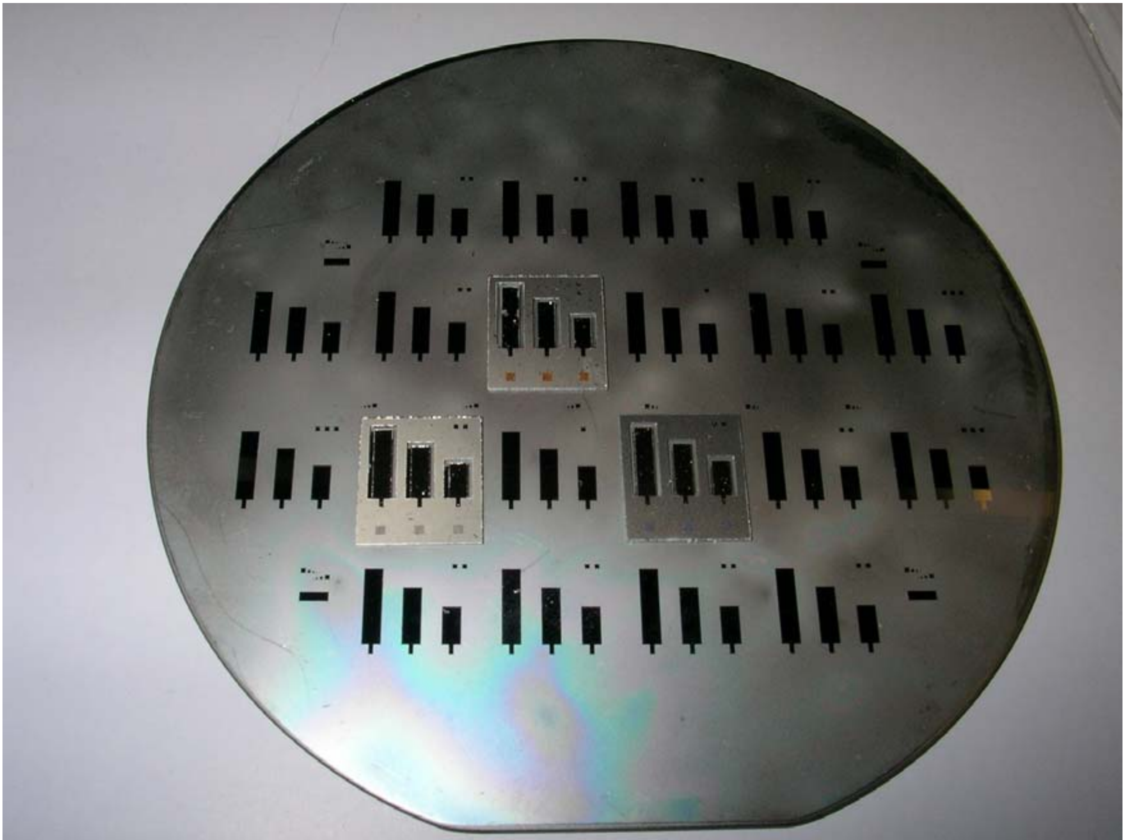

Picture of fabricated cantilever array on the wafer